UNIVERSITY OF CALIFORNIA,
IRVINE

Molecular hydrogen in Earth's atmosphere: reconstructions and interpretation

DISSERTATION

submitted in partial satisfaction of the requirements
for the degree of

DOCTOR OF PHILOSOPHY

Earth System Science

by

John David Patterson

Dissertation Committee:
Professor Eric Saltzman, Chair
Professor Michael Prather
Professor Ann Marie Carlton
Professor Steve Allison

2022

DEDICATION

To

my parents, Mary and Larry

"Our posturings, our imagined self-importance, the delusion that we have some privileged position in the Universe, are challenged by this point of pale light. Our planet is a lonely speck in the great enveloping cosmic dark. In our obscurity, in all this vastness, there is no hint that help will come from elsewhere to save us from ourselves.

The Earth is the only world known so far to harbor life. There is nowhere else, at least in the near future, to which our species could migrate. Visit, yes. Settle, not yet. Like it or not, for the moment the Earth is where we make our stand."

-Carl Sagan

TABLE OF CONTENTS

Page

LIST OF FIGURES **v**

LIST OF TABLES **ix**

ACKNOWLEDGEMENTS **x**

VITA **xi**

ABSTRACT OF THE DISSERTATION **xiv**

1 Introduction **1**
1.1 Overview of this dissertation 1
1.2 Background 3
1.2.1 Budget and distribution of molecular hydrogen in the atmosphere 4
1.2.2 Atmospheric chemistry, climate, and air quality impacts of H_2 8
1.2.3 Polar firn and ice cores as an archive of past atmospheric composition 11
1.2.4 H_2 in polar firn and ice 16

2 Diffusivity and solubility of H_2 in ice type Ih: Implications for the behavior of H_2 in polar ice **20**
2.1 Overview 20
2.2 Introduction 20
2.3 Experimental methods 22
2.3.1 Quantification of H_2 in air 22
2.3.2 Experimental design 23
2.3.3 Data analysis 27
2.4 Results 28
2.5 Comparison to previous work 34
2.5.1 Diffusivity 34
2.5.2 Solubility 35
2.6 Implications for the mobility of H_2 in polar firn and ice 38
2.6.1 Pore close-off fractionation 38
2.6.2 Diffusive migration of H_2 in an ice sheet 42
2.6.3 Post-coring diffusive exchange with atmospheric H_2 44
2.7 Summary and conclusions 51

3 Reconstruction atmospheric H_2 from polar firn air **53**
3.1 Overview 53
3.2 Introduction 54
3.3 Firn air sites, sampling, and H_2 measurements 55
3.3.1 Firn air sites 55
3.3.2 Firn air sampling 59

3.3.3 Firn air H_2 measurements and calibration 60
3.4 Firn air modeling and inversions 69
3.4.1 Firn air model 69
3.4.2 Firn air inversion modeling 74
3.5 Antarctic firn results 81
3.5.1 Atmospheric reconstructions-Antarctica 81
3.5.2 Assessing bias in the atmospheric reconstruction-Antarctica 87
3.6 Greenland firn results 97
3.6.1 Atmospheric reconstructions-Greenland 97
3.6.2 Assessing bias in the atmospheric reconstruction-Greenland 107
3.7 Summary and conclusions 114

4 Synthesis of northern hemisphere and southern hemisphere atmospheric H_2 reconstructions 116
4.1 Overview 116
4.2 Introduction 116
4.3 Atmospheric box modeling 117
4.3.1 6-box model overview 117
4.3.2 Detailed description of sources and sinks 119
4.4 Box model evaluation 121
4.5 20^{th} century changes to H_2 sources 127
4.6 Late 20^{th} century atmospheric H_2 trends 130
4.7 Comparison of atmospheric H_2 over Antarctica and Greenland 133
4.7.1 Uncertainties in the budget? 134
4.7.2 Bias in the Greenland reconstruction 140
4.8 Summary and conclusions 146

5 Conclusions and future directions 148
5.1 Key findings and outstanding questions 148
5.2 Broader context and future directions 150

Bibliography 154

LIST OF FIGURES

		Page
Figure 1.1	Monthly averaged H_2 mixing ratios from modern in situ measurements from AGAGE	8
Figure 1.2	Schematic of the role of H_2 as an ozone precursor and indirect greenhouse gas	11
Figure 1.3	A simplified schematic of gas transport in the firn column	14
Figure 1.4	An 800 kyr record of atmospheric change and climate proxies from Antarctic ice cores and the benthic $\delta^{18}O$ stack	15
Figure 1.5	A schematic of pore close-off fractionation	18
Figure 1.6	Previously published reconstructions of atmospheric H_2 using firn air measurements from NEEM, Greenland	19
Figure 2.1	Cross-polar microscope image of a piece of ice prepared as the ice used for the permeability experiments	26
Figure 2.2	Schematic of the laboratory setup used to measure H_2 permeation in ice	26
Figure 2.3	Results from a single permeation experiment	31
Figure 2.4	Arrhenius plots of the results from all permeation experiments	32
Figure 2.5	Comparison of diffusivity, solubility, and permeability data from our experiments and literature data for H_2 and other gases	36
Figure 2.6	Results from a model simulation of H_2 diffusion between a pressurized bubble and unpressurized open pores showing characteristic relaxation time as a function of firn depth	41
Figure 2.7	X-ray tomography image of the porosity field from just below the close-off depth	42
Figure 2.8	Results from a model simulation of a pulse of H_2 propagating through the ice sheet at South Pole	44
Figure 2.9	Model simulation of equilibration of ice core samples recovered from South Pole from bubbly and bubble-free clathrate ice	49
Figure 3.1	Locations of the South Pole and Megadunes firn air sampling sites in Antarctica	57

Figure 3.2	Locations of the NEEM, Summit, and Tunu firn air sampling sites in Greenland	58
Figure 3.3	Schematic of a typical firn air sampling apparatus	60
Figure 3.4	Raw measurements of H_2 in firn air from the five sites used in this analysis	65
Figure 3.5	Intercomparison of surface flask measurements from Cape Grim, Tasmania from NOAA/GML and AGAGE.	66
Figure 3.6	Intercomparison of surface flask measurements from Cape Grim, Tasmania from NOAA/GML and CSIRO.	67
Figure 3.7	-Depth-averaged measurements of H_2 in firn air adjusted to the MPI09 calibration scale and corrected for detector non-linearity and gravitational fractionation	68
Figure 3.8	Measured and modeled depth profiles at Megadunes for CO_2 and CH_4	73
Figure 3.9	Age distributions or "Green's functions," calculated by the firn air model for South Pole	80
Figure 3.10	Comparison of H_2 reconstructions with three different inversion methods using Megadunes firn air measurements	81
Figure 3.11	Firn air reconstructions from the two Antarctic sites and associated depth profiles	84
Figure 3.12	Histograms for the posterior distributions of β	85
Figure 3.13	Joint reconstruction from the two Antarctic sites and associated depth profiles	86
Figure 3.14	Development of the CH_4-based age distribution correction	91
Figure 3.15	Reconstructions of southern hemisphere atmospheric CH_4 using original and corrected age distributions	92
Figure 3.16	Reconstructions of southern hemisphere atmospheric CO_2 using original age distributions and age distributions with the CH_4-based corrections applied	93
Figure 3.17	Reconstructions of southern hemisphere atmospheric CH_3CCl_3 using original age distributions and age distributions with the CH_4-based corrections applied	94
Figure 3.18	Comparison of atmospheric H_2 reconstructions using original age distributions and age distributions with the CH_4-based corrections applied	95

Figure 3.19	Firn air reconstructions from the three Greenland sites and associated depth profiles	104
Figure 3.20	Joint reconstruction from the three Greenland sites and associated depth profiles	105
Figure 3.21	Joint reconstruction from the three Greenland sites and associated depth profiles assuming a Tunu calibration offset	106
Figure 3.22	Surface flask measurements of atmospheric H_2 at high northern latitude sites	107
Figure 3.23	Reconstructions of northern hemisphere atmospheric CH_4 using original and corrected age distributions	110
Figure 3.24	Reconstructions of southern hemisphere atmospheric CO_2 using original age distributions and age distributions with the CH_4-based corrections applied	111
Figure 3.25	Comparison of atmospheric H_2 reconstructions using original age distributions and age distributions with the CH_4-based corrections applied	112
Figure 4.1	Comparison of monthly atmospheric H_2 levels from 1995-2014 generated by the box model, GFDL-AM4.1, and flask measurements	124
Figure 4.2	Comparison of annually averaged H_2 levels from 1995-2014 generated by the box model, GFDL-AM4.1, and flask measurements	125
Figure 4.3	Comparison of H_2 seasonal cycles from 1995-2014 generated by the box model, GFDL-AM4.1, and flask measurements	126
Figure 4.4	Global H_2 sources and results from the 1910-2013 base-case box model run compared to the firn air reconstruction and modern flask measurements	129
Figure 4.5	Global biomass burning emissions of H_2 from Van Marle et al. (2017) and calculated from Lamarque et al. (2010)	131
Figure 4.6	Comparison of box model output from the base-case 1910-2014 run and the CB run	132
Figure 4.7	Comparison of box model output from the base-case 1910-2014 run and the steady-state run	132
Figure 4.8	Comparison of joint firn air reconstructions from Antarctica and Greenland	133

Figure 4.9 Comparison of firn air reconstructions with the box model run with the high northern latitude soil sink reduced to 0 and the southern tropical box soil sink increased by the corresponding amount 137

Figure 4.10 Comparison of firn air reconstructions (solid lines) with the box model run with the high northern latitude soil sink reduced to half of its base-case strength and the southern tropical box soil sink increased by the corresponding amount 138

Figure 4.11 Comparison of firn air reconstructions (solid lines and shading) with the box model run with the high northern latitude soil sink ramped from 0 to half of its base-case strength 139

Figure 4.12 Comparison of firn air reconstructions (solid lines) with the box model run with the strength of anthropogenic emissions increased by 75% from its base-case strength and the production from CH_4 oxidation reduced by 46% from its base-case strength 139

Figure 4.13 Comparison of the joint firn air reconstruction from Antarctica and the reconstruction from Tunu 143

Figure 4.14 Comparison of the joint firn air reconstruction from Antarctica and the joint reconstruction from Greenland, assuming a calibration offset for NEEM and Summit 144

Figure 4.15 Joint atmospheric H_2 reconstruction using firn air from three Greenland sites and associated depth profiles, assuming pore close-off fractionation is underestimated 145

Figure 4.16 Comparison of the joint firn air reconstruction from Antarctica and the joint reconstruction from Greenland that is plotted in Figure 4.15 146

LIST OF TABLES

		Page
Table 1.1	Several published estimates of the modern budget of atmospheric H_2	7
Table 2.1	Chromatographic parameters for the GC-HePDD analytical system	23
Table 2.2	Summary of experimental results for H_2 diffusivity, solubility, and permeability derived from the individual block degassing experiments	33
Table 2.3	Parameter estimates for the Arrhenius to the diffusivity, permeability, and solubility of H_2	34
Table 2.4	Summary of the diffusivity, solubility, and permeability data from various literature sources that is plotted in Figure 2.5	37
Table 2.5	Comparison of gas partitioning for a system with only bubbles and for a system with bubbles in thermodynamic equilibrium with clathrates	50
Table 3.1	Site characteristics and associated references for each of the five firn air sampling campaigns used in this research	56
Table 3.2	Summary of the firn air H_2 measurements from each of the five sites	64
Table 3.3	R^2 and RMSE values for southern hemisphere reconstructions compared to established atmospheric histories using original age distributions and corrected age distributions for CH_4, CO_2, and CH_3CCl_3.	96
Table 3.4	R^2 and RMSE values for northern hemisphere reconstructions compared to established atmospheric histories using original age distributions and corrected age distributions for CH_4 and CO_2	113

ACKNOWLEDGEMENTS

I would like to extend my deepest gratitude to my advisor, Dr. Eric Saltzman. Your passion and intellect have been an endless source of inspiration. This work would not have been possible without your dedication, guidance, and enthusiastic support. Heartfelt thanks to my committee members, Dr. Michael Prather, Dr. Ann Marie Carlton, and Dr. Steve Allison. Your input has been invaluable to this dissertation. I would also like to thank the many amazing members of the Saltzman/Aydin group with whom I've had the pleasure of working during my time at UCI. In particular, I would like to express my utmost appreciation to Murat Aydin for sharing his wealth of knowledge, to Mindy Nicewonger for her encouragement and mentorship during my first year, and to Jenn Campos Ayala for her friendship and support, especially on days when I was feeling drained. Thank you to Cyril McCormick for always figuring out a way to somehow fix the broken machines. Thanks to Gabi Petron, Andy Crotwell, and Paul Krummel for useful discussions and helping me deal with drifting calibrations. Thanks to Jeff Severinghaus for sharing code, ideas, and measurements. Thanks to Mark Steinborn and Chris Peterson for their professionalism and skill. And thanks to my first-year cohort for their help and support throughout our coursework and beyond. I would also like to acknowledge the American Geophysical Union and the National Academy of Sciences for the use of their previously published material.

Graduate school is difficult, and I wouldn't have made it without the assistance of an extensive support network. Most importantly, my parents, Mary and Larry, supported and believed in me, even when I didn't believe in myself. I wouldn't be here without them. Thanks to my brother Nathan for his companionship, humor, and book recommendations. Thank you to my wonderful girlfriend, Ivy. Your love and patience have meant the world to me. And thanks to my many climbing and skiing partners: Mackenzie, Josh, Sunshine, Morgan, Jarid, Alec, Paige, and Lauren. The opportunities to do rad things in beautiful places have been so important for my mental health and for reminding me why I wanted to study the Earth in the first place.

VITA

John D. Patterson

EDUCATION:

PhD in Earth System Science, 2022
University of California, Irvine
Irvine, CA

MS in Earth System Science, 2019
University of California, Irvine
Irvine, CA

BS in Chemistry (Summa Cum Laude), 2015
Tufts University
Medford, MA

RESEARCH INTERESTS:

Atmospheric chemistry, biogeochemical cycling, atmospheric hydrogen, paleoclimate, firn air, ice cores

HONORS AND AWARDS:

CalSpace Fellow (2021)
Tufts University Durkee Scholarships (2015)
ACS Undergraduate Award in Inorganic Chemistry (2015)

RESEARCH EXPERIENCE:

2017-Present **Graduate Student Researcher**
University of California, Irvine
Dissertation advisor: Eric Saltzman
Dissertation topic: Understanding past changes in atmospheric H_2 using firn air and ice core measurements.
Technical skill development: trace gas analysis, mass spectrometry, numerical modeling, inversion, and Bayesian data analysis

2014-2015 **Undergraduate Researcher**
Tufts University
Research advisor: Elena Rybak-Akimova

Research topic: Investigating the catalytic properties of pyridine containing organic macrocycles functionalized with a metallic ligand.
Technical skills development: Organic synthesis, UV-vis spectrophotometry.

TEACHING EXPERIENCE

Teaching Assistant, University of California, Irvine; Irvine, CA
Courses:

Spring 2021: Earth System Science 114- Field Methods

Fall 2020: Earth System Science 7- Physical Geology

Spring 2020: Earth System Science 55- Earth's Atmosphere

Fall 2019: Earth System Science 114- Field Methods

Spring 2019: Earth System Science 114- Field Methods

Fall 2018: Earth System Science 17- Catastrophes

Summer 2018: Earth System Science 3- Oceanography

Tutor, STEMtree Learning Center- Vienna, VA

2016: Chemistry and biology

OUTREACH AND LEADERSHIP

2017-Present **CLEAN** (Climate Literacy Education And iNquiry)

CLEAN is a graduate student-run outreach organization. We teach hands-on lessons focused on climate and environmental science at a local underserved middle school. In addition to volunteering as an educator, I joined the board as the treasurer in 2018. I also led the adaptation of two of our lessons for remote delivery during the COVID-19 pandemic.

PUBLICATIONS

Patterson, John D., Aydin, M., Crotwell, A. M., Pétron, G., & Severinghaus, J. P. (2021). H_2 in Antarctic firn air : Atmospheric reconstructions and implications for anthropogenic emissions. *Proceedings of the National Academy of Sciences of the United States of America*, *118*, https://doi.org/10.1073/pnas.2103335118.

Patterson, John D., & Saltzman, E. S. (2021). Diffusivity and solubility of H_2 in ice Ih: Implications for the behavior of H_2 in polar ice. *Journal of Geophysical Research Atmospheres*, *126*, 1–14. https://doi.org/10.1029/2020JD033840.

Patterson, J. D., Aydin, M., Crotwell, A. M., Petron, G., Severinghaus, J. P., & Saltzman, E. S. (2020). Atmospheric History of H_2 Over the Past Century Reconstructed From South Pole Firn Air. *Geophysical Research Letters*, *47*(14), 1–8. https://doi.org/10.1029/2020GL087787.

McKenzie, S. G., Palluccio, T. D., **Patterson, J. D**., & Rybak-Akimova, E. V. (2018). Synthesis,

characterization, and oxidation catalysis studies of a monofunctionalized copper pyridine-aza macrocycle. *Inorganica Chimica Acta*, *482*. https://doi.org/10.1016/j.ica.2018.07.008.

PRESENTATIONS:

Patterson, John D. et al. (2021) Reconstructing the atmospheric history of H_2 from Greenland firn air, oral presentation at the 2021 American Geophysical Union Fall Meeting, Remote

Patterson, John D., et al. (2021) H_2 in Antarctic firn air: atmospheric reconstructions and implications for the budget, poster presentation at the 2021 National Oceanic and Atmospheric Administration Global Monitoring Annual Conference, Remote

Patterson, John D. (2021) Reconstructing the atmospheric history of H_2 from Antarctic firn air, oral presentation at the Oregon State University Paleoclimate Seminar series, Remote

Patterson, John D. et al. (2020) Reconstructing the atmospheric history of H_2 from Antarctic firn air, oral presentation at the 2020 American Geophysical Union Fall Meeting, Remote

Patterson, John D. (2020) Reconstructing the atmospheric history of H_2 from Antarctic firn air, oral presentation at the AirUCI Internal Seminar Series, Remote

Patterson, John D. et al. (2019) Reconstructing the atmospheric history of H_2 from Antarctic firn air, poster presentation at the 2019 American Geophysical Union Fall Meeting, San Francisco, CA

Patterson, John D., et al. (2019) Molecular hydrogen (H_2) in South Pole firn air, poster presentation at the 2019 South Pole Ice Core Meeting, Seattle, WA

Patterson, John D., et al. (2018) Molecular hydrogen in South Pole firn air, poster presentation at the 2018 South Pole Ice Core Meeting, Seattle, WA

ABSTRACT OF THE DISSERTATION

Molecular hydrogen in Earth's atmosphere: reconstructions and interpretation

By

John D. Patterson

Doctor of Philosophy in Earth System Science

University of California, Irvine, 2022

Professor Eric S. Saltzman, Chair

The biogeochemical cycling of atmospheric hydrogen (H_2) is linked to several important aspects of the Earth system including the radiative budget, biomass burning, biogenic hydrocarbon emissions, soil microbial activity, and the oxidative capacity of Earth's atmosphere. As H_2 becomes a more important part of the energy sector, anthropogenic emissions are likely to increase dramatically. Projecting the effects of increasing anthropogenic emissions in a changing climate require a comprehensive understanding of the biogeochemical cycle of H_2. Studying past changes in the atmospheric levels of H_2 is one way to improve understanding of the cycling of H_2 through the Earth system. However, knowledge of past variability in atmospheric H_2 is limited.

In this dissertation, atmospheric H_2 levels over the last century are reconstructed. We conduct laboratory experiments to make the first measurements of the diffusivity of H_2 in ice under conditions relevant to polar ice sheets. Numerical models are used to understand the implications of our results for the mobility of H_2 in polar firn and ice. We show that the partial pressure of H_2 equilibrates between open and closed pores in the firn column, that significant diffusive smoothing of atmospheric variability should be expected in ice core measurements of

H_2 older than a few centuries, and that shallow ice core samples could be analyzed for H_2 for up to a year after drilling without confounding diffusive losses to the atmosphere.

The results of the diffusion experiment are incorporated into a new firn air model. The firn air model is used to reconstruct atmospheric H_2 using measurements from two Antarctic sites and three Greenland sites. The reconstructions show that H_2 levels increased by ~60% over Antarctica and ~40% over Greenland during the 20th century. A simplified atmospheric box model is used to demonstrate that the 20th century increase in H_2 levels is consistent with increasing anthropogenic emissions and increasing photochemical production. This study is the first comprehensive investigation of past changes to the biogeochemical cycling of H_2. Further research is required to confirm the records presented here and to extend the reconstruction of atmospheric H_2 levels further back in time in order to analyze the covariance of climate and H_2.

CHAPTER 1

Introduction

Includes excerpts from:

Patterson, J. D., & Saltzman, E. S. (2021). Diffusivity and solubility of H_2 in ice Ih: Implications for the behavior of H_2 in polar ice. Journal of Geophysical Research Atmospheres, 126. https://doi.org/. https://doi. org/10.1029/2020JD033840

Patterson, J. D., Aydin, M., Crotwell, A. M., Pétron, G., & Severinghaus, J. P. (2021). H_2 in Antarctic firn air: Atmospheric reconstructions and implications for anthropogenic emissions. Proceedings of the National Academy of Sciences of the United States of America, 118. https://doi.org/10.1073/pnas.2103335118/-/DCSupplemental.90

1.1 Overview of this dissertation

Molecular hydrogen (H_2) in the atmosphere plays an important role in atmospheric chemistry and the climate system. The biogeochemical cycling of H_2 is linked to several important components of the Earth system including the radiative budget, biomass burning, biogenic hydrocarbon emissions, soil microbial activity, and the oxidative capacity of Earth's atmosphere. Recently, there has been renewed interest in H_2 in both the scientific and policy communities because of its potential to replace fossil fuels as an energy source. Substituting energy generated from H_2 for fossil fuel energy would drastically reduce anthropogenic emissions of greenhouse gases and air pollutants, provided that the H_2 is produced using renewable energy sources (Derwent et al., 2020; Prather, 2003). Like all small molecules, H_2 is highly diffusive, and widespread implementation of H_2 energy technologies would likely lead to

significant H_2 emissions from leakage (Derwent et al., 2020; Schultz et al., 2003). Projecting the atmospheric accumulation and climate impacts of increasing anthropogenic emissions requires a comprehensive understanding of the biogeochemical cycle of H_2.

Studying past perturbations to the biogeochemical cycling of H_2 can provide insight into its relationship to climate and human activities and increase confidence in projections of the consequences of future anthropogenic perturbations. However, knowledge of past changes in H_2's biogeochemical cycling is limited by the lack of information about past atmospheric variability. Measurements of the aging air trapped in polar firn and ice cores has allowed researchers to determine past atmospheric levels of climatically important gases such as CO_2 and methane (CH_4). These atmospheric histories have revealed tight coupling between climate and atmospheric composition. Furthermore, the reconstructions have allowed researchers to test theories about the biogeochemical cycling of these gases and infer anthropogenic perturbations to atmosphere. Currently no such record of atmospheric H_2 exists because interpretation of H_2 measurements is complicated by H_2's unusually high permeability in ice.

This dissertation focuses on reconstructing the atmospheric variability of H_2 over the last century from measurements on polar firn and inferring changes to the budget over that time span. The study constitutes the first comprehensive investigation of past changes to the biogeochemical cycle of H_2. The research was accomplished by:

1) Conducting laboratory measurements of the solubility and diffusivity of H_2 in ice under conditions relevant to polar ice sheets
2) Investigating how H_2's unusually high permeability affects the interpretation of H_2 measurements in polar firn and ice using numerical models

3) Developing new firn air modeling techniques, which incorporate the results from steps 1) and 2)
4) Reconstructing past atmospheric levels of H_2 over the last 150 years using firn air measurements from Greenland and Antarctica with the new firn air model
5) Inferring past changes to the global biogeochemical cycling of H_2 using a simple atmospheric box model and statistical analyses.

The remainder of chapter 1 is devoted to background information on the biogeochemical cycling of H_2 and gas measurements in polar ice cores. Chapter 2 describes the experimental setup and the results of the H_2 permeability experiments. It also describes the results of numerical modeling undertaken to assess the implications of the permeability measurements for the incorporation of H_2 into an ice sheet. Chapter 3 presents firn air measurements from two sites in Antarctica and the three sites in Greenland, describes the new numerical model used to simulate the movement of H_2 through the firn, and presents reconstructed atmospheric histories of H_2 over Antarctica and Greenland. Chapter 4 describes the atmospheric box model used to simulate the atmospheric distribution and biogeochemical cycling of H_2, and it explores budget scenarios that could explain the firn air reconstructions. Chapter 5 summarized our key findings, provides a broader perspective on this work, and suggests possible future directions for research on H_2 in the Earth system.

1.2 Background

This section describes: 1) the budget and distribution of molecular hydrogen in the atmosphere, 2) the air pollution and climate impacts of the atmospheric chemistry associated with molecular hydrogen, 3) the use of polar firn air and ice cores to reconstruct the composition of the past atmosphere, and 4) challenges and previous work on molecular hydrogen in polar ice.

1.2.1 Budget and distribution of molecular hydrogen in the atmosphere

Molecular hydrogen (H_2) is an abundant and reactive trace gas in Earth's atmosphere. The globally averaged mixing ratio of H_2 in the troposphere is 530 ppb (nmol H_2 mol^{-1} air), and its estimated atmospheric lifetime is 2 years (Ehhalt & Rohrer, 2009; Novelli et al., 1999; Pieterse et al., 2011; Pieterse et al., 2013; Paulot et al., 2021). The budget of atmospheric H_2 is complex with both natural and anthropogenic terms. The largest single source of H_2 is the photolysis of formaldehyde in the atmosphere. Formaldehyde photolysis accounts for almost half of total H_2 sources. Formaldehyde is a photo-oxidation product of methane and other non-methane hydrocarbons (NMHCs) of both anthropogenic and biogenic origin. Formaldehyde photolyzes in the atmosphere in one of two ways:

$$HCHO + h\nu \rightarrow CO + H_2 \quad (1.1a)$$
$$HCHO + h\nu \rightarrow HCO + H \quad (1.1b)$$

Reaction pathway 1.1a, which produces H_2, is slightly favored over reaction pathway 1.1b (Novelli et al., 1999). H_2 is also a product of incomplete combustion. Thus, direct emissions from fossil fuel combustion and biomass burning constitute a significant source. Combined, combustion sources account for ~40% of total H_2 sources. Emission as a byproduct of N_2 fixation, both on land and in the ocean, is a small additional source (Ehhalt & Rohrer, 2009; Novelli et al., 1999; Pieterse et al., 2013; Pieterse et al., 2011). The most important sink of atmospheric H_2 is uptake by soil microbes which accounts for 70% of total losses. Oxidation by the OH radical makes up the balance of remaining losses. Reaction with the OH radical proceeds according to reaction 1.2:

$$H_2 + OH \rightarrow H_2O + H \quad (1.2)$$

Estimates of the modern budget of atmospheric H_2 from several literature sources are given in Table 1.1.

There is 3% more H_2 in the Southern hemisphere than the Northern hemisphere, due to the asymmetry of the soil microbial sink. This interhemispheric difference is opposite that of most trace gases for which direct anthropogenic emissions are an important source. (Novelli et al., 1999; Prather, 2003). H_2 exhibits strong seasonality in the Northern hemisphere with an annual maximum around 530 ppb and an annual minimum around 490 ppb. In the Southern hemisphere, the annual maximum about 550 ppb, and the minimum is around 530 ppb. Interestingly, the hemispheric cycles do not occur 180^o out of phase as is normal for most gases. The annual maximums are separated by only a few months indicating that there is a different primary control on the seasonal cycle of H_2 in each hemisphere (Novelli et al., 1999). Figure 1.1 shows *in situ* measurements of atmospheric H_2 made by the Advanced Global Atmospheric Gas Experiment (AGAGE) at Cape Grim, Tasmania and Mace Head, Ireland from 1994-2018.

The modern instrumental record of tropospheric H_2 abundance began in the late 1980's (Khalil & Rasmussen, 1990; Novelli et al., 1999). Mid-20^{th} century studies reported a wide range (400-2000 ppb), which likely reflects analytical issues and/or influence from urban pollutants (Ehhalt et al., 1977; Paneth, 1937; Schmidt, 1974). The surface flask air measurements of Khalil & Rasmussen (1990), the National Oceanic and Atmospheric Administration's Global Monitoring Laboratory (NOAA/GML; Novelli, 2006; Novelli et al., 1999), and the Commonwealth Scientific and Industrial Research Organisation (CSIRO; Langenfelds et al., 2002) show atmospheric levels of H_2 of 510-550 ppb during the late 20^{th} and early 21^{st} centuries at background sites around the world. *In situ* measurements from Cape Grim, Tasmania and Mace Head, Ireland made by AGAGE show similar levels of atmospheric H_2 during the same

time period (Prinn et al., 2019; Figure 1.1). The data show a small increasing trend in atmospheric H_2 in the southern hemisphere during 1990's with stable levels thereafter. In the northern hemisphere, the flasks show no discernible trend since the early 1990's.

Measurements of atmospheric H_2 have been subject to challenging calibration drift (Jordan & Steinberg, 2011). It is believed that H_2 outgasses from the high-pressure aluminum cylinders commonly used to make the calibration standards for atmospheric measurements. Presently, the World Meteorological Organization recommends reporting H_2 measurements on the MPI09 (also referred to as the WMO H_2 X2009) scale maintained by the Max Plank Institute for Biogeochemistry, Jena, Germany. The MPI09 scale is calibrated against standards made in electropolished stainless steel Essex cylinders. In 2013, measurements made by AGAGE and CSIRO were revised from the CSIRO94 scale to the MPI09 scale by applying a correction of ~3%. Since that time, those organizations have reported measurements on the MPI09 scale. NOAA/GML is currently in the process of revising their H_2 measurements from the NOAA96 scale to the MPI09 scale. Matched flask measurements suggest that the bias in NOAA/GML measurements relative to AGAGE and CSIRO measurements was -1% during the mid-1990's, but, by 2015, the absolute bias increased to -5%.

Table 1.1 - Estimates of the modern budget of atmospheric H_2 from several references.

	Novelli et al. (1999)	**Price et al. (2007)**	**Ehhalt & Rohrer (2009)**	**Pieterse et al. (2011)**
Sources (Tg y^{-1})				
Anthropogenic emissions[a]	15 ± 10	22.7	11 ± 4	$17.0\pm^{3}_{6}$
Biomass burning	16 ± 5	10.1	15 ± 6	15 ± 5
Land N_2 fixation	3 ± 1	0	3 ± 2	$3.0\pm^{3}_{3}$
Ocean N_2 fixation	3 ± 2	6.0	6 ± 3	$5.0\pm^{3}_{2}$
Photochemical production	40	34.3	41 ± 11	37.3
From CH_4	26 ± 9	24.5	23 ± 8	
From NMHCs[b]	14 ± 7	9.8	18 ± 7	
Total	**77 ± 16**	**73**	**76 ± 14**	**77.3**
Sinks (Tg y^{-1})				
Soil uptake	56 ± 41	55	$60\pm^{30}_{20}$	55.8
OH oxidation	19 ± 5	18	19 ± 5	22.1
Total	**75 ± 41**	**73**	$\mathbf{79\pm^{30}_{20}}$	**77.9**

*Also see Paulot et al., 2021

[a] Includes only direct emissions from fossil fuel and biofuel burning

[b] Includes biogenic and anthropogenic NMHCs

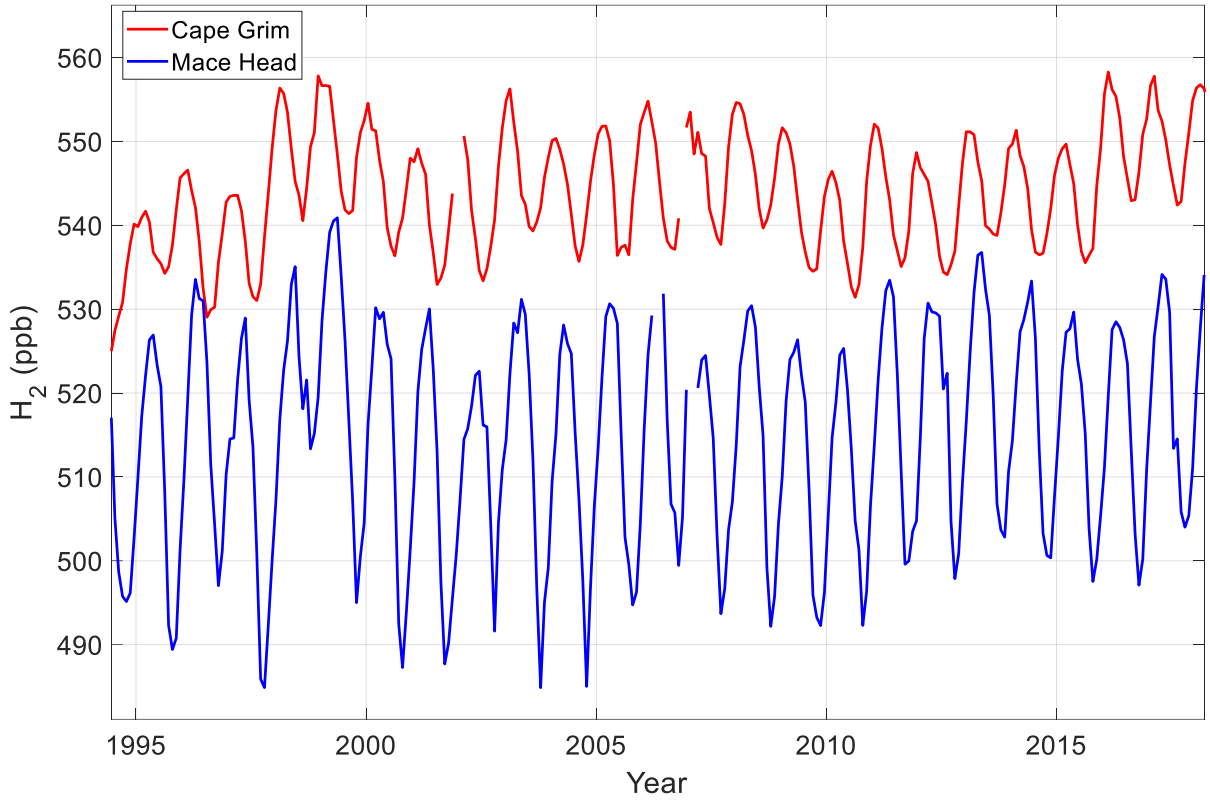

Figure 1.1- Monthly averaged H_2 mixing ratios from *in situ* measurements over Cape Grim, Tasmania (red) and Mace Head, Ireland (blue) made by AGAGE (Prinn et al., 2019)

1.2.2 Atmospheric chemistry, climate, and air quality impacts of H_2

The atmospheric abundance of H_2 has links to climate and air quality. Much like carbon monoxide (CO), H_2 is an indirect greenhouse gas and ozone (O_3) precursor (Figure 1.2). The oxidation of H_2 results in reduced levels of OH radicals. The OH radical is the primary removal mechanism for atmospheric hydrocarbons, including methane, a powerful greenhouse gas. By reducing OH levels, atmospheric H_2 extends the atmospheric lifetime of methane and increases the climate warming associated with atmospheric methane. Thus, although it is not radiatively active, H_2 acts as an indirect greenhouse gas via its effect on the atmospheric lifetime of methane.

Atmospheric levels of H_2 can also affect air quality. The H atom produced in reaction 1.2 leads to the production of HO_2 (reaction 1.3). Additional H_2 causes a shift from OH to HO_2, and this shift in the balance between HO_x species influences ozone chemistry. In the polluted parts of the troposphere, where high levels of NO_x (NO and NO_2) are present, H_2 provides the "fuel" necessary for the catalytic generation of ozone, which is a potent air pollutant and greenhouse gas:

$$H_2 + OH \rightarrow H_2O + H \quad (1.2)$$
$$H + O_2 \rightarrow HO_2 \quad (1.3)$$
$$HO_2 + NO \rightarrow OH + NO_2 \quad (1.4)$$
$$NO_2 + h\nu \rightarrow NO + O(^3P) \quad (1.5)$$
$$O(^3P) + O_2 \rightarrow O_3 \quad (1.6)$$

Net: $$H_2 + 2O_2 + h\nu \rightarrow O_3 + H_2O \quad (1.7)$$

Atmospheric H_2 also affects stratospheric water vapor content. The oxidation of H_2 results in the net production of water vapor. While this process has a negligible impact on total water vapor content in the relatively moist troposphere, it can have a large impact in the exceedingly dry air of the stratosphere. Additional water vapor in the stratosphere cools the stratosphere and warms the troposphere (Solomon et al., 2010). The cooling of the stratosphere combined with increased water vapor content could also enhance stratospheric ozone depletion through an increase of polar stratospheric clouds although this effect depends largely on the continued presence of chlorofluorocarbons (Tromp et al., 2003). In summary, atmospheric H_2 abundance plays a role in climate, ozone pollution, and stratospheric chemistry.

H_2 is an attractive alternative to fossil fuels as an energy source. The idea that H_2 could be used to generate a substantial proportion of our energy in the future has been coined the

"hydrogen economy." The use of H_2 electrochemical cells produces only water vapor as a waste product. Substitution of H_2 electrochemical cells for fossil fuels as an energy source would dramatically reduce carbon emissions and the emission of air pollutants such as NO_x and aerosols, provided that the H_2 is generated from renewables (Tromp et al., 2003; Prather, 2003). This reduction in carbon emissions and air pollutants is the primary reason that H_2 is considered to be an attractive alternative fuel. However, H_2 is a highly diffusive because of its small molecular diameter. It has been estimated that, if 50% of the energy obtained from combustion of fossil fuels was instead obtained from clean H_2 electrochemical cells, atmospheric levels of H_2 could increase by as much as 600 ppb through diffusive losses from storage tanks (Schultz et al. 2003). This would correspond to a radiative forcing of 0.026 W m^{-2} due to H_2's previously discussed role as a sink for OH radicals (Prather, 2003). For comparison, total current anthropogenic forcing is estimated to be 2.7 W m^{-2} (Forster et al., 2021). Additionally, it has been estimated that an increase of 500 ppb in total atmospheric H_2 content would produce enough stratospheric water vapor to cool the stratosphere by 0.5ºC (Tromp et al. 2003).

A more recent modeling study investigated the radiative effects of the complete replacement of fossil fuel energy with hydrogen fuel cells (Derwent et al., 2020). Those researchers estimated that, with a 10% H_2 leakage rate, the transition to a hydrogen economy would reduce anthropogenic radiative forcing by 95% relative to the continued use of fossil fuels over a 100-year time horizon. Similarly, Wang et al. conducted a detailed modeling study to examine the effects of an H_2 based road-transportation sector on ozone chemistry and air pollution (Wang et al., 2013a, 2013b). That research found that adoption of H_2 based road-transportation decreases tropospheric air pollution under all scenarios. Assuming a 2.5% leakage rate, implementation of hydrogen fuel cell technology for road-based transportation would

reduce tropospheric ozone concentrations by 5%-7% and CO concentrations by 4-14%. Adoption of hydrogen internal combustion engines would decrease tropospheric ozone concentrations by 1% and decrease the tropospheric CO burden by 7-17%. Again, assuming a 2.5% leakage rate, those researchers found that an H_2-based road transportation sector would decrease stratospheric ozone by at most 0.5%.

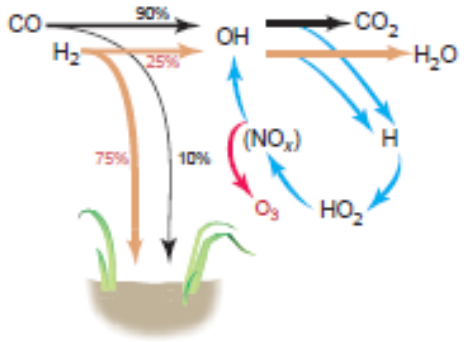

Figure 1.2- Schematic of the role of H_2 as an ozone precursor and indirect greenhouse gas. Much like CO, H_2 reacts to generate ozone in the presences of NO_x and acts as a sink for the OH radical (figure from Prather, 2003).

1.2.3 Polar firn and ice cores as an archive of past atmospheric composition

Samples of aging air trapped in polar firn and ice are commonly used to reconstruct the composition of the past atmosphere on timescales ranging from decades to hundreds of thousands of years (eg. Alley, 2000; Brook & Buizert, 2018). The firn is the porous layer of densifying snow that comprises the upper 60-120 m of an ice sheet (Figure 1.2). Bulk density increases with depth, and total porosity decreases. Additionally, as depth increases, open pores are progressively sealed into closed bubbles, which are isolated from the atmosphere and the air in the open porosity. In firn air research, the aging air from the open porosity in the firn column is sampled and analyzed. The composition of the air in the open porosity of the firn column is controlled by several processes (Schwander et al., 1993; Severinghaus et al., 2001; Severinghaus

& Battle, 2006; Trudinger et al., 1997). Near the surface (<10 m), the firn air is well-mixed with the atmosphere due to convective mixing.

The region below the convective zone is known as the diffusive column. The diffusive column typically extends to a depth of 60-120 m depending on site characteristics such as accumulation and temperature. In the diffusive column, gas transport is primarily driven by molecular diffusion, which acts to decrease concentration gradients. The average age of the air in the open pores increases with depth. However, the age of the air at a given depth in the firn column does not correspond to a single year; rather, firn air composition reflects the past atmospheric composition integrated over an age distribution. The age distribution for a given gas depends primarily on the molecular diffusivity of that gas. The age distribution of a slow-diffusing gas at a given depth is older and broader than the age distribution of a fast-diffusing gas. Additionally, gas composition in the diffusive column is affected by gravitational fractionation. Gravitational fractionation describes the differential gravitational settling of various gases based on their molecular weight. Gas species that are heavier than air are enriched with depth while lighter gas species are depleted with depth. This process is well-described by the barometric equation (Schwander et al., 1993).

The bottom part of the firn is known as the lock-in zone. In the lock-in zone, vertical gas diffusion is inhibited by the presence of impermeable seasonal layers (M. O. Battle et al., 2011; Severinghaus & Battle, 2006). In this zone, gas transport is dominated by advection as new snow at the surface compresses and buries the older firn. The bottom of the lock-in zone is termed the firn-ice transition. At the firn-ice transition, no open porosity remains, and any remaining gas is trapped in closed bubbles in the ice matrix. The air contained in the bubbles ages at the same rate as the surrounding ice. At warmer, high-accumulation sites, the firn-ice transition generally

occurs at shallower depths, whereas at colder low-accumulation sites, the firn-ice transition is generally deeper. Therefore, the age distribution of air trapped in bubbles at the firn-ice transition is narrower and younger at high-accumulation sites than at low accumulation sites. Furthermore, the age difference (or delta age) between the air trapped in the bubbles and the surrounding ice is smaller at high-accumulation sites than at low-accumulation sites.

Polar ice cores are a unique continuous record of Earth's atmosphere and climate. Samples of the air extracted from polar ice cores have been used to reconstruct atmospheric composition on timescales of up to 800,000 years. Similarly, water isotopes ($\delta^{18}O$ and δD) and other proxies have been used to infer past temperature variability and other important climate parameters (Figure 1.4). Ice core records have provided valuable insight into the Earth system and revealed tight coupling between the global climate and atmospheric composition over the last several glacial/interglacial cycles (Brook & Buizert, 2018).

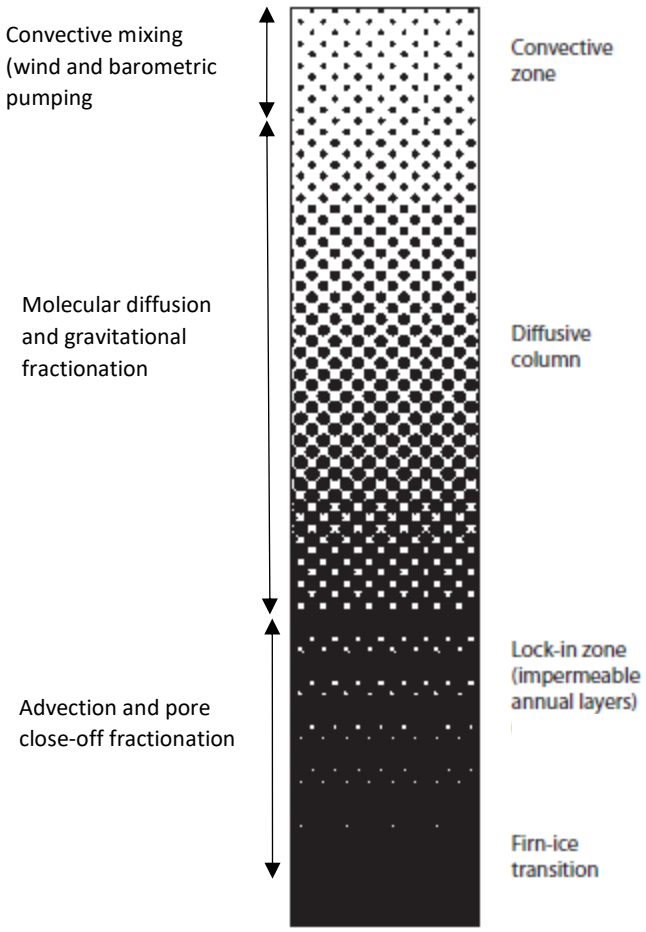

Figure 1.3- A simplified schematic of the firn column, adapted from Battle et al., 2011. On the right are the regions of the firn described in the text. On the left are the primary gas transport mechanisms, which control the composition of the air in the open pores in each region.

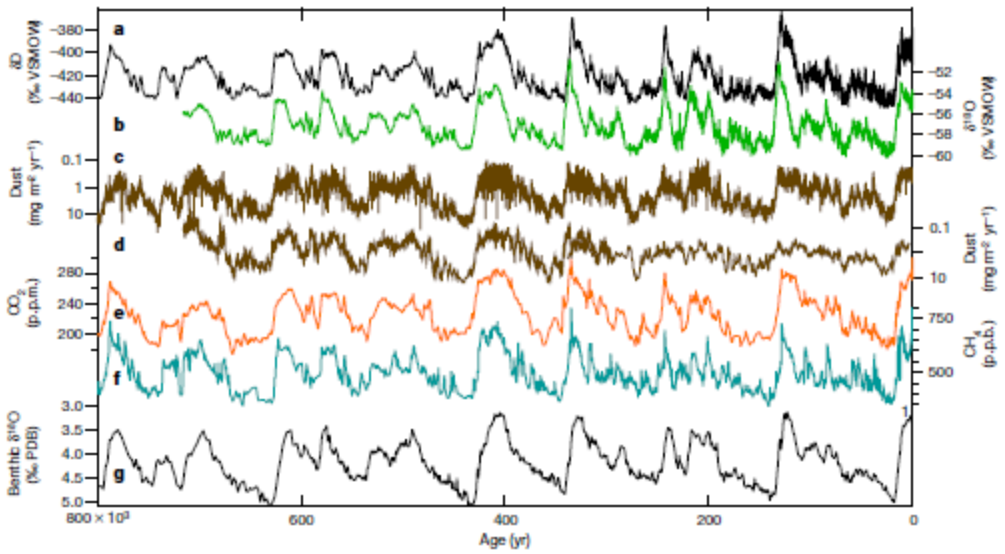

Figure 1.4- An 800,000 year record of atmospheric change and climate proxies from Antarctic ice cores and the benthic $\delta^{18}O$ stack from Brook & Buizert, 2018. Glacial/interglacial cycles are clearly visible as periodic, simultaneous fluctuations in the data. a) EPICA Dome C δD of water relative to VSMOW (Vienna Standard Mean Ocean Water); b) Dome Fuji $\delta^{18}O$ of water; c) & d) dust records from Epica Dome C and Dome Fuji respectively; e) & f) Epica Dome C/Vostok CO_2 and CH_4 records; g) benthic $\delta^{18}O$ stack relative to PDB (Pee-Dee belemnite standard).

1.2.4 H_2 in polar firn and ice

There are several unique challenges associated with the analysis of H_2 in polar firn and ice cores due to its small molecular diameter (2.89 Å). Gas molecules with small kinetic diameters (<3.60 Å) are highly permeable in ice. Dissolution and diffusion of H_2 through the ice lattice can affect the composition of firn air and ice core bubbles through several mechanisms. Pore close-off fractionation is a process that takes place in the firn column. It refers to the gradual pressurization of closed bubbles, which drives a diffusive flux of gases between bubbles into open pores (Figure 1.5; Huber et al., 2006; Ikeda-Fukazawa et al., 2005; Severinghaus & Battle, 2006). Significant enrichment of small, diffusive gases has been measured in the open pores at the base of the firn air lock-in zone where vertical gas phase diffusion within the open porosity is inhibited by impermeable winter layers. These impermeable layers allow much steeper concentration gradients to exist in the open porosity in the lock-in zone. For example, Severinghaus & Battle (2006) reported that firn air samples from the base of the lock-in zone were enriched in ^{22}Ne by as much as 10%. This enrichment must be considered in firn air analyses of small diffusive gases. Pore close-off fractionation begins well above the lock-in zone, leading to upward diffusion of the fractionated gas. As a result, ice core bubbles must be depleted in mobile gases such as Ne and H_2, relative to the overlying atmosphere.

A second process involves the vertical migration of diffusive gases within the ice sheet. The internal pressure of air bubbles increases with depth below the firn/ice transition in response to the increasing hydrostatic pressure. The resulting increase in partial pressure of H_2 in the bubbles causes dissolution of H_2 from the bubble into the ice. This creates a vertical concentration gradient of H_2 in the ice and a net upward flux of H_2 in the ice sheet even in the case of constant atmospheric H_2 levels. The increase in H_2 partial pressure with depth likely

continues until the bubble/clathrate transition is complete and no H_2 is present in the gas phase. This phenomenon has been observed previously with He (Craig & Chou, 1982; Jean-Baptiste et al., 1993, 2001). Furthermore, vertical diffusion will reduce H_2 gradients and smooth the H_2 atmospheric history recorded in an ice sheet

A third challenge involves post-coring sample treatment and storage. After an ice core has been drilled and brought to the surface, H_2 within the ice begins to equilibrate with the surrounding atmosphere. The rate of this process dictates the procedures required to sample ice cores for analysis of paleoatmospheric H_2 levels. As described previously, the hydrostatic compression of bubbles at depth drives H_2 from the bubbles into the ice. This effect causes newly drilled ice to be supersaturated with respect to atmospheric H_2. A similar phenomenon occurs for He, and post-coring diffusive losses for He have been estimated to be as much as 10% within 15 minutes of drilling and recovery (Jean-Baptiste et al., 1993, 2001). Haan (1996) reported measurements of H_2 in several stored ice cores, showing that the measured H_2 levels are roughly consistent with full equilibration with the ambient atmosphere in the storage freezer.

There is one previously published investigation of the historical trends in atmospheric H_2 using measurements from firn air in Greenland. Petrenko et al. reconstructed northern hemisphere H_2 (Petrenko et al., 2013). Their results show an increase in atmospheric H_2 levels from 450-520 ppb during the 1960's to a peak near 550 ppb during the late 1980's or early 1990's, then, a recent decline to about 515 ppb in 2010 (Figure 1.6). The peak and recent decline are inconsistent with modern flask measurements that show roughly constant H_2 levels during the 1990's (Novelli, 2006; Novelli et al., 1999; Prinn et al., 2019). The authors note that the firn air model used for the reconstruction does not include pore close-off fractionation of H_2, and it is

possible that the inferred peak is an artifact of this process (Petrenko et al., 2013; Severinghaus & Battle, 2006).

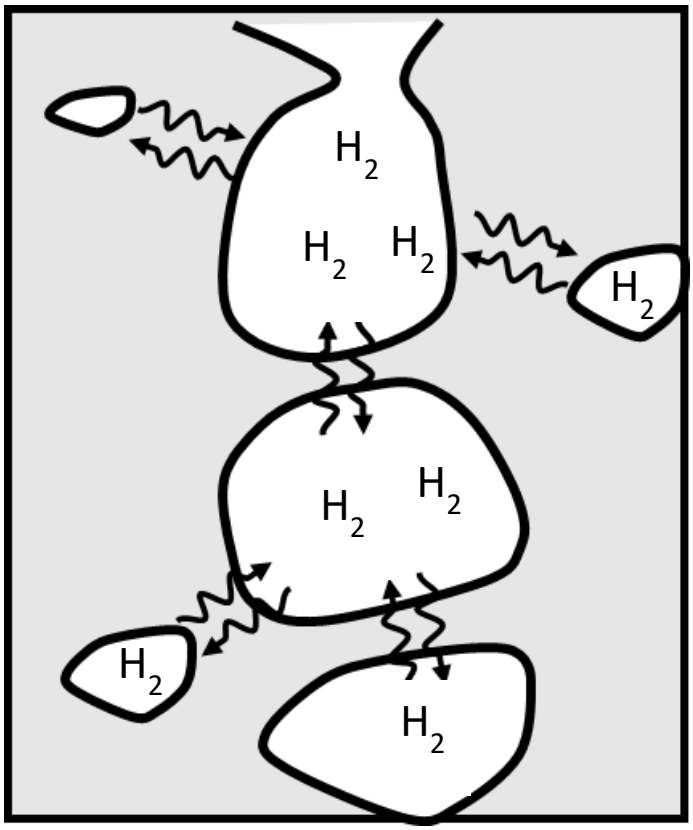

Figure 1.5- A schematic of pore close-off fractionation, adapted from Severinghaus & Battle 2006. Diffusive exchange between closed, pressurized bubbles and open pores causes enrichment in small diffusive gases, like H_2, in the open pores

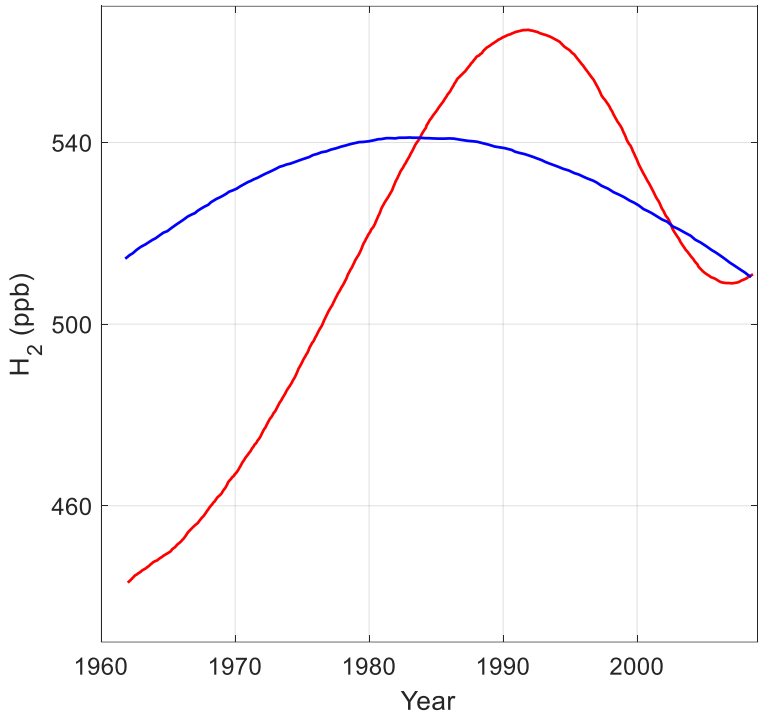

Figure 1.6- Reconstructions of atmospheric H_2 using firn air measurements at NEEM, Greenland using two different firn air models from Petrenko et al. (2013). The histories have been adjusted from the NOAA96 to the MPI09 calibration scale.

CHAPTER 2

Diffusivity and solubility of H_2 in ice Ih: Implications for the behavior of H_2 in polar ice

Includes excerpts from:

Patterson, J. D., & Saltzman, E. S. (2021). Diffusivity and solubility of H_2 in ice Ih: Implications for the behavior of H_2 in polar ice. Journal of Geophysical Research Atmospheres, 126. https://doi.org/. https://doi. org/10.1029/2020JD033840

2.1 Overview

This chapter describes the measurement of the diffusivity and solubility of H_2 in ice and discusses the implications of those measurements. The experimental setup is detailed, and the results of those laboratory experiments are presented. Numerical models are used to assess how the permeability of H_2 affects measurements in polar firn and ice. This research was published in Patterson & Saltzman (2021).

2.2 Introduction

The polar ice sheets contain a unique archive of ancient air that can be used to reconstruct atmospheric composition on timescales from decades to hundreds of thousands of years. Reconstructing paleoatmospheric trace gas levels requires an understanding of how trace gases are incorporated into the ice sheet and how they evolve in time as a function of burial depth and temperature (eg. Etheridge et al., 1996, 1998). Gas molecules with small kinetic diameters (<3.60 Å) are highly permeable in ice, and information about the solubility and diffusivity of such gases in ice is needed to develop physical models of gas transport in the ice sheet (Huber et al., 2006; Ikeda-Fukazawa et al., 2005; Patterson et al., 2020; Severinghaus & Battle, 2006). For example, firn air enrichments in Ne/N_2 and O_2/N_2 relative to atmospheric ratios have been

observed as a consequence of bubble compression and diffusion into the open pores of the firn (Severinghaus & Battle, 2006). Bubble compression below close-off depths can lead to vertical migration of diffusive gases in the ice sheet (Ahn et al., 2008; Craig & Chou, 1982; Jean-Baptiste et al., 1993, 2001). Permeability of small gases can also lead to changes in trace gas composition during storage of ice core samples. Such changes have been observed for O_2/N_2 ratios, He, and H_2 (Bender et al., 1995; Bereiter et al., 2009; Haan, 1996; Jean-Baptiste et al., 1993, 2001; Severinghaus & Battle, 2006). Gas diffusion between bubbles and clathrates in the bubble-clathrate transition zone is also responsible for small scale variability in ice core CO_2 and O_2/N_2 measurements. (Lüthi et al., 2010). These high frequency variations are smoothed by diffusion deeper in the ice sheet.

This study is focused on the solubility and diffusivity of molecular hydrogen (H_2) in ice. H_2 is one of the most abundant trace gases in the atmosphere, with a global mean level of 530 ppb (Novelli et al., 1999). Atmospheric histories of H_2 from firn air and ice cores would provide insight into the biogeochemical cycle of H_2 and its relationship to climate and human activities. Firn air H_2 records from Greenland and Antarctica show significant changes in atmospheric H_2 over the past century (Petrenko et al., 2013; Patterson et al., 2020). Quantitative information about the mobility of H_2 in ice is required in order to interpret firn air and ice core records (Patterson et al., 2020).

Relatively little work has been published on the physical properties of H_2 in ice. The solubility of H_2 in ice near the melting point has been measured over a wide pressure range (Ildyakov & Manakov, 2014; Manakov et al., 2017; Namiot & Gorodetskaya, 1969). No measurements have been made at the lower temperatures relevant to polar ice core sites. Strauss et al. (1994) published an estimate of the diffusivity of H_2 in D_2O ice at temperatures of 25-60 K.

Here, we conduct laboratory measurements of the permeability of H_2 in synthetic polycrystalline hexagonal ice (Ih) over a wide temperature range (199-253 K) and analyze the data to estimate H_2 solubility and diffusivity. Implications of the results are discussed in terms of 1) H_2 behavior in firn air, 2) H_2 mobility with depth in the ice sheet, and 3) sampling/storage of ice core samples for H_2 analysis.

2.3 Experimental methods

2.3.1 Quantification of H_2 in air

H_2 was analyzed in the air streams from the diffusion cells using gas chromatography with pulsed-discharge helium photoionization detection (GC- Agilent 7890A; Valco Instruments D-3-I-7890 HePDD; Novelli et al. 2009). The air stream was directed through a stainless steel sample loop (3 mL loop of coiled 1/8" stainless steel tubing) and vented to the atmosphere. The loop was periodically (12-minute intervals) injected into the He carrier gas stream of the gas chromatograph. Chromatographic separation was carried out on isothermal packed columns consisting of two HayeSep DB 100/120 mesh -packed stainless steel columns operated in series (Table 2.1). The first column was operated as a precolumn and switched out of the carrier flow 4 minutes after injection to prevent less volatile compounds from reaching the detector. A valve was mounted just before the detector to divert major components of air (O_2, N_2, Ar) from the detector as they eluted from the columns. The retention time for H_2 on the system is 3.7 minutes.

The system was calibrated using gas mixtures of 163-620 ppb H_2 in N_2 (ppb= nmol H_2/mol air) prepared in our laboratory in high pressure aluminum cylinders. The detector response is linear in H_2 (R^2 =.99). Under the conditions of these experiments (3 mL sample loop at atmospheric pressure), reproducibility is estimated at 1.5% (1σ) and the limit of detection (2 x the 1σ uncertainty in the intercept of the calibration curve) is estimated at 9 ppb.

Table 2.1. Chromatographic parameters for the GC-HePDD analytical system

Carrier Gas	99.999% pure He (Airgas Inc., Santa Ana CA)
Precolumn	5 m x 1/8 in. OD HayeSep DB 100/120 mesh
Analytical Column	5 m x 1/8 in. OD HayeSep DB 100/120 mesh
Oven Temperature	50^{o} C
HePDD Temperature	100^{o} C
Column Flow Rate	35 mL min^{-1}
Discharge gas flow rate	3 mL min^{-1}

2.3.2 Experimental design

This study was carried out using a "block degassing" method. This involves exposing a block of ice (1.5 x 1.5 x .5 cm) to a pure H_2 atmosphere for several hours, (referred to as "charging") then replacing the H_2 with air and monitoring the H_2 outgassing as a function of time. This is similar in principle to methods used in prior studies of gas diffusion in ice (e.g. Noguchi et al., 2019; Satoh et al., 1996). In those studies, outgassing was carried out in a sealed evacuated chamber and quantified by monitoring the change in total cell pressure. Here outgassing was carried out in a flow of Ultra-zero air at a pressure of 1 atm and quantified by measuring the air flow rate and mole fraction of H_2 in the air exiting the diffusion chamber.

Experiments were carried out over a range of temperatures maintained to $<\pm.05$ K using three configurations. Experiments at 199.2 -204.2 K were carried out in a temperature-controlled polystyrene foam box placed inside an outer insulated box containing dry ice. The polystyrene foam box contained an air-circulating fan, thermistor, and heater, with temperature control provided by a thermistor signal amplifier and Newport process controller. Experiments at 227.2 K were carried out in a low temperature freezer with digital temperature control (Scientemp Corp.). Experiments at 252.7 K were carried out in the temperature-controlled box placed inside

a 249 K walk-in freezer. In this configuration, eutectic ice packs were placed in the polystyrene foam box to prevent temperature drift during defrost cycles.

The ice block is placed in a stainless steel "charging" chamber made from a KF-25 nipple sealed with Viton O-rings. Once the chamber and ice thermally equilibrate at the experimental temperature, a flow of pure H_2 is maintained for 12-72 hours (5 mL min^{-1} STP; P= 1 atm). Subsequently, the sample is manually transferred to a second stainless steel "outgassing" chamber, sealed by Conflat flanges with copper gaskets (Figure 2.2). The second chamber is never exposed to pure H_2 to avoid outgassing of H_2 from chamber walls. A stainless steel cylinder was placed in the outgassing chamber to minimize dead volume. A mass flow controller regulates a flow of Ultra-zero air into the temperature control box through a coil of copper tubing, and into the outgassing chamber (10 mL min^{-1} STP; P= 1 atm). The outflow from the outgassing chamber is routed to the GC/HePDD injection loop and analyzed for H_2 every 12 minutes. All tubing is 1/8" copper. The experiment is terminated when the H_2 levels in the air flow approach the limit of detection of the analytical system, about 24 hours depending on ice sample size and H_2 exposure time.

During both the charging and outgassing phases of the experiment, the gas flows are pre-equilibrated with the experimental temperature by passage through a 2 m coil of copper tubing prior to reaching the chamber. For experiments carried out at 253 K, the Ultra-zero air flow was pre-saturated with water vapor prior to entering the outgassing chamber. This was done to minimize mass loss of the ice block to sublimation which would otherwise have been about 1% over 24 hrs. The pre-saturation chamber consisted of a stainless steel KF-25 nipple sealed with Viton O-rings that contained a similarly prepared block of ice. The pre-saturation chamber and

ice was never exposed to pure H_2. The pre-saturation chamber was not required for experiments at colder temperatures.

Care was taken to avoid air inclusions during the preparation of the ice. First, a ¼" sheet of copper was precooled to -47° C and ultra-pure Milli-Q water was degassed by boiling for 15 minutes. At room temperature, a square nylon tube with 0.3 cm thick walls, a 1.5 cm x 1.5 cm inner cross section, and ~4 cm length is placed on the cold copper. 6 mL of hot water is pipetted into the square tube, and the water freezes from the bottom, excluding any remaining dissolved gas into the liquid above. After ~10 minutes, the remaining liquid water is poured off the top of the tube, and the ice is pressed out of the tube by hand. The top of the ice is then melted back to the desired thickness and simultaneously blotted with a Kimwipe to remove meltwater. The samples used in this study were typically 0.5 cm in thickness. The ice appears bubble-free under magnifications that reveal bubbles with diameters greater than 10 μm. While the presence of smaller bubbles cannot be ruled out completely, we estimate that undetected bubbles could bias the measured diffusivity and solubility high by not more than 5-10%. Examination of a thinner (~.5 mm) similarly prepared ice sample under a cross polar microscope revealed polycrystalline ice with a typical crystal size of ~.3 mm (Figure 2.1). The c-axes of the crystals are randomly oriented

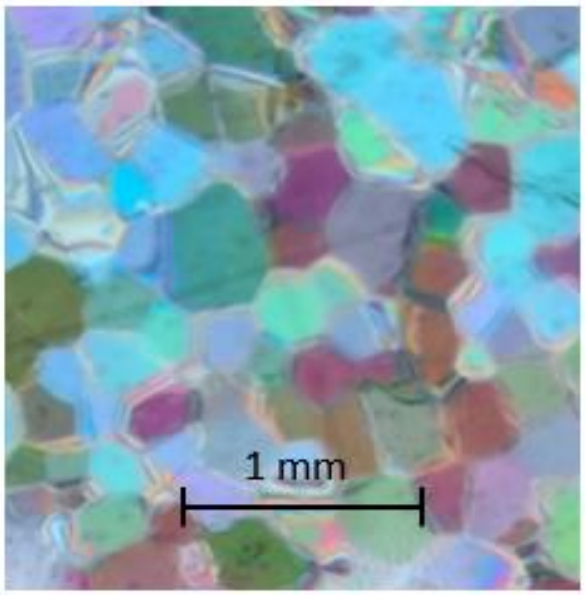

Figure 2.1- A piece of ice prepared as described in 2.1.1 imaged under a cross-polar microscope. This piece was thinned to about 0.5 mm for imaging.

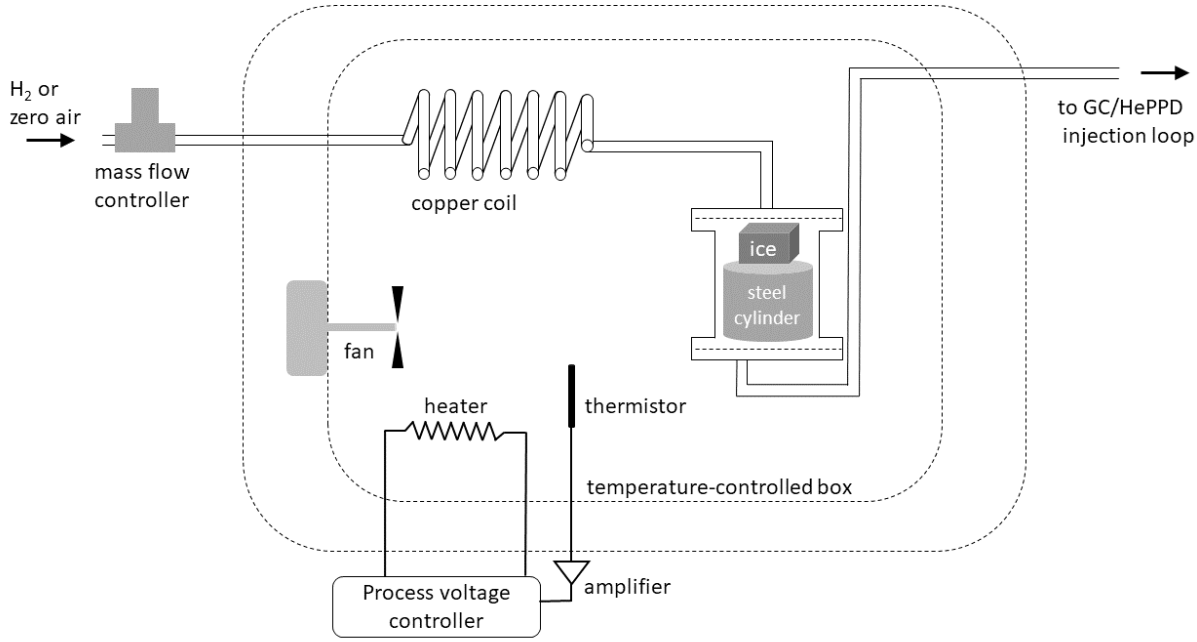

Figure 2.2- Schematic of the laboratory setup used to measure H_2 permeation from ice

2.3.3 Data analysis

There are no published analytical solutions for diffusion from a rectangular block of finite dimensions. To analyze the experimental results, we used a 3-dimensional time-dependent finite-difference diffusion model. The model domain is the entire block of ice. A model grid is constructed with the unique length, width, and height of the ice blocks used in each experiment (*L*, *W*, and *H*). Non-uniform grid spacing is used to provide high resolution at the edges of the box where the strongest concentration gradients are present while minimizing computational costs. In the center of the model domain, ($x=L/2$, $y=W/2$, $z=H/2$) normalized spacing (i.e. $\Delta x/L$) is 0.0385, 0.0385, and 0.0714 in the *x*, *y*, and *z* dimensions. Normalized grid spacing decreases linearly to .0015, .0015, and .0055 at the outer boundaries (i.e. $x=0$, $x=L$). The governing equation for the model is Fick's second law:

$$\frac{\partial C}{\partial t} = D\nabla^2 C \tag{2.1}$$

Where C (mol m^{-3}) is the concentration of H_2 in the ice and D ($m^2\ s^{-1}$) is the diffusivity constant of H_2 in ice. A Dirichlet boundary condition is imposed where the concentration in the boxes at the edge of the domain is prescribed. During the charging period, the concentration at the edges is $C=X*P$, the product of solubility (X, mol m^{-3} Pa^{-1}) and partial pressure of H_2 (P, Pa). During the outgassing period, the concentration is zero. The model calculates the instantaneous rate of H_2 outgassing from the block as a function of time, diffusivity, and solubility ($G_{mod}(t,D,X)$; mol s^{-1}) by integrating the concentration of H_2 over the entire domain at each time step and dividing by the duration of the time step. The model does not account for adsorption of H_2 on the ice surface. Adsorption of H_2 on ice is negligible above 30 K (Kristensen et al., 2011) and

sublimation from the ice surface would likely rapidly desorb any H_2 from the surface before the first injection into the GC/HePDD.

A fourth order Runge-Kutta integration scheme and a fixed time step of 1 s are used for the first 100 s of both the charging and outgassing periods when concentration gradients in the ice block are large. After 100 s, an adaptive Runge-Kutta-Fehlberg time stepping scheme is used to increase computational speed (Matthews & Fink, 2004). The time step increases to ~2000 s by the end of each period when the concentration gradient is drastically reduced. A typical simulation for the conditions used in this study takes about 10 s, executing in MATLAB on an Intel Core-i7 processor running Windows 10. The model iterates over many combinations of solubility and diffusivity to optimize the fit of the modeled rate of outgassing to the measured rate of outgassing. We calculate the rate of H_2 outgassing from the ice ($G(t)$, mol s^{-1}) based on the measured mole fraction on the downstream side:

$$G(t) = H_2(t) * \frac{P_{air}F_{air}}{RT} \tag{2.2}$$

Where $H_2(t)$ is the time variant measured mole fraction, P_{air} is the air pressure in the outgassing cell (1 atm), F_{air} is the volumetric flow of air through the sample loop, T is the temperature of the sample loop, and R is the ideal gas constant

2.4 Results

The raw data time series resulting from a block degassing experiment is shown in Figure 2.3a. H_2 levels in the air flow were initially ~1000 ppb and declined with an initial rate of decrease of roughly 400 ppb hr^{-1}. After 24 hours, H_2 levels were on the order of 100 ppb and the rate of decrease had slowed to 10's of ppb hr^{-1}. The optimum diffusivity, solubility, and permeability (P) constants for each experiment were determined using the 3-dimensional diffusion model described in section 2.3.3). Optimization was carried out by running the model

in forward mode using a grid of diffusivity and solubility values. Probabilities are assigned to each combination of diffusivity and solubility by assuming that the residuals between the modeled and measured H_2 levels are normally distributed with a variance equal to the analytical uncertainty:

$$Prob\ (D,X) = \frac{1}{(\sigma\sqrt{2\pi})^N} e^{\frac{-1}{2\sigma^2}\sum_{t_0}^{t_N}(G_{mod}(t,D,X)-G\,(t))^2} \quad (2.3)$$

Where σ is the analytical uncertainty, and N is the number of samples in the run. The summation is performed over all sampling times. This process results in a two-dimensional probability distribution (Figure 2.3b). Permeation is well constrained by the block degassing experiments, with a relative uncertainty of roughly ±10% for the higher temperatures and ±30% at lower temperatures.

The fit between the model and the experiment allows the permeability to be partitioned into diffusivity and solubility. Marginalized probability distributions for diffusivity and solubility are obtained by integrating the two-dimensional probability distributions over the alternate dimension (Figures 2.3c and 2.3d). These are considerably broader than that for permeability because the inferred diffusivity and solubility from any given experiment are highly correlated (in a negative sense). For example, a low diffusivity constant paired with a high solubility constant can yield a similar modeled result to that from a high diffusivity constant paired with a low solubility constant. The relative 1σ uncertainties for diffusivity and solubility are roughly 30% at warmer temperatures and 50% at colder temperatures. These uncertainties are slightly skewed, resulting in asymmetrical uncertainties (Figure 2.3, Table 2.2).

In total, 17 experiments were conducted using two different blocks of ice. These experiments were carried out at temperatures ranging from 199 - 253 K. The results are tabulated in Table 3.1 and plotted in Figure 3.2. Optimized diffusivity constants ranged from 4.8-22.7*10^{-12} m^2 s^{-1} and showed no temperature dependence. Optimized solubility constants ranged from 4.4-22.6*10^{-7} mol m^{-3} Pa^{-1}. The solubility data shows a strong temperature dependence. Optimized permeabilities ranged from 7.9-38.0*10^{-18} mol m^{-1} Pa^{-1} s^{-1}. The permeability data also show strong temperature dependence reflecting the temperature dependence of solubility.

The diffusivity, solubility, and permeability data from the block degassing experiments were fit to an Arrhenius expression of the form:

$$\boldsymbol{k = A * e^{\frac{-E_a}{RT}}} \tag{2.4}$$

where k is the constant of interest, A and E_a are the A-factor and energy of activation. The Arrhenius fits and parameters are shown in Figure 2.4 and Table 2.3.

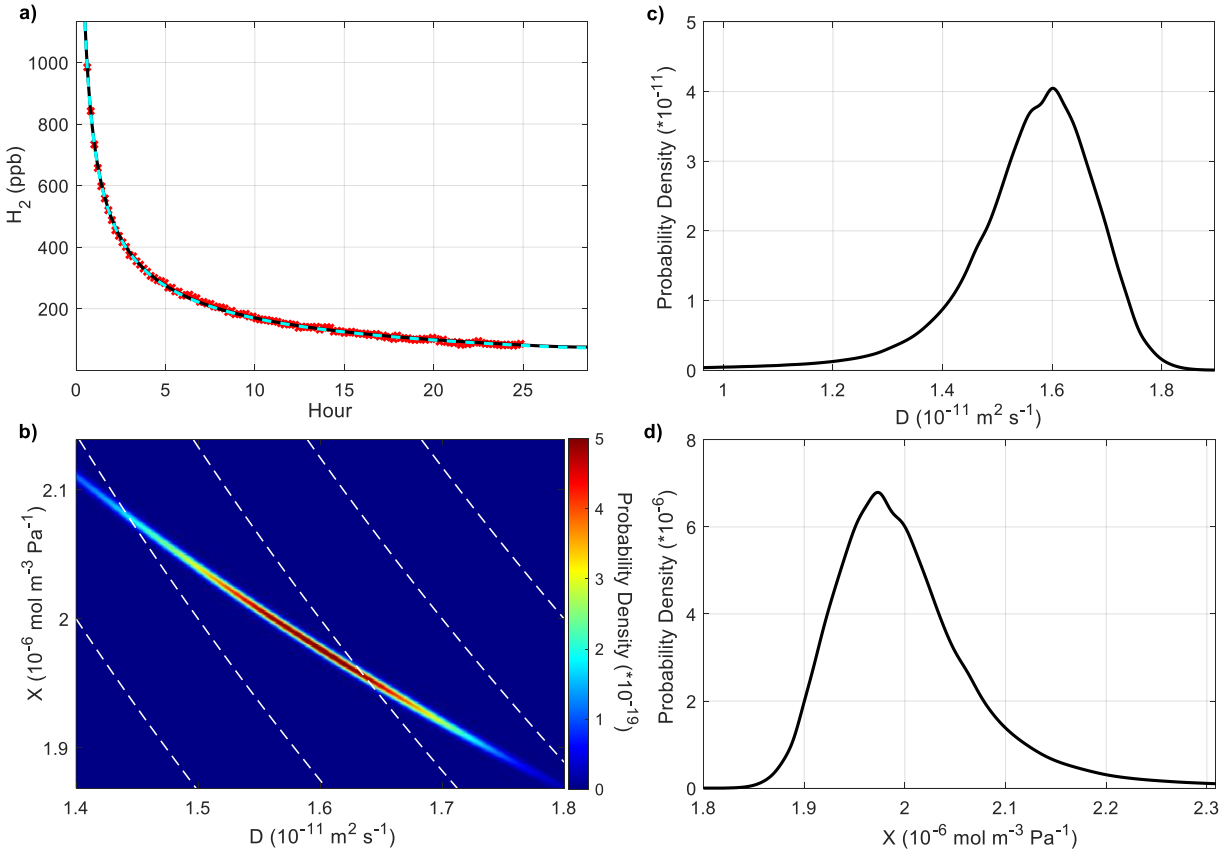

Figure 2.3- a) results from an experiment with Block A at 253 K with a charging time of 70.7 hours. Red x's are measured H_2 mixing ratios. The dashed blue line is the expected mixing ratio from the numerical diffusion model using the optimal diffusivity and solubility constants (Table 2, row 1), and the black line is the expected mixing ratio using the Arrhenius fits in Table 3. The two lines are nearly identical. b) two dimensional probability distribution for diffusivity (D) and solubility (X) calculated for the same experiment. Dashed white lines are contours of constant permeability. c) and d) marginalized 1-dimensional probability distribution for D and X, respectively. The roughness of the marginalized probability distributions is non-physical and results from discretization. Note: the grid spacing used in b),c), and d) is $1.0*10^{-3}$ for both diffusivity and solubility.

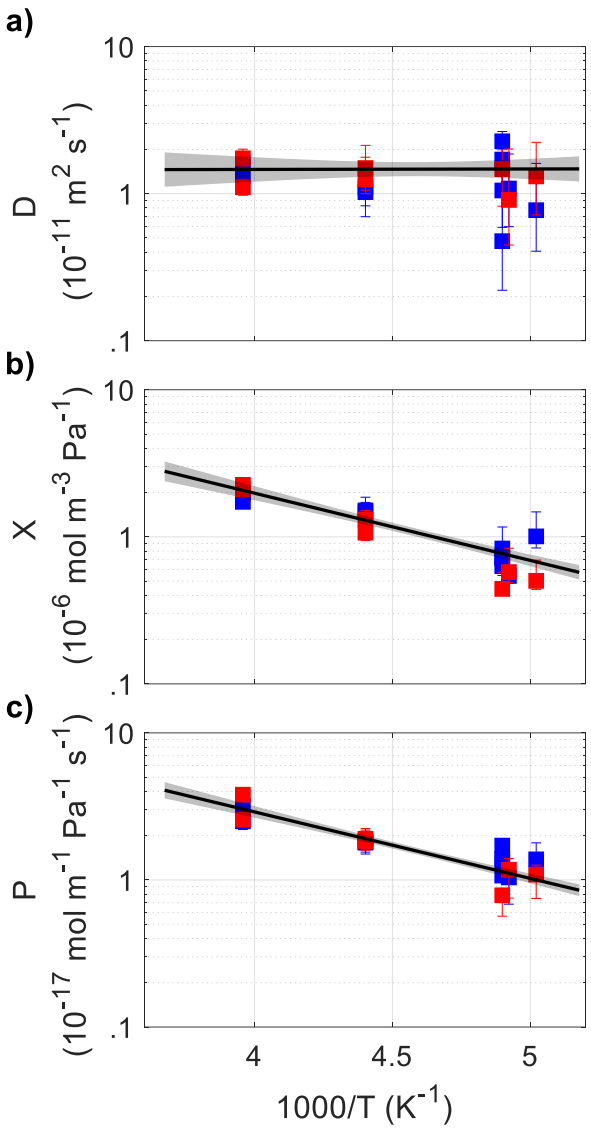

Figure 2.4-Optimized diffusivity (D), solubility (X), and permeability (P) constants obtained from the experiments. Error bars are ±1σ uncertainties. Blue squares correspond to ice Block A, and red squares correspond to Block B. Black lines are the Arrhenius fits with ±1σ uncertainty (Table 2.3)

Table 2.2- Summary of experimental results for H_2 diffusivity, solubility, and permeability derived from the individual block degassing experiments. Uncertainties are given as ±1σ.

Ice Block	Temperature (K)	Diffusivity (10^{-12} m^2 s^{-1})	Solubility (10^{-7} mol m^{-3} Pa^{-1})	Permeability (10^{-18} mol m^{-1} s^{-1} Pa^{-1})
A	252.7	$16.1^{+.7}_{-1.2}$	$19.6^{+.8}_{-.4}$	$31.8^{+.8}_{-1.3}$
	252.7	$13.2^{+3.4}_{-2.6}$	$17.3^{+2.6}_{-1.3}$	$25.1^{+2.8}_{-3.0}$
	227.2	$11.0^{+3.3}_{-2.8}$	$14.6^{+2.5}_{-1.4}$	$17.9^{+2.2}_{-2.4}$
	227.2	$10.2^{+4.3}_{-3.3}$	$15.1^{+3.5}_{-1.9}$	$18.2^{+3.2}_{-3.2}$
	204.2	$4.8^{+8.9}_{-2.5}$	$6.3^{+2.6}_{-.9}$	$10.7^{+1.0}_{-.3}$
	204.2	$22.7^{+3.7}_{-4.4}$	$7.2^{+1.0}_{-.5}$	$17.1^{+1.4}_{-1.7}$
	204.2	$17.1^{+4.9}_{-6.0}$	$7.4^{+1.6}_{-.7}$	$13.9^{+1.7}_{-2.4}$
	204.1	$10.5^{+8.2}_{-4.6}$	$8.3^{+3.3}_{-1.3}$	$13.2^{+3.0}_{-3.5}$
	203.2	$10.8^{+7.8}_{-4.9}$	$5.4^{+1.9}_{-.6}$	$10.4^{+1.2}_{-3.6}$
	199.2	$7.7^{+8.3}_{-3.7}$	$10.1^{+4.7}_{-1.7}$	$13.8^{+4.1}_{-3.5}$
B	252.7	$17.4^{+2.7}_{-2.2}$	$21.1^{+1.6}_{-1.4}$	$38.0^{+3.0}_{-2.6}$
	252.7	$11.1^{+1.5}_{-1.3}$	$22.6^{+1.7}_{-1.1}$	$25.7^{+1.6}_{-1.7}$
	227.2	$14.9^{+6.4}_{-4.4}$	$10.7^{+2.4}_{-1.3}$	$19.0^{+3.4}_{-3.1}$
	227.2	$12.6^{+5.1}_{-2.6}$	$13.1^{+2.0}_{-1.8}$	$18.4^{+3.4}_{-2.1}$
	204.2	$14.7^{+5.2}_{-6.5}$	$4.4^{+1.3}_{-.4}$	$7.9^{+.9}_{-2.2}$
	203.2	$9.0^{+11.1}_{-4.6}$	$5.8^{+2.6}_{-.9}$	$11.7^{+2.2}_{-4.2}$
	199.2	$13.1^{+9.2}_{-5.9}$	$5.0^{+1.9}_{-.6}$	$10.8^{+1.7}_{-3.4}$

Table 2.3- Parameter estimates for the Arrhenius fits (A factor and energy of activation, E_a) to the diffusivity, permeability, and solubility of H_2. Uncertainties are ±1σ. The parameters were obtained using linear regression on the data in Figure 3.2.

Parameter	A factor	E_a (J/mol)
Diffusivity (D)	$\mathbf{1.4^{+1.5}_{-.7}}$*$10^{-11}$ m^2 s^{-1}	$\mathbf{-58^{+1450}_{-1450}}$
Solubility (X)	$\mathbf{1.3^{+.6}_{-.4}}$*10^{-4} mol m^{-3} Pa^{-1}	$\mathbf{8750^{+750}_{-730}}$
Permeability (P)	$\mathbf{1.9^{+1.1}_{-.6}}$*$10^{-15}$ mol m^{-1} Pa^{-1} s^{-1}	$\mathbf{8660^{+840}_{-820}}$

2.5 Comparison to previous work

2.5.1 Diffusivity

To our knowledge, the only previous measurement of H_2 diffusivity in ice is Strauss et al. (1994) who inferred H_2 diffusivity in ice Ih from the energy distribution of scattered neutrons. They reported diffusion coefficients in the range of 10^{-9}-10^{-8} m^2 s^{-1} at temperatures between 25 and 60 K. Those results are two orders of magnitude larger than the results from the current study and comparable to the diffusivity of H_2 in liquid water (3-5*10^{-9} m^2 s^{-1} ; Verhallen et al., 1984). Strauss et al. (1994) noted that these diffusivities were unexpectedly large and an order of magnitude larger than those of H atoms in the same study. The anomalously high diffusivity obtained from these neutron scattering experiments remains unexplained.

Diffusivities have been published for some other small gases of atmospheric interest. Satoh et al. (1996) reported diffusion coefficients for He, Ne, and Ar using techniques similar to those used here. They report D_{He} and D_{Ne} values from 258 - 268 K that are greater than D_{H2} found in this study by factors of approximately 100 and 10, respectively (Figure 2.5a). Their D_{Ar} is slightly lower than D_{H2} by a factor of 2-3. Ikeda-Fukazawa et al. (2002, 2005) estimated D_{He}, D_{O2}, and D_{N2} based on molecular dynamics simulations. Our estimate of D_{H2} is substantially

lower than their estimate for D_{He} at all temperatures. Their estimate for D_{O2} is similar to our result for D_{H2} at our lowest temperatures, but with a much stronger temperature dependence. At the high end of our temperatures (253 K), their D_{O2} is roughly a factor of 5 greater than D_{H2}. For N_2, diffusivity is lower than D_{H2} at low temperatures, and comparable to D_{H2} at the higher end.

2.5.2 Solubility

Ildaykov & Manakov (2014) reported the solubility of H_2 near the melting point (271-272 K) at pressures from 1.9-8 MPa. A linear fit through their data forced through the origin yields an H_2 solubility of $4.6 * 10^{-6}$ mol m^{-3} Pa^{-1}, in reasonable agreement with this study (Figure 2.5b). Extrapolation of the Arrhenius fit to our data predicts a solubility of $2.8^{+.5}_{-.4} * 10^{-6}$ mol m^{-3} Pa^{-1} at 272 K (Table 2.4). Two additional studies of H_2 solubility in ice reported data at pressures exceeding 40 MPa. We did not compare those high-pressure measurements to our data because of the large extrapolation required.

The solubility of H_2 in ice is similar to that of He and substantially larger than those of Ne, O_2, and N_2. In terms of kinetic diameter (KD), He is smaller than H_2. O_2, Ar, and N_2 are larger. Ne is very similar in size to H_2. However, the diffusivity of H_2 is closer to that of O_2 than Ne and the solubility of H_2 is closer to that of He then Ne. KD is clearly not the only factor controlling these physical properties and intermolecular forces must also be important.

The strong temperature dependence of H_2 solubility in ice is similar to the temperature dependence for the solubility of O_2 and N_2 predicted by the molecular dynamics simulations of Ikeda-Fukazawa et al. (2005). Interestingly, Ildyakov et al. (2013) reported a temperature dependence of the opposite sign for the solubility of He in ice. Investigating and explaining these inconsistencies will require further laboratory observations of the behavior of H_2 and other gases in ice.

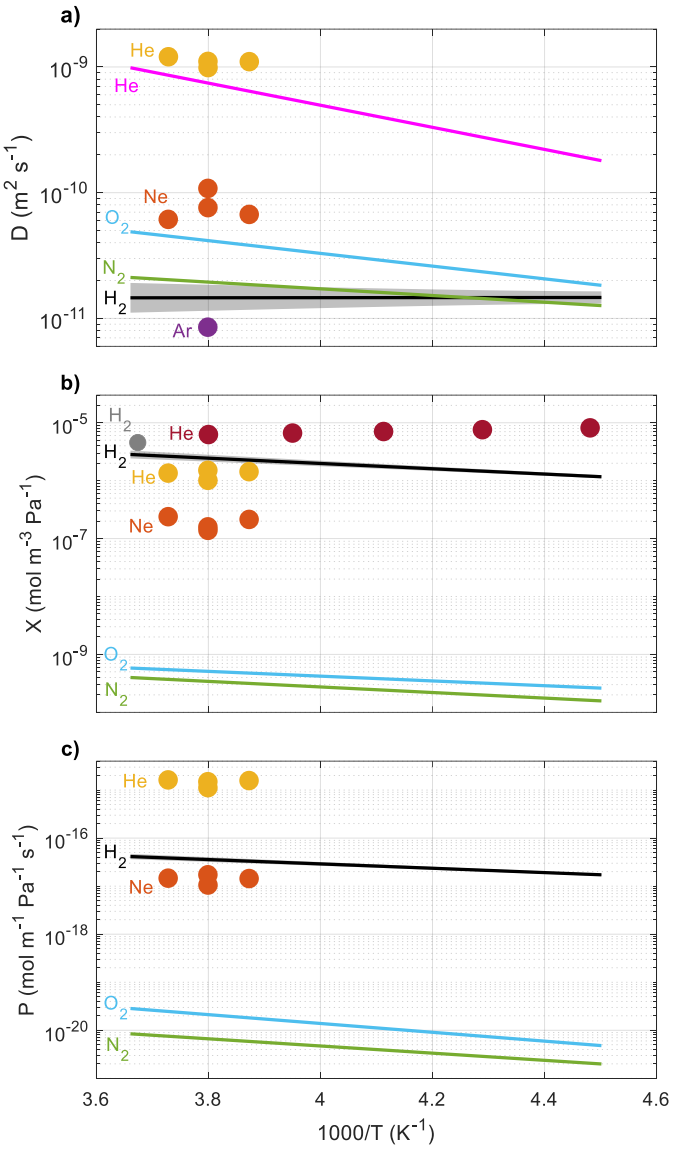

Figure 2.5- Comparison of diffusivity (a), solubility (b), and permeability (c) data from this study with literature data for H_2 and other gases. The plotted data is tabulated in Table 4. Filled circles: gray - measured H_2 solubility (Ildyakov & Manakov, 2014); yellow - measured diffusivity, solubility and permeation of He (Satoh et al., 1996); orange - measured diffusivity, solubility and permeation of Ne (Satoh et al. 1996); purple - measured Ar diffusivity (Satoh et al., 1996); maroon - measured solubility of He (Ildyakov et al., 2013).
Lines: black - Arrhenius fits to data from this study with ±1σ uncertainty (as in Figure 4); magenta - estimated diffusivity of He from molecular dynamics simulations (Ikeda-Fukazawa et al., 2002); blue and green lines-estimated diffusivity, solubility, and permeability of O_2 and N_2 from molecular dynamics simulations (Ikeda-Fukazawa et al., 2005).

Table 2.4- Summary of the diffusivity, solubility, and permeability data from various literature sources that is plotted in Figure 2.5

Gas	Reference	Temp. K	Diffusivity D (m^2 s^{-1})	Solubility X (mol m^{-3} Pa^{-1})	Permeability P (mol m^{-1} Pa^{-1} s^{-1})
Discrete measurements:					
H_2	Ildyakov & Manakov, 2014	272	N/A	$4.6*10^{-6}$	N/A
He	Ildyakov et al., 2013	223	N/A	$8.2*10^{-6}$	N/A
		233	N/A	$7.6*10^{-6}$	N/A
		243	N/A	$7.1*10^{-6}$	N/A
		253	N/A	$6.6*10^{-6}$	N/A
		263	N/A	$6.3*10^{-6}$	N/A
He	Satoh et al., 1996	258	$1.1*10^{-9}$	$1.4*10^{-6}$	$1.6*10^{-15}$
		263	$1.1*10^{-9}$	$1.0*10^{-6}$	$1.1*10^{-15}$
		263	$9.9*10^{-10}$	$1.5*10^{-6}$	$1.5*10^{-15}$
		268	$1.2*10^{-9}$	$1.4*10^{-6}$	$1.6*10^{-15}$
Ne	Satoh et al., 1996	258	$6.7*10^{-11}$	$2.1*10^{-7}$	$1.4*10^{-17}$
		263	$7.6*10^{-11}$	$1.4*10^{-7}$	$1.1*10^{-17}$
		263	$1.1*10^{-10}$	$1.6*10^{-7}$	$1.7*10^{-17}$
		268	$6.1*10^{-11}$	$2.4*10^{-7}$	$1.5*10^{-17}$
Ar	Satoh et al., 1996	263	$8.5*10^{-12}$	N/A	N/A

Arrhenius relationships:		Diffusivity		Solubility		Permeability	
		A (m^2 s^{-1})	E_a (J mol^{-1})	A (mol m^{-3} Pa^{-1})	E_a (J mol^{-1})	A (mol m^{-1} Pa^{-1} s^{-1})	E_a (J mol^{-1})
H_2	This Work	$1.4*10^{-11}$	-58	$1.3*10^{-4}$	8750	$1.9*10^{-15}$	8660
He	Ikeda-Fukazawa et al., 2002	$1.6*10^{-6}$	16830	N/A	N/A	N/A	N/A
O_2	Ikeda-Fukazawa et al., 2004	$3.5*10^{-9}$	9700	$1.9*10^{-8}$	7900	$6.6*10^{-17}$	17600
N_2	Ikeda-Fukazawa et al., 2004	$2.0*10^{-10}$	5100	$2.3*10^{-8}$	9200	$4.6*10^{-18}$	14400

2.6 Implications for the mobility of H_2 in polar firn and ice

The permeability rates determined in this study can be used to examine how mobility of H_2 influences the incorporation of atmospheric H_2 levels into the polar ice sheets and the behavior of H_2 in ice cores during recovery and storage.

2.6.1 Pore close-off fractionation

Dissolution and diffusion of H_2 through the ice lattice can affect the composition of firn air and ice core bubbles. Pore close-off fractionation refers to the gradual pressurization of closed bubbles which drives a diffusive flux of gases between bubbles and open pores (Huber et al., 2006; Ikeda-Fukazawa et al., 2005; Severinghaus & Battle, 2006). Significant enrichment of small, diffusive gases has been measured in the open pores at the base of the firn air lock-in zone where vertical gas phase diffusion within the open porosity is inhibited by impermeable winter layers. These impermeable layers allow much steeper concentration gradients to exist in the open porosity in the lock-in zone. Severinghaus & Battle (2006) reported that firn air samples from the base of the lock-in zone were enriched in ^{22}Ne by as much as 10%. Pore close-off fractionation begins well above the lock-in zone, leading to upward diffusion of the fractionated gas. As a result, ice core bubbles must be depleted in mobile gases such as Ne, relative to the overlying atmosphere.

Pore close-off fractionation must be accounted for when reconstructing past atmospheric levels of H_2 from firn air measurements using firn air models. At South Pole, neglecting this process leads to an overestimate of atmospheric levels of H_2 by ~10% during the early 1900's (Patterson et al. 2020). Pore close-off fractionation in firn air models has been parameterized in numerous ways. In Severinghaus & Battle (2006), small gases like Ne and H_2 diffuse through the thin walls of recently closed bubbles into the open porosity. The bubbles contribute to the

fractionation until they have been compressed by 5% by firn densification. Beyond that point, bubbles cease to contribute to fractionation because they are assumed to be too far from open porosity. Patterson et al. (2020) refer to this model as the "kinetic model" because it implicitly assumes that diffusion through the ice lattice is a rate-limiting process. Alternatively, Patterson et al. (2020) proposed an "equilibrium model" of pore close-off fractionation in which H_2 diffusion through ice is sufficiently fast to equilibrate the partial pressure of H_2 between closed bubbles and open pores at the South Pole. Here we use the laboratory data from this study and a simple numerical diffusion model to examine the validity of the assumption of equilibrium.

The numerical model simulates radial diffusion from a single spherical, pressurized bubble through a concentric shell of ice into an outer shell of "open porosity" (Figure 3.4, inset). The closed bubble is assumed to have a volume of 10^{-10} m^3, corresponding to a radius of 0.288 mm. Equilibration time is calculated as a function of depth at the South Pole for depths where closed bubbles make up >1% of the total volume, beginning at a depth of 108 m. The porosity profile from the firn air model of Patterson et al. (2020) was used to prescribe the ice shell thickness and the volume of the "open porosity" shell. For each model run, the ratio of the volumes of the open porosity and closed bubble to total ice volume is identical to those ratios at the corresponding depth in the firn air model. The ice shell thickness decreases with depth from 1 mm at 108 m to 0.4 mm at 125 m because, in the firn air model, the ratio of ice volume to closed bubble volume decreases with depth. Likewise, open porosity volume decreases with depth from $1.0*10^{-9}$ m^3 at 108 m to $2.2*10^{-13}$ m^3 at 125 m because the ratio of open porosity volume to closed bubble volume in the firn air model decreases with depth. The model is initialized with H_2- free ice and equilibrium between the gas and ice is assumed at the boundaries of the bubble and the shell throughout the model run. The model calculation is carried out in one

dimension, and non-radial diffusion is ignored. The diffusivity and solubility constants at the annual average temperature at South Pole (223 K) were calculated from the Arrhenius fits to the data from this study. The characteristic relaxation time (*e*-folding time) for equilibration is calculated and plotted in Figure 3.4. The characteristic relaxation time (τ) is defined as the time at which:

$$\frac{P_{eq}}{P_{eq}-P_o(\tau)} = exp\ (1) \tag{2.5}$$

Where P_{eq} is the equilibrium partial pressure of H_2 in the open porosity shell and P_o is the time-varying partial pressure of H_2 in the open porosity shell.

The *e*-folding time for the equilibration of the partial pressure of H_2 in the outer shell ranges from 7.0 days at 108 m to 0.1 day at 125 m. The rapid decrease in equilibration time with depth is driven by the decreasing ice shell thickness and by decreasing open pore volume. At South Pole, the annual accumulation rate is about 8 cm ice eq. y^{-1} and bubble pressurization in the firn column is roughly ~.1% yr^{-1}. This model result suggests that the assumption of diffusive equilibrium between closed and open porosity is reasonable at the South Pole, and, given the short *e*-folding time, it is likely that the assumption of equilibrium is valid even at higher accumulation sites where bubble pressurization is more rapid. The geometry assumed in this calculation is highly oversimplified. In reality, the open pores are a complex web-like network, making it challenging to determine the average distance between closed bubbles and open pores (Burr et al., 2018; Figure 2.7). Images obtained from X-ray tomography of firn (Figure 2.7)

could be used to develop more refined calculations of equilibration times for pore close-off fractionation.

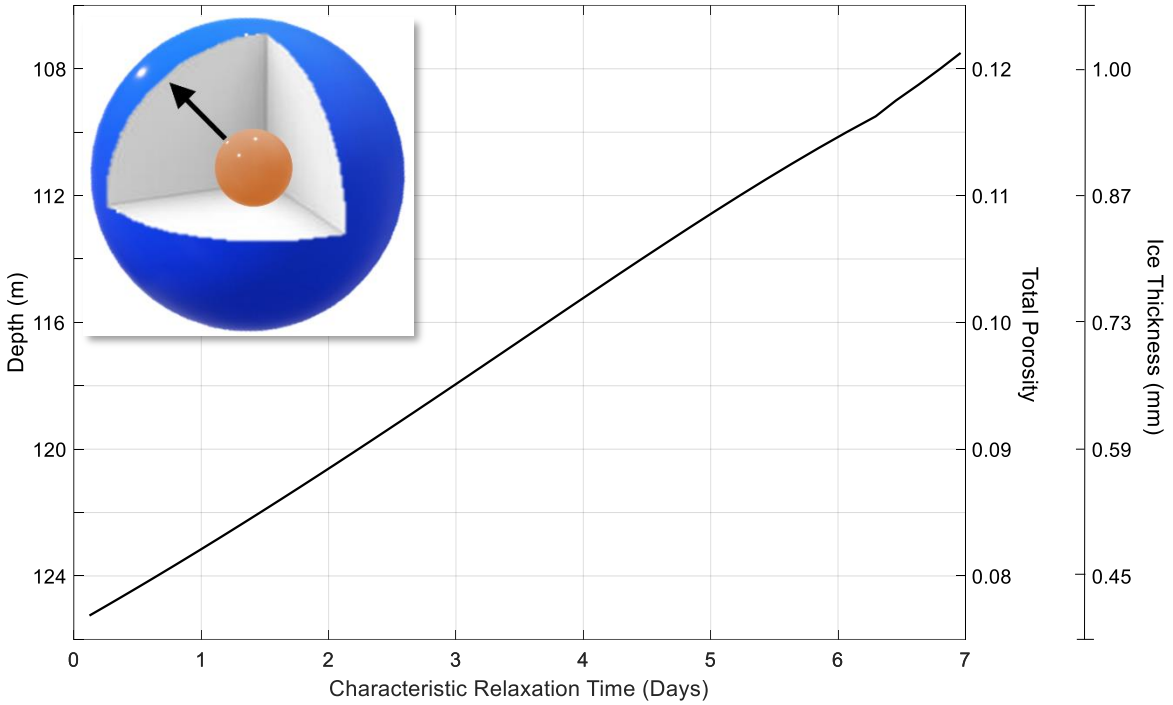

Figure 2.6- Results from a model simulation of H_2 diffusion between a pressurized bubble and unpressurized open pores showing characteristic relaxation time as a function of firn depth. Characteristic relaxation time is defined as the *e*-folding time for the equilibration of the partial pressure of H_2 in the outer shell of open porosity. Inset: An illustration of the geometry of the simulation. The bubble is at the center of an ice sphere with an outer "shell" of open porosity. H_2 diffuses from the inner bubble (orange) through the ice (white) to the outer "open porosity" (blue). Graph: corresponding total porosity (i.e. (open pore volume +closed bubble volume/ firn volume) and model ice shell thickness for each depth is shown on the right y-axis.

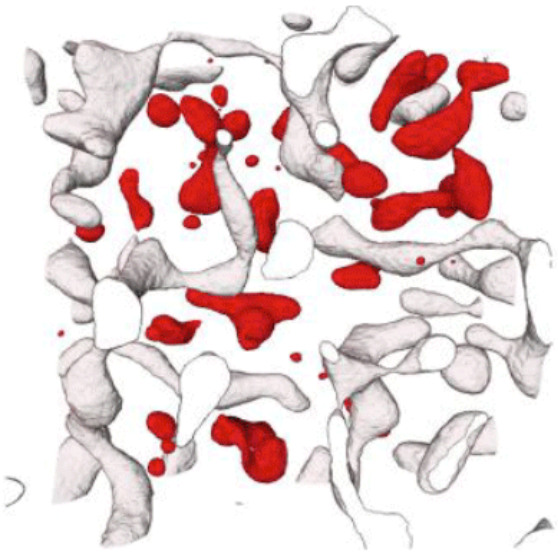

Figure 2.7- X-ray tomography image of the porosity field from just below the close-off depth (100 m) at Dome C. Below 100 m, firn air could not be sampled. Open pores are white and closed bubbles are red. The cross section is 6.72 mm x 6.72 mm. Reproduced with permission from Burr et al. (2018).

2.6.2 Diffusive migration of H_2 in an ice sheet

The internal pressure of air bubbles increases with depth below the firn/ice transition in response to the increasing hydrostatic pressure. The resulting increase in partial pressure of H_2 causes dissolution of H_2 from the bubble into the ice. This creates a vertical concentration gradient of H_2 in the ice and a net upward flux of H_2 in the ice sheet even in the case of constant atmospheric H_2 levels. The increase in H_2 partial pressure with depth likely continues until the bubble/clathrate transition is complete and no H_2 is present in the gas phase. This phenomenon has been observed previously with He (Craig & Chou, 1982; Jean-Baptiste et al., 1993, 2001)

To investigate the magnitude of this effect for H_2, we use a 1-dimensional finite difference advective/diffusive ice sheet model with layer thinning and ice densification (Neftel et al., 1983). The ice sheet model is discretized into annual layers. To isolate the effects of diffusion in the ice sheet from those associated with the firn layer (discussed in section 2.6.1 above), the

ice sheet model is not coupled to a firn air model. H_2 is assumed to be in equilibrium between ice and bubbles in each layer. The physical properties of South Pole were used for this calculation and a constant atmospheric mixing ratio was maintained. The model was run for 20,000 years and a steady state profile was achieved. The resulting vertical gradient was small (~1% m^{-1}). Upward diffusion was negligible, approximately 0.001% loss of H_2 from a single annual layer over 5,000 years. This result is consistent with the results of Jean-Baptiste et al. (1993), given that the permeability of H_2 is less than 0.01 times that of He.

We also investigated the diffusive smoothing of vertical gradients of H_2 in the ice sheet originating from fluctuations in atmospheric H_2 using the same model (Neftel et al., 1983). A 1-year pulse of H_2 is introduced at the surface and the model is run for 10,000 years. The amplitude of the resulting peak decreases, and the peak broadens due to vertical diffusion as it propagates through the ice sheet (Figure 2.8). The full width at half maximum (FWHM) for the 1-year pulse after propagating for 1000 years is 0.6 m, which is equivalent to 10 years. After 10,000 years, the pulse FWHM is 4.5 m, equivalent to 78 years.

Sites with higher annual accumulation experience a reduction in smoothing due to thicker annual layers. However, the effects of thicker layers are somewhat offset by the more rapid permeation associated with warmer temperatures. For example, under WAIS-Divide conditions (243 K, 22 cm ice eq. y^{-1}), the FWHM for a 1-year pulse is 6 years (0.8 m) after 1000 years of propagation and 44 years (6.1 m) after 10000 years of propagation. Annual layers are about 2.8 times thicker at WAIS-Divide than South Pole, but smoothing is only attenuated by a factor of 1.7.

These results indicate that reconstructing high frequency (decadal) atmospheric H_2 variability from polar ice cores will require some correction for diffusive smoothing. This could

be accomplished by inverting an ice sheet model in a similar fashion to firn air reconstructions (eg. Patterson et al., 2020; Petrenko et al., 2013). Smoothing of atmospheric variations also occurs due to gas phase diffusion in the firn column. At the South Pole, the age distribution of the H_2 incorporated into the ice sheet at the bottom of the firn column has a FWHM of ~13 years (Patterson et al., 2020). This smoothing in the firn air column is important to account for with all ice core samples. In contrast, smoothing due to diffusion through the ice lattice is only important for samples that are more than several centuries old.

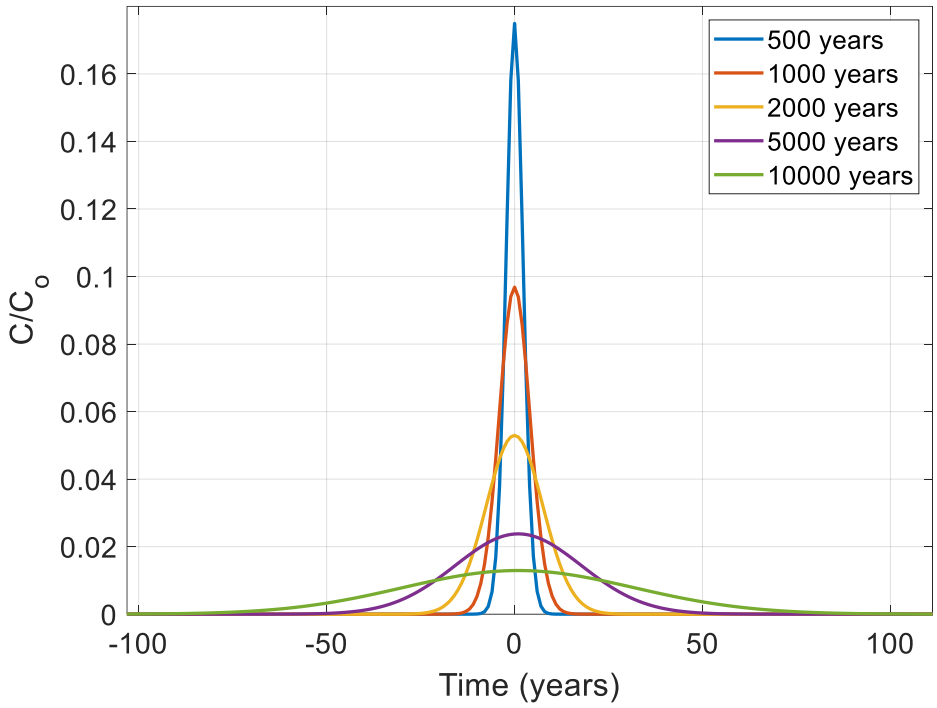

Figure 2.8- Model simulation of a pulse of H_2 propagating through the ice sheet at the South Pole. Length has been converted to time-scale on the x-axis.

2.6.3 Post-coring diffusive exchange with atmospheric H_2

After an ice core has been drilled and brought to the surface, H_2 within the ice equilibrates with the surrounding atmosphere. The rate of this process dictates the procedures required to sample ice cores for analysis of paleoatmospheric H_2 levels. As described earlier, the

hydrostatic compression of bubbles at depth drives H_2 from the bubbles into the ice. This effect causes newly drilled ice to be supersaturated with respect to atmospheric H_2. A similar phenomenon occurs for He, and post-coring diffusive losses for He have been estimated to be as much as 10% within 15 minutes of drilling and recovery (Jean-Baptiste et al., 1993, 2001). Haan (1996) reported measurements of H_2 in several stored ice cores, showing that the measured H_2 levels are roughly consistent with full equilibration with the ambient atmosphere in the storage freezer. However, the kinetics of diffusive exchange cannot be calculated from that data, as the storage time of the cores was not given.

Post-coring equilibration of H_2 was simulated using a finite difference model of diffusion in a uniform cylinder. The model assumes radial symmetry and a homogeneous distribution of bubbles. For this calculation we used the approximate properties of a 10 cm diameter South Pole ice core recovered from a depth of 200 m (223 K, accumulation rate 8 cm ice eq. yr^{-1}). The bubble pressure was estimated from the ice sheet model described in section 2.6.2. The in-situ bubble pressure at 200 m is roughly 25 bar. H_2 in the bubbles at close-off was assumed to be 300 ppb, based on firn air measurements at the base of the lock-in zone at South Pole (Patterson et al., 2020). We make two simplifying assumptions in this calculation that both tend to overestimate the rate of diffusive equilibration. First, instantaneous equilibrium is assumed between the bubbles and the ice within each grid cell. Second, ice relaxation is neglected. Gow (1971) estimated a density change of 0.2-0.3% over 16 months for a GISP2 ice core sample recovered from a depth of 200 m. This implies a 7-10% decrease in bubble pressure over that time span. Therefore, this calculation serves as an upper bound on diffusive losses of H_2 from a bubbly ice core. Diffusion and solubility coefficients were obtained using the Arrhenius parameters in Table 3 for 253 K, a typical storage freezer temperature.

The model simulation is run for one year of sample storage at ambient atmospheric levels of 530 ppb H_2. The results show that over one year, the ice core sample loses only 18% of its H_2 (Figure 2.9). This calculation suggests that bubbly ice core samples could still be meaningfully analyzed for H_2 after storage for several months in the ambient atmosphere provided that the outermost ice is removed before extraction. A caveat to this conclusion is the possible additional loss of H_2 via microfractures associated with drilling and ice relaxation. Small losses of Ar and O_2 (1-2%) have been observed during storage and attributed to microfractures in the ice lattice associated with drilling and extraction (Bender et al., 1995). These losses ceased after 3 months presumably because of microfracture healing. It is possible that microfracture-related losses of H_2 could be greater due to its smaller molecular diameter, but the size dependence of this phenomenon has not been established.

We also considered the case of deep ice core samples in which some or all of the enclosed air is bound in clathrate hydrates. Air bubbles transform into air clathrate inclusions in the ice lattice at depths between 500 m and 1700 m, depending on site temperature and accumulation rate, (Miller, 1969; Salamatin et al., 1998; Shoji & Langway, 1982) . Pure H_2 clathrates do not form in polar ice sheets because the dissociation pressure of such clathrates (~10^9 Pa at 223 K) is substantially higher than *in situ* pressures (Mao & Mao, 2004; Vos et al., 1993). Experimental evidence shows that H_2 can occupy various sites in N_2 clathrates as a guest molecule. Lu et al. (2012) exposed N_2 clathrates to pure H_2 at 150 bar and observed formation of mixed clathrates with between 1 and 3 H_2 molecules per N_2 molecule. Those results are not directly transferable to clathrates in an ice sheet where N_2 is ~10^7 times more abundant than H_2. Instead, we estimated the fractional occupancy of clathrates in polar ice using Kihara potentials after Mousis et al. (2013) and Parrish & Prausnitz (1972). Using this approach, we calculated the

partitioning of H_2 between the dissolved phase, the gas phase, and clathrates (both large and small cage) occupied by a mixture of N_2, O_2, Ar, and H_2. These are thermodynamic calculations that do not account for the kinetics of clathrate nucleation and growth or for the non-hydrostatic behavior of bubbles (Salamatin et al., 1998). This calculation also requires some air to remain in the gas phase (bubbles) at all pressures. In actuality, bubbles are no longer observed below the bubble/clathrate transition depth (e.g., below 1300 m at South Pole; Ackermann et al., 2006). These simplifications notwithstanding, the calculation should estimate the impact of clathrate formation on H_2 mobility in deep polar ice.

Parameters for the calculations include Kihara potential parameters for N_2, O_2, Ar, and H_2 (Mousis et al., 2013; Khan et al., 2015) and Structure II clathrate physical parameters from Mousis et al. (2013). Dissociation pressures for pure clathrates of N_2, O_2, Ar at 223 K were calculated after Mousis et al. (2013). The dissociation pressure of pure H_2 clathrate was estimated from an Arrhenius fit to the data in Mao & Mao (2004).

The following case is an example illustrating how clathrates influence the behavior of H_2 in ice. We use conditions similar to those at the base of the bubble-clathrate transition zone at South Pole: 1) a bubble volume to ice volume ratio of 10^{-6}, 2) a total gas pressure of $7.6*10^9$ Pa if no clathrates were present, 3) total gas composition of 0.78 N_2, 0.21 O_2, 0.01 Ar, and 400 ppb H_2 (including H_2 in both the dissolved and gas phases). The amount of N_2, O_2, and Ar dissolved in the ice lattice is negligible compared to the clathrate and gas phase, and is ignored in these calculations. At equilibrium under these conditions, 99.95% of the total gas present in the system is enclathrated and .05% of the total gas present in the system remains in the gas phase at a pressure of $3.8*10^6$ Pa. 97.0% of the H_2 present in the system is dissolved in the ice lattice, 3.0% partitions into the clathrates, and .04% remains in the gas phase. The small amount of H_2 present

in the clathrate phase reflects the small magnitude of the Kihara potential well of an enclathrated H_2 molecule.

Diffusive losses of H_2 from a bubble-free clathrate ice sample with these characteristics were calculated using the Crank (1975) solution for radial diffusion in a cylinder. To facilitate the calculation, we make two simplifying assumptions: 1) all of the H_2 is dissolved in the ice lattice (rather than the ~97% predicted from the Kihara calculation), and 2) as before, ice relaxation during storage is ignored, although Gow (1971) estimated that the volume of a GISP2 sample recovered from 1000 m increased by .3-.4% over 16 months. The results show that after one year, the bubble free ice has lost 66% of the H_2 initially present in the sample (Figure 3.7). This simulation provides an upper limit on diffusive losses of H_2 from clathrate ice. H_2 concentrations in clathrate ice are much higher than in bubbly ice because H_2 partitions almost exclusively into the dissolved phase in clathrate ice. The greater supersaturation in H_2 relative to the atmosphere causes faster diffusive losses from clathrate ice upon sample recovery. As a result, it is evident that ice core samples containing clathrates intended for analysis of H_2 should be enclosed in an impermeable container after drilling to prevent diffusive exchange with the modern atmosphere.

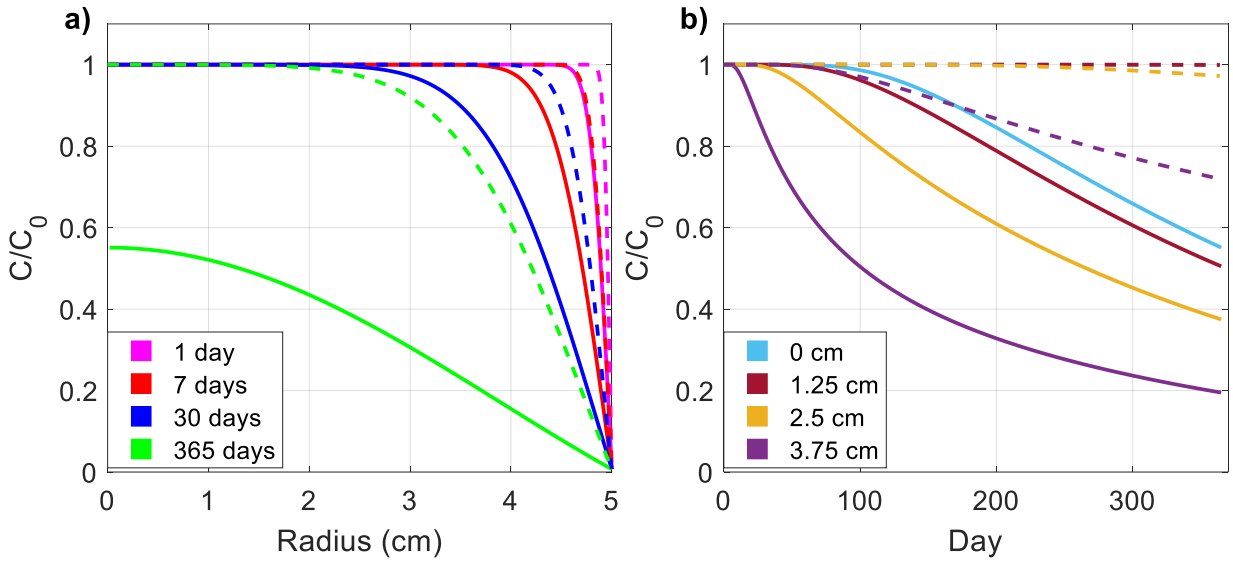

Figure 2.9- Model simulation of equilibration of ice core samples recovered from South Pole from bubbly and bubble-free clathrate ice. The fraction of initial H_2 remaining is plotted as a function of distance from the center of a 10 cm diameter ice core and of storage time after drilling. Dashed lines: bubble-containing (200 m) ice, Solid lines: bubble-free clathrate ice. a) Curves show the profile after 1 day (magenta), 7 days (red), 30 days (blue), and 365 days (green). b) curves show the time course at radii of 0 cm (light blue), 1.25 cm (maroon), 2.5 cm (yellow), and 3.75 cm (purple).

Table 2.5- Comparison of gas partitioning for a system with only bubbles and for a system with bubbles in thermodynamic equilibrium with clathrates

Condition	Pressure	Bubble (mole fraction)				Clathrate (mole fraction)				Ice (mol m^{-3})
	P (Pa)	N_2	O_2	Ar	H_2	N_2	O_2	Ar	H_2	H_2
Bubbles only	$7.6*10^{9}$	0.78	0.21	0.010	$1.8*10^{-10}$	N/A	N/A	N/A	N/A	$1.6*10^{-6}$
Bubbles and clathrates	$3.8*10^{6}$	0.90	0.098	$2.3*10^{-3}$	$3.5*10^{-7}$	0.78	0.21	0.01	$1.2*10^{-8}$	$1.6*10^{-6}$

2.7 Summary and conclusions

The permeability of H_2 in ice was experimentally measured at temperatures relevant to polar ice and partitioned into diffusivity and solubility constants. H_2 permeability in ice exhibits positive temperature-dependence. The temperature dependence of permeation appears to be fully explained by that of solubility while diffusivity appears to be temperature invariant. This is a surprising result because conceptual models for diffusion of gases in ice typically invoke an activation energy associated with the mobility of vacancies in the lattice or potential fields between the ice and diffusing gas molecules (Ikeda-Fukazawa et al., 2002, 2004, 2005). There is little experimental data in the literature with which to validate this finding. Satoh et al. (1996) reported temperature-independent diffusivity of Ne in ice, but that study covered only a 10 K temperature range. If temperature independence of diffusivity proves correct, it would suggest that the mechanism of diffusion is more complex than previously assumed. Further experimental work on the diffusion of small gases in ice is warranted and the experimental methodology developed here is easily extended to other gases.

The permeability of H_2 allows estimation of the rates of processes relevant to reconstructing the atmospheric history of H_2 from polar firn air and ice cores. H_2 permeation is likely to result in equilibration between open and closed pores in the firn column. Such equilibration simplifies firn air modeling for H_2 (Patterson et al., 2020). H_2 permeation in polar ice leads to diffusive smoothing of vertical gradients.

For ice with gas ages of several centuries, this smoothing is comparable to that caused by diffusion during firn air enclosure. Finally, we estimate the rate of exchange of ice core samples with the atmosphere and find that the permeation of H_2 from bubbly ice should be slow enough to permit analysis of H_2 up to a year after drilling (barring additional losses via microfractures).

CHAPTER 3

Reconstructing atmospheric H_2 from polar firn air

Includes excerpts from:

Patterson J. D., Aydin, M., Crotwell, A.M., Petron G., Severinghaus J. P., & Saltzman, E. S. (2020). Atmospheric history of H_2 over the past century reconstructed from South Pole firn air. *Geophysical Research Letters*, *47*, e2020GL087787. https://doi.org/10.1029/2020GL087787

Patterson, J. D., Aydin, M., Crotwell, A. M., Pétron, G., & Severinghaus, J. P. (2021). H_2 in Antarctic firn air: Atmospheric reconstructions and implications for anthropogenic emissions. Proceedings of the National Academy of Sciences of the United States of America, 118. https://doi.org/10.1073/pnas.2103335118/-/DCSupplemental.90

3.1 Overview

This chapter presents reconstructions of the atmospheric history of H_2 from firn air measurements. During the course of this research, it was discovered that H_2 had been measured in polar firn air from several sites between 1996 and 2013 but the data was never analyzed or published. Here we report firn air measurements of H_2 from two sites in Antarctica and three in Greenland. The challenges associated with calibrating those measurements are discussed. New firn air modeling techniques specific to highly diffusive gases such as H_2 are presented, and the details of the atmospheric reconstruction technique are described. Reconstructions of southern hemisphere H_2 levels since 1850 and northern hemisphere H_2 levels since 1930 are presented (Patterson et al., 2020; 2021). These are the first reconstructions of atmospheric H_2 spanning the 20^{th} century.

3.2 Introduction

The utilization of H_2 as an energy source emits no carbon to the atmosphere if produced from renewables. Increasing adoption of H_2 as a substitute for fossil fuels is likely (van Renssen, 2020). As the H_2 energy sector expands, anthropogenic emissions are expected to increase due to leakage (Paulot et al., 2021; Prather, 2003; Wang et al., 2013a). Projecting the effects of increasing anthropogenic emissions requires a comprehensive understanding of the biogeochemical cycle of H_2. Reconstructing the paleoatmospheric levels of H_2 contributes to that understanding by establishing the baseline for quantifying anthropogenic emissions since the industrial revolution and for studying the effect of climate variability on the cycling of atmospheric H_2 over decadal to century time scales.

Prior to this study, there was one published firn air study of the historical trends of atmospheric H_2. Petrenko et al. (Petrenko et al., 2013) reconstructed northern hemisphere H_2 from Greenland firn air measurements. Their results show an increase in atmospheric H_2 levels from 400-480 ppb during the 1960's to a peak of 500-520 ppb during the early 1990's, then, a recent decline to about 480 ppb in 2010. The peak and recent decline are inconsistent with modern flask measurements that show a slow increase during the 1990's. (Novelli, 2006; Novelli et al., 1999; Prinn et al., 2019). The authors note that the firn air model used for the reconstruction does not include pore close-off fractionation of H_2, and suggest that it is possible that the inferred peak is an artifact of this process (Petrenko et al., 2013; Severinghaus & Battle, 2006).

3.3 Firn air sites, sampling and H_2 measurements

3.3.1 Firn air sites

H_2 measurements from five firn air sampling campaigns were used in this research. The sites of the five campaigns were: South Pole, Antarctica; Megadunes, Antarctica; North Greenland Eemian Ice Drilling Site (NEEM), Greenland; Summit, Greenland; and Tunu, Greenland. Site characteristics and associated references are summarized in Table 3.2. Sites were chosen because of the availability of high-quality H_2 measurements that had not previously been analyzed. Inclusion of sites from both hemispheres allows for analysis of changes to the inter-hemispheric difference and the global biogeochemical cycle of H_2.

Table 3.1- Site characteristics and associated references for each of the five firn air sampling campaigns used in this research are summarized below.

Site	Lat.	Lon.	Sampling Date	Average Temp. (°C)	Average Acc. (cm i.e. y^{-1})[1]	Sampling Ref.	Modeling Parameters Ref.[2]
South Pole	90°S	25°W	1/2001	-51	8.1	Severinghaus & Battle, 2006	Severinghaus & Battle, 2006
Megadunes	81°S	125°E	1/2004	-49	2.8	Severinghaus et al., 2010	Severinghaus et al., 2010
NEEM	77°N	51°W	7/2008	-29	21.6	Petrenko et al., 2013	Buizert et al., 2012
Summit	73°N	38°W	5/2013	-31	23.4	Hmiel et al., 2020	Christo Buizert, Personal Communication
Tunu	78° N	34° W	5/1996	-29	10.0	Butler et al., 1999	This Work

[1]Average Accumulation (cm ice equivalent per year)
[2]Modeling parameters include: density profile, diffusivity profile, partitioning between open and closed porosity, and the depth of the onset of the lock-in zone (Section 2.4.1).

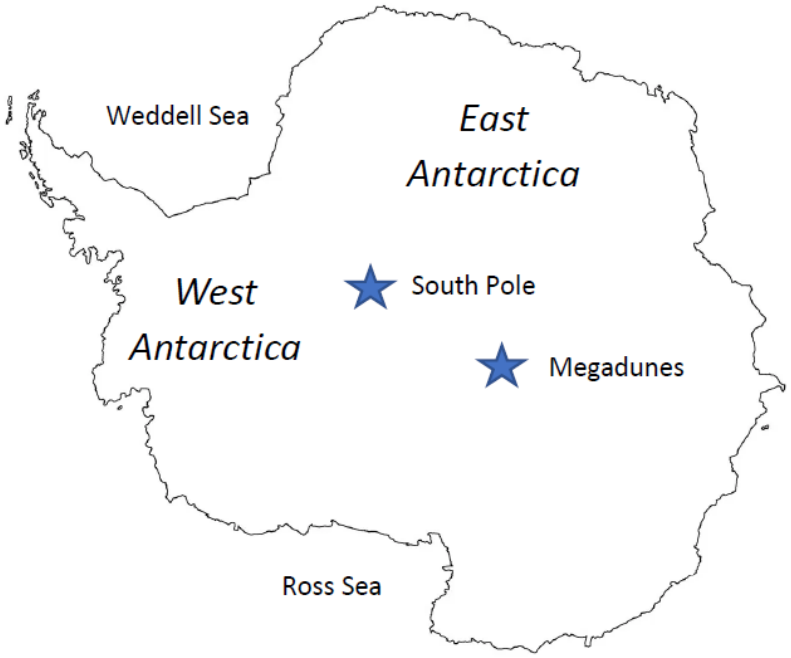

Figure 3.1- Locations of the South Pole and Megadunes firn air sampling sites in Antarctica

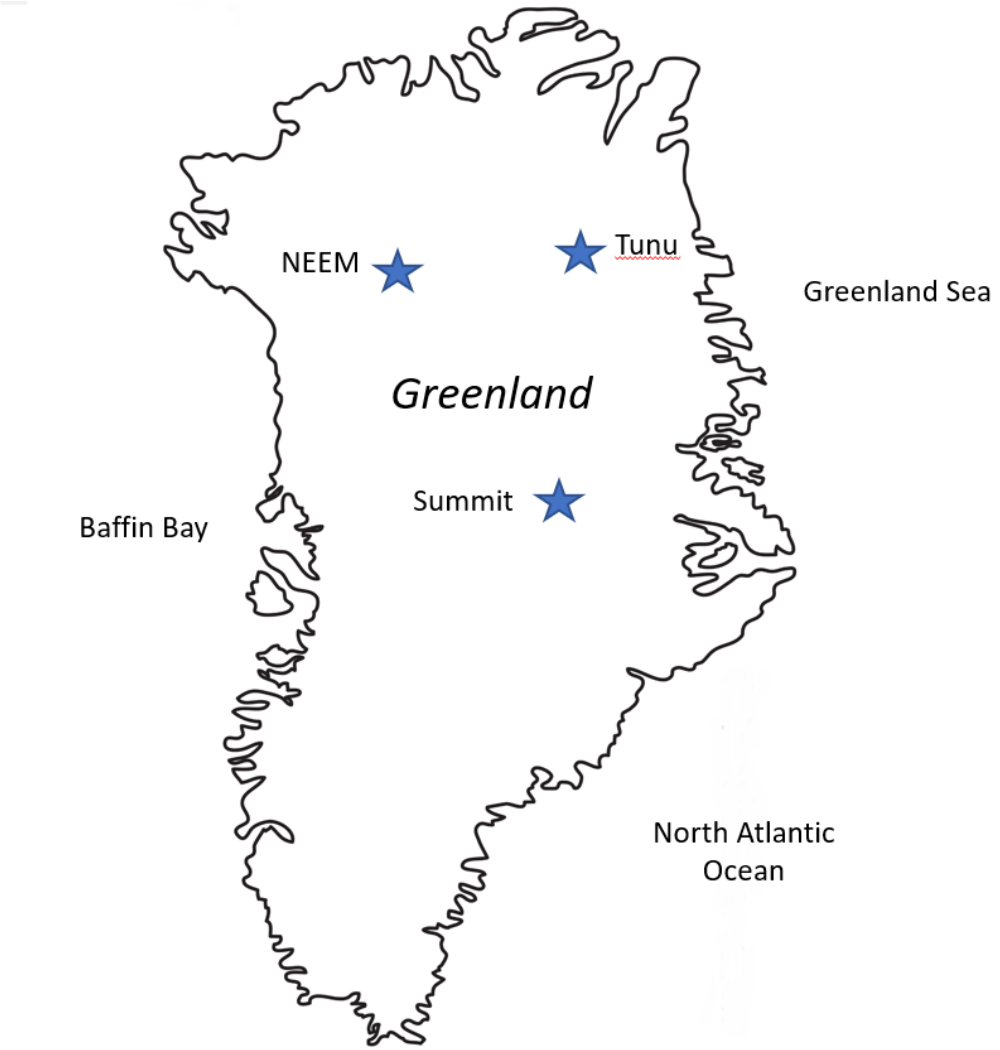

Figure 3.2- Locations of the NEEM, Summit, and Tunu firn air sampling sites in Greenland

3.3.2 Firn air sampling

The sampling methods used in these firn air campaigns were similar to techniques from previous published firn air studies (Figure 3.3; eg. M. Battle et al., 1996; Severinghaus et al., 2001; Severinghaus & Battle, 2006). A borehole was drilled into the snowpack. The hole was sealed above each sampling depth with an inflatable rubber packer to prevent contamination from the modern atmosphere. Decabon tubes for both waste air and sample air extend from below the packer to the surface. The waste air intake was positioned directly below the rubber packer. The waste air intake was separated from the sample air intake by stainless steel baffle nearly as wide as the borehole. Air was pumped from the waste air intake 2-5x faster than from the sample air intake to ensure that no air that had been in contact with the rubber packer was sampled. Sampled air was pumped across a P_2O_5 desiccant and stored in 2 l glass flasks. More detailed information regarding the sampling at each site may be found in the references listed in Table 3.1.

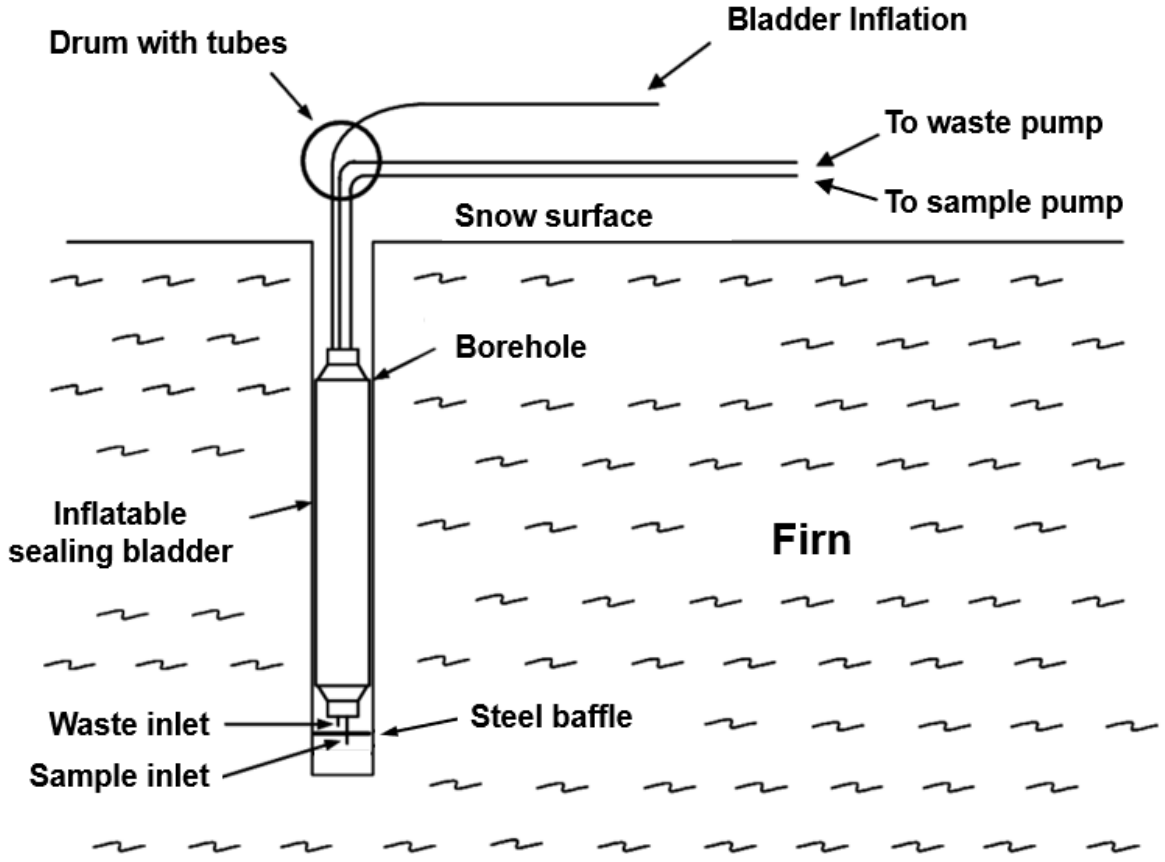

Figure 3.3- Schematic of a typical firn air sampling apparatus, adapted from Assonov et al., 2007

3.3.3 Firn air H_2 measurements and calibration

Firn air samples from NEEM were analyzed at the Climate Science Centre, Commonwealth Scientific and Industrial Research Organisation (CSIRO) using gas chromatography coupled to an HgO reductive gas analyzer (HgO-RGA). CSIRO measurements were reported on the Max Plank Instituted 2009 (MPI09) scale, and analytical uncertainty is estimated at 2%. Firn air samples from South Pole, Megadunes, Summit, and Tunu were analyzed for H_2 by the NOAA/GML Carbon Cycle Group. Measurements were made using gas chromatography coupled to either an HgO-RGA (South Pole, Megadunes, Tunu) or He pulsed

discharge detector (HePDD; Summit). These measurements were reported on the NOAA-1996 (NOAA96) calibration scale. Analytical uncertainty is estimated at 2% (Novelli et al., 2009; Novelli et al., 1999). The World Meteorological Organization recommends reporting H_2 measurements on the MPI09 calibration scale. The measurements from NOAA/GML were corrected to the MPI09 scale using flask intercomparisons between NOAA and either AGAGE or CSIRO as described below. Additionally, a correction for detector non-linearity was applied to measurements made using the HgO-RGA (described below). Table 3.2 summarizes the measurements from each site.

Raw, uncorrected measurements from all five firn air campaigns are plotted in Figure 3.4. At South Pole, measurements above the lock-in zone are approximately constant near modern levels (~540 ppb). Below 116 m, H_2 levels decrease rapidly to 380 ppb at 123 m. Observed trends in firn air H_2 content are similar at Megadunes. H_2 levels are approximately constant between 540 and 550 ppb, above 64 m, the onset of the lock-in zone at Megadunes. H_2 levels decrease rapidly in the lock-in zone to 340 ppb at 69 m.

Measured depth profiles at the three Greenland sites display strong gradients above lock-in that reflect the intense seasonality of atmospheric H_2 in the northern hemisphere. Additionally, the depth profiles from NEEM and Summit both display sharp maximums in the lock-in zone. At NEEM, H_2 increases from 515 to 525 ppb between 5 and 35 m. H_2 levels decrease to 505 ppb at 62 m, just above the lock-in zone. H_2 levels then increase to a sharp maximum of 530 ppb at 68 m. H_2 levels decrease form the maximum rapidly to 485 ppb at 76 m. At Summit, measured H_2 levels decrease from 510 ppb at the surface 485 ppb at 68 m. H_2 levels then increases to 530 ppb at 78 m. H_2 levels decrease below that to 520 ppb at 80 m. The Tunu depth profile decreases

from 525 ppb at the surface to 495 ppb at 47 m. H_2 is nearly constant from 47-59 m and decreases to 410 ppb at 68 m.

The firn air measurements from South Pole, Megadunes, Summit, and Tunu are reported on the NOAA96 calibration scale. This calibration scale has been subject to slow drift over time due to changes in gravimetric gas standards. The H_2 calibration scale currently recommended by the World Meteorological Organization is the MPI09 scale (Jordan & Steinberg, 2011). We adjusted the NOAA firn air measurements from South Pole and Megadunes to the MPI09 scale using contemporaneous surface air flask measurements from NOAA/GML and AGAGE from Cape Grim Observatory, Tasmania (Figure 3.5). The AGAGE measurements used in this comparison were retroactively adjusted to the MPI09 scale in 2012 (Prinn et al., 2019).

The first batch of South Pole firn air flasks was analyzed in March 2001 at the same time as Cape Grim surface air flasks from December 2000 and January 2001. The NOAA/GML Cape Grim surface air flask measurements are 3.8 ppb lower than contemporaneous CSIRO/AGAGE data. This offset was applied to the South Pole firn air data from the first batch. The second batch of firn air samples was analyzed during February 2002 along with Cape Grim flasks from November 2001 and January 2002. The NOAA/GML Cape Grim surface air flask measurements from that period measurements for these months are biased low by 2.7 ppb, and this correction was applied to the second batch of firn air samples (Novelli, 2006; Prinn et al., 2019).

Megadunes firn air flasks were analyzed for H_2 at NOAA/GML in April 2004. During the same time period, Cape Grim surface air samples from January-March 2004 were also analyzed by NOAA/GML. The average offset between the AGAGE measurements and the NOAA/GML measurements during these months is 1.6 ppb (with AGAGE measurements higher than

NOAA/GML measurements; Novelli, 2006; Prinn et al., 2019). We applied a constant correction of 1.6 ppb to all of the Megadunes firn air measurements.

NOAA/GML surface flask measurements from 2013 are not available. Instead, we correct the Summit firn air flask measurements according to a matched flask intercomparison project between NOAA/GML and CSIRO (Figure 3.6; Paul Krummel, Personal Communication). H_2 measurements at CSIRO are tied to the MPI09 calibration scale. The average offset between CSIRO and NOAA/GML measurements in 2013 was 22.2 ppb with the NOAA/GML measurements lower than the CSIRO measurements. That correction was applied to all Summit firn air samples.

Measurements of the Tunu firn air were conducted at NOAA/GML during June of 1996. No surface flasks from Cape Grim were analyzed by NOAA/GML during that time, so we used the same matched flask intercomparison project to correct the Tunu measurements. The average offset between CSIRO and NOAA/GML during June and July of 1996 was 4.7 ppb with NOAA/GML measurements lower than the CSIRO measurements. A constant correction of 4.7 ppb was applied to all of the Tunu firn air measurements.

NOAA/GML H_2 measurements were initially calibrated using a single 530 ppb H_2 standard, assuming a linear detector response. We have applied an empirical correction to the firn air H_2 data from South Pole, Megadunes, and TUNU to account for the non-linear response of the HgO-RGA. The non-linearity bias is estimated to be -3 ppb at 453 ppb and -12 ppb at 312 ppb based on a few laboratory measurements made at NOAA/GML in 2009 (Gabrielle Petron and Andrew Crotwell, Personal Communication). The biases were linearly interpolated onto the firn air measurements, and the measurements were corrected for the bias (i.e., a measurement of 300 ppb would be corrected to 312 ppb). The response of the HePDD is linear, so the non-

linearity correction was not applied to the firn air measurements from Summit. The calibration and non-linearity corrections described above are small (<5%) and are not important for the main conclusions of this research.

The NOAA/GML H_2 measurements from the 2013 Summit campaign are being formally revised to the MPI09 calibration scale. The revised Summit measurements will be available from NOAA/GML (Gabrielle Petron; gabrielle.petron@noaa.gov). Measurements from the other firn air campaigns will not be revised. The firn air measurements from NEEM were made by CSIRO. H_2 measurements from CSIRO are calibrated using standards between 340 and 1000 ppb. CSIRO measurements were revised to the MPI09 scale in 2010. Therefore, the calibration and non-linearity corrections were not applied to the firn air measurements from NEEM. The firn air measurements from all five sites were corrected for gravitational fractionation using equation 3.2 as described in section 3.4.1. Measurements were then depth averaged to generate the finalized depth profiles used in the analyses (Figure 3.7).

Table 3.2- Summary of firn air H_2 measurements from each site

Site	Number of Samples	Unique Depths	Analysis Group	Analysis Method	Observed lock-in depth (m)
South Pole	96	31	NOAA	HgO-RGA	116
Megadunes	34	15	NOAA	HgO-RGA	64.5
NEEM	23	18	CSIRO	HgO-RGA	64
Summit	37	19	NOAA	HePDD	68.5
Tunu	48	22	NOAA	HgO-RGA	58

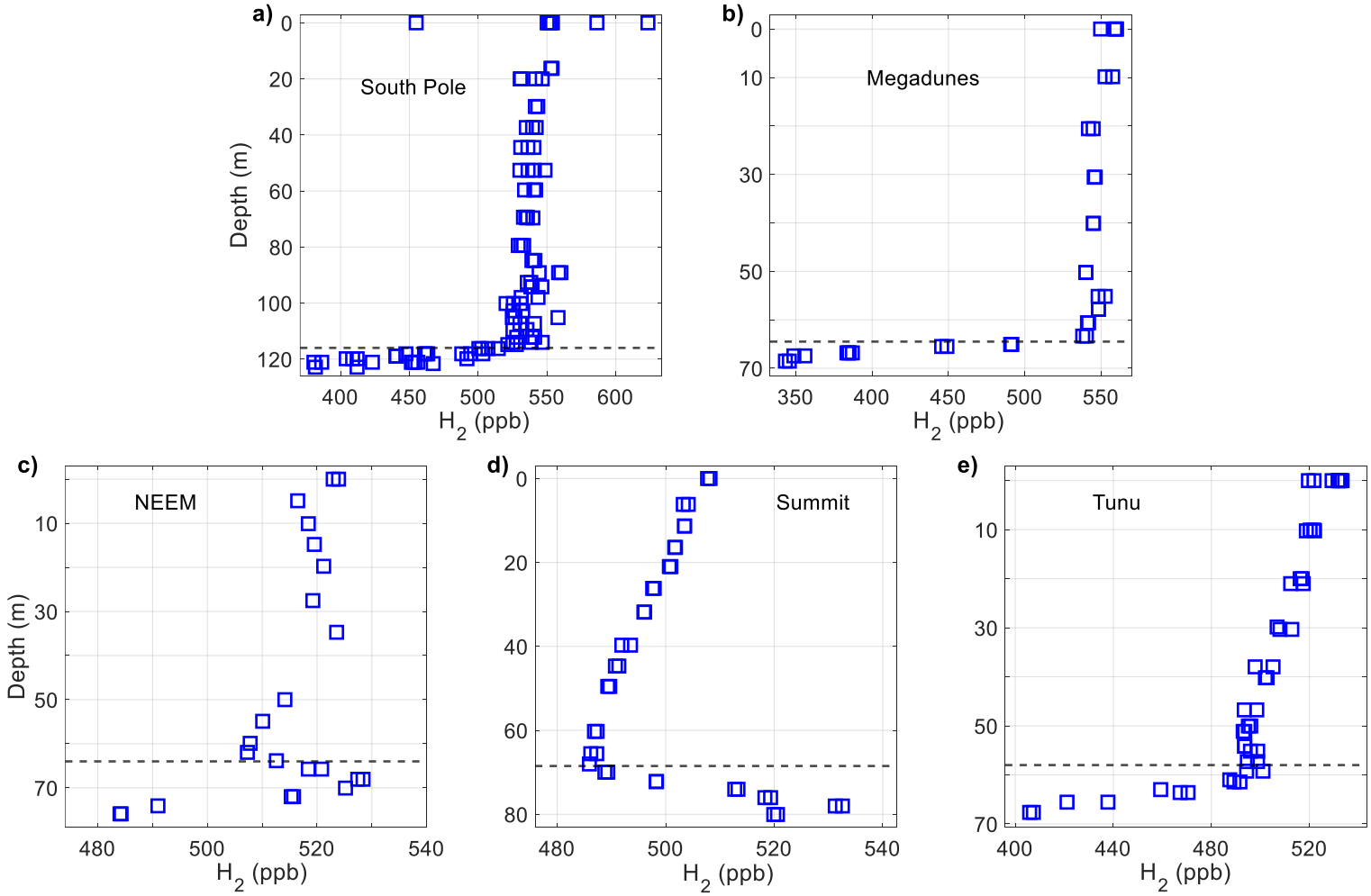

Figure 3.4- Raw measurements of H_2 in firn air from a) South Pole, b) Megadunes, c) NEEM, d) Summit, and e) Tunu. Dashed black lines are the lock-in depth at each site.

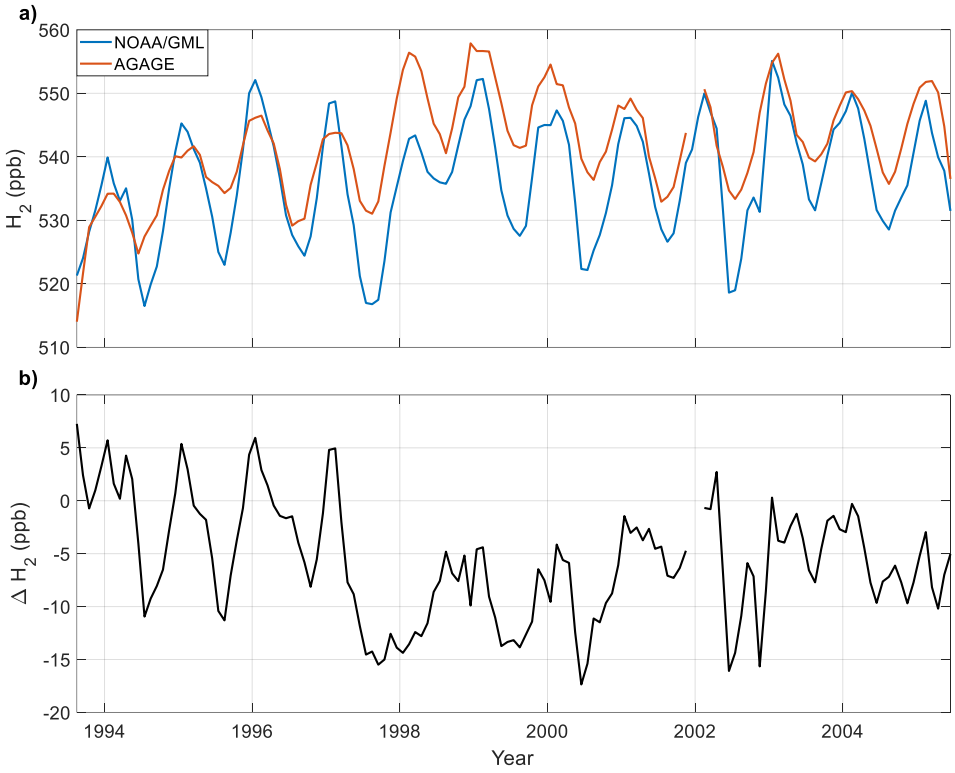

Figure 3.5- Intercomparison of surface flask measurements from Cape Grim, Tasmania used to adjust NOAA/GML measurements to the MPI09 calibration scale, a)- flask measurements from NOAA/GML (blue line) and AGAGE (orange line); b)- difference between NOAA/GML and AGAGE measurements (i.e. NOAA/GML-AGAGE)

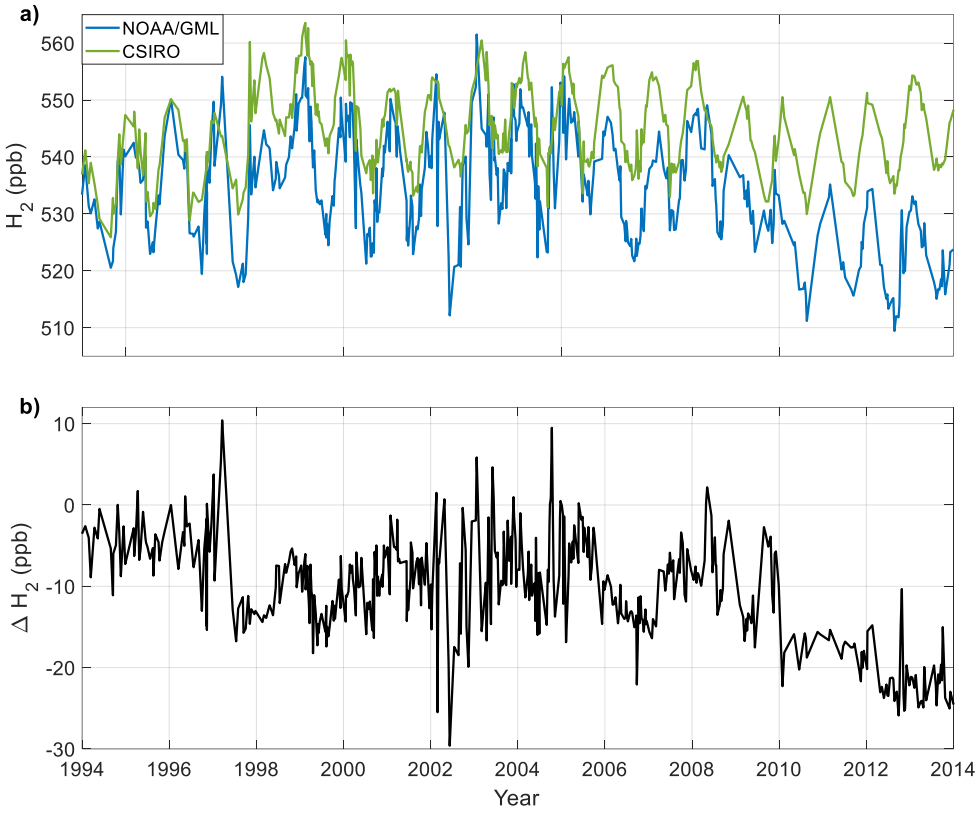

Figure 3.6- Intercomparison of surface flask measurements from Cape Grim, Tasmania used to adjust NOAA/GML measurements to the MPI09 calibration scale, a)- flask measurements from NOAA/GML (blue line) and AGAGE (orange line); b)- difference between NOAA/GML and CSIRO measurements (i.e. NOAA/GML-CSIRO)

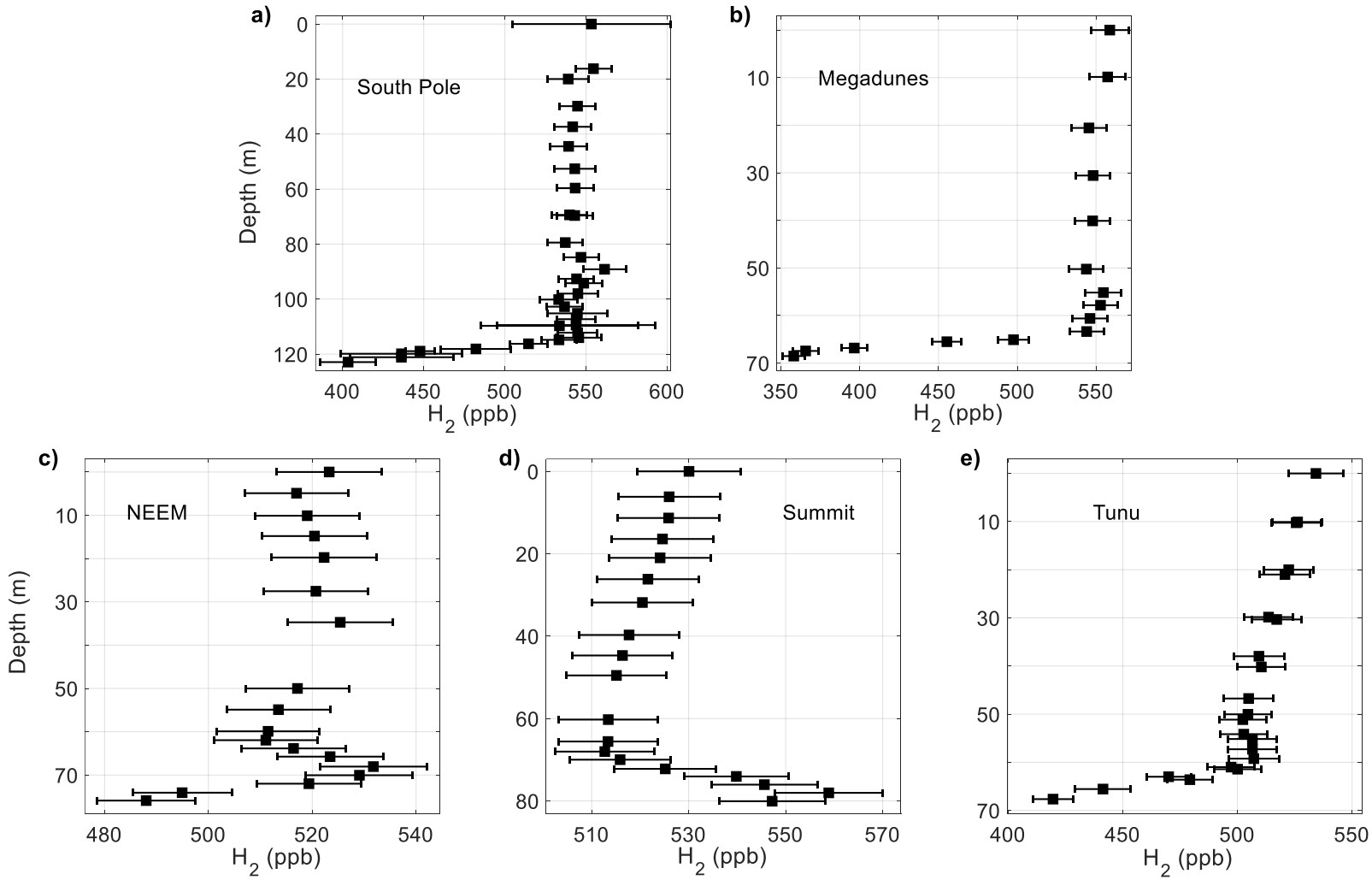

Figure 3.7- Depth-averaged measurements of H_2 in firn air adjusted to the MPI09 calibration scale and corrected for detector non-linearity and gravitational fractionation from a) South Pole, b) Megadunes, c) NEEM, d) Summit, and e) Tunu. Error bars are the propagated 2% measurement uncertainty.

3.4 Firn air modeling and inversions

3.4.1 Firn air model

The UCI_2 firn air model is a 1-dimensional finite-difference advective-diffusive model that is used to simulate the evolution of H_2 levels in firn air. The model is largely derived from the work of Severinghaus et al. (2010), and a complete model description is given in that work.. The model domain is broadly divided into an upper "diffusive zone" and lower "lock-in zone." In the diffusive zone, vertical gas transport occurs via wind-driven convective mixing and molecular diffusion. Diffusive mixing decreases with depth due to the increasing tortuosity of the firn. In the lock-in zone, vertical molecular diffusion ceases due to the presence of impermeable winter layers. Gas transport in the lock-in zone occurs primarily due to advection with a small non-fractionating mixing term. The model uses a forward Euler integration scheme and a time step of 324 s. There are two important differences between our implementation of the model and that of Severinghaus et al. (2010): 1) thermal diffusion is neglected, as it is unimportant for H_2, and 2) a pore close-off fractionation module is implemented to allow for rapid permeation of H_2 between open and closed pores. The model tracks the air content and composition in both open pores and closed bubbles as a function of time and depth. The model code is written and executed in MATLAB R2020a (Mathworks Inc.)

The site-specific bulk density profile (ρ_{firn}) is calculated from an empirical fit to density measurements of the firn core. Total porosity (s_{total}) is estimated from the density profile:

$$s_{total} = 1 - \frac{\rho_{firn}}{\rho_{ice}} \tag{3.1}$$

Where ρ_{ice} is the temperature dependent density of ice from Bader (kg m^{-3}; Bader, 1964). Partitioning between open and closed porosity, accumulation rate, and the depth of the lock-in zone onset are site-specific parameters (Table 3.1).

Model grid spacing is 0.5 m in the diffusive zone. Gas transport is dominated by convective mixing in the upper part of the diffusive zone, and by molecular diffusion in the lower part of the diffusive zone. To simulate non-fractionating convective mixing, an eddy diffusivity term is added to the classical one-dimensional firn air transport equation (Schwander et al., 1993; Severinghaus et al., 2010; Trudinger et al., 1997). Additionally, we neglect the typical gravitational term, and instead empirically correct the firn air measurements using the $\delta^{15}N$ depth profile. The correction is calculated from the $\delta^{15}N$ data for each borehole according to equation 2.4:

$$Corr_{grav}(z) = \frac{\delta^{15}N(z)}{1000} * \frac{\exp\left(g*z*\frac{\Delta m_g}{RT}\right)-1}{\exp\left(g*z*\frac{\Delta m_{15N}}{RT}\right)-1} \quad (3.2)$$

Where $Corr_{grav}$ is the depth dependent fractional correction for the gas of interest, $\delta^{15}N$ is the measured isotopic composition of N_2 each depth (‰), g is the gravitational acceleration constant (9.8 m s^{-2}), z is depth (m), R is the ideal gas constant (8.314 J mol^{-1} K^{-1}), T is the annual average temperature at the site, Δm_g is the difference in molar mass between the gas of interest and air, and Δm_{15N} is the difference in molar mass between $^{28}N_2$ and $^{29}N_2$ (.001 kg).

Equation 2.5 governs the evolution of the concentration of the gas of interest in the open pores (Severinghaus et al., 2010):

$$s_o \frac{\partial C}{\partial t} = \frac{\partial}{\partial z}\left(\frac{\partial C}{\partial z} * \left[s_o D_{mol}(z,T,P) + s_o D_{eddy}(z)\right]\right) - s_o w(z) \frac{\partial C}{\partial z} \quad (3.3)$$

Where s_o is the open porosity, C is concentration of the gas of interest (mol m^{-3}), D_{mol} is the depth, temperature, and pressure dependent molecular diffusivity constant (m^2 s^{-1}), D_{eddy} is the depth dependent eddy diffusivity (m^2 s^{-1}), and w is the downward velocity of the firn column (m s^{-1}). D_{mol} and D_{eddy} are tuned using the measured CO_2 and $\delta^{15}N$ depth profiles. D_{mol} is then scaled using the ratio of the gas phase diffusivity of CO_2 to the gas phase diffusivity of the gas of interest. Temperature and pressure dependent gas phase diffusivities are calculated from Reid et al. (1987).

Model grid spacing in the lock-in zone is 1 annual layer. There is no molecular diffusivity in the lock-in zone and gas transport occurs via downward advection of annual layers once per year. Small values of eddy diffusivity are prescribed in the upper part of lock-in. This non-fractionating mixing term is included to account for vertical airflow caused by barometric pressure fluctuations. The model parameterizations are validated by forcing the model with the atmospheric history of CO_2 and CH_4 from Law Dome and the NOAA flask air network and comparing the resulting modeled and measured depth profiles (Figure 3.8; Dlugokencky & Lan, 2020b, 2020a; Etheridge et al., 1996, 1998).

In addition to convective mixing, diffusion and advection, pore close-off fractionation is parameterized in the firn air model. As closed pores (bubbles) are advected downward in the firn, internal pressure increases, creating a partial pressure gradient which drives a net diffusive flux of highly mobile trace gases out of the bubbles, through the ice lattice, and into the open pores (Figure 1.5). The open pores are therefore enriched in these gases. This phenomenon affects gases with kinetic diameters (KD) <3.6 Å such as Ne, and He due to their large diffusivity in ice (Patterson et al., 2020; Severinghaus & Battle, 2006). As a result of pore close-

off fractionation, enrichments of nearly 10% in ^{22}Ne (KD= 2.75 Å) content were observed in the base of lock-in at South Pole and Megadunes.

Given its small molecular diameter (KD= 2.89 Å) pore close-off fractionation must affect H_2 in a similar manner to Ne (Patterson et al., 2020; Petrenko et al., 2013; Severinghaus & Battle, 2006). Two different parameterizations were used to simulate the pore close-off fractionation of H_2 in Patterson et al. (2020). In the "kinetic" parameterization, the time scale for diffusion between closed and open pores is assumed to be slow relative to the advective time scale. A small constant flux out of a given bubble is maintained until the bubble has compressed by 5% after which the flux out of the bubble decreases to 0. In the "equilibrium" parameterization, permeation through the ice lattice is assumed to be fast enough to achieve equilibrium between open pores and closed bubbles throughout the model domain. Reconstructions of atmospheric H_2 from South Pole firn air measurements were relatively insensitive to the choice of parameterization (Patterson et al., 2020). Recent laboratory measurements indicate that the permeability of H_2 in ice is sufficiently fast to equalize the partial pressure of H_2 in the open porosity and closed bubbles, supporting the use of the equilibrium parametrization (Chapter 2; Patterson & Saltzman, 2021). The equilibrium parameterization is described by equations 3.4-3.6:

$$P_n = (P_{bubble} x_{n(bubble)} s_c + P x_{n(firn)} s_o)/s_{total} \quad (3.4)$$

$$x_{n(bubble)} = P_n/P_{bubble} \quad (3.5)$$

$$x_{n(firn)} = P_n/P_{ambient} \quad (3.6)$$

Where P is pressure, x is mole fraction, and s_c is closed porosity. The subscripts *bubble* and *firn* distinguish between the closed and open porosity. Equations 3.4-3.6 are executed at every timestep in each grid cell in the model. Patterson et al. (Patterson et al., 2020) demonstrated that dissolution and vertical diffusion through the ice lattice may have effects on the order of 2-3% in lock-in zone if a permeation constant of $5.0*10^{-15}$ mol m^{-1} s^{-1} Pa^{-1} is assumed. Recent measurements of the permeation of H_2 in ice yield an estimate more than 100 times lower, so vertical diffusion through the ice lattice can be neglected on time scales relevant to firn air modeling (Patterson & Saltzman, 2021).

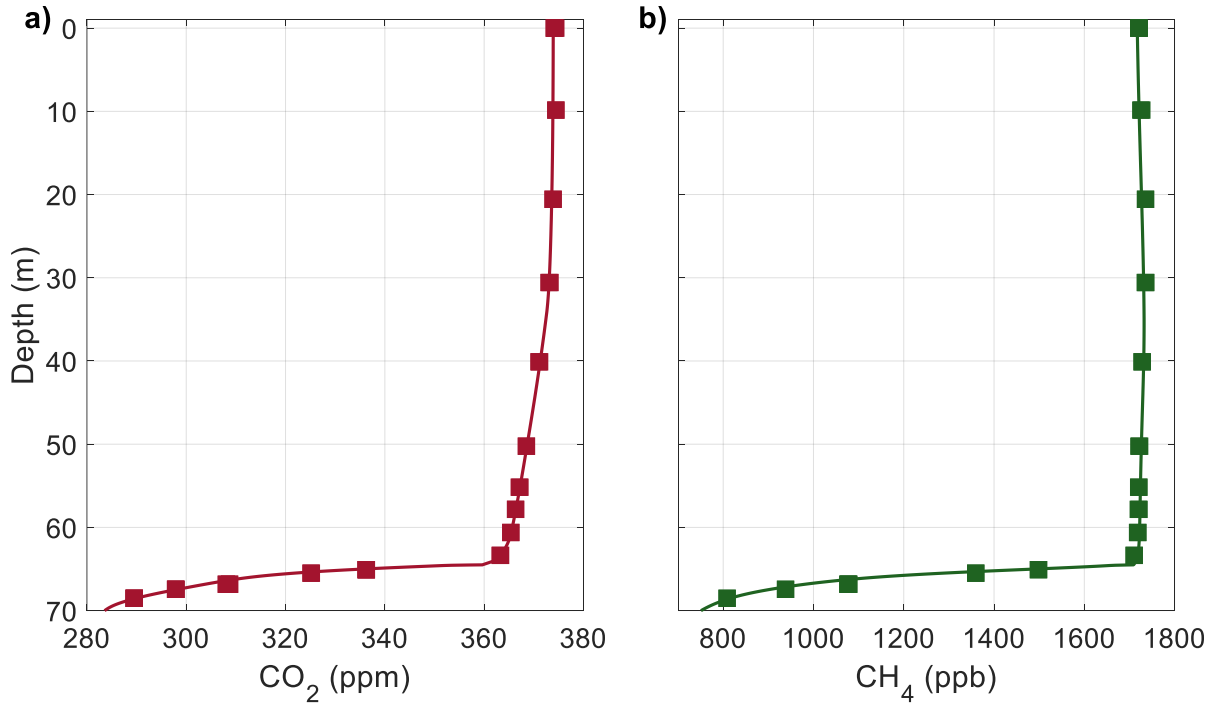

Figure 3.8- Measured and modeled depth profiles at Megadunes for a) CO_2 and b) CH_4. Solid lines are the model result and squares are measurements. The measurements have been corrected for gravitational fractionation as described by equation 3.2. The model was forced using atmospheric histories based on high resolution ice core measurements from Law Dome and modern flask air measurements from NOAA/GML (Dlugokencky & Lan, 2020b, 2020a; Etheridge et al., 1996, 1998)

3.4.2 Firn air inversion modeling

The firn air measurements are inverted to recover an atmospheric history of H_2. The exact inversion technique has evolved throughout this research. Three different methods were used over the course of this project (optimizer, matrix inversion, and Stan) as described below. All techniques employ depth dependent age distributions or Green's functions (*G(z,t);* Rommelaere et al., 1997). the firn air model is initialized with no H_2 in the firn air column, then forced with a 1-year pulse of H_2 at the surface, after which the surface concentration is set to 0. The model is integrated for 300 years, and the evolution of the pulse is tracked as a function of depth and time to produce the Green's functions. The Green's functions grow older and broader with depth (Figure 3.9). Given an atmospheric history ($H_{2(atm)}(t)$), modelled levels of H_2 in the firn are calculated according to equation 2.9:

$$H_2(z) = \sum_{t=0}^{300} H_{2(atm)}(t) * G(z,t) \quad (3.7)$$

Using Green's function allows for rapid iteration over many possible atmospheric histories without running the firn air model in forward mode. The inversion problem is under constrained with multiple atmospheric histories giving good agreement with the measured depth profile, and additional constraints are required to yield a unique solution. The additional constraints consist of an added smoothing term for the first and second inversion techniques and the assumption that the atmospheric history is auto-correlated for the third technique.

The Optimizer Technique

The "optimizer technique," utilizes the MATLAB optimizer *fmincon*, which employs an interior-point optimization algorithm, to minimize an objective function or "cost-function". The

optimizer technique was used to recover H_2 atmospheric histories from the firn air measurements at South Pole and Megadunes in Patterson et al. (2020; 2021). To prevent unrealistic extreme fluctuations in the reconstructions, the cost-function includes a smoothing term (Rommelaere et al., 1997):

$$f = \chi^2_{red} + S = \sum_{i=1}^{n} \frac{\left(\frac{(H_2\ model - H_2\ obs)^2}{\sigma^2}\right)}{n-1} + \alpha \sum_{t=0}^{t_n} \left(\frac{\partial^2 H_{2(atm)}(t)}{\partial t^2}\right)^2 \quad (3.8)$$

Where f is the cost, χ^2_{red} is the reduced chi square statistic, S is the smoothing term, σ is the analytical uncertainty (Figure 3.5), n is the number of unique depths, and α is an arbitrary, prescribed, dimensionless weighting parameter for the smoothing term.

The initial guess for the atmospheric H_2 history is a linear ramp from some "preindustrial" level of H_2 to 540 ppb at the time of firn air sampling. The preindustrial level for the oldest year is fixed at its initial value, and the H_2 levels for the other years are allowed to vary to minimize f. In order to assess the sensitivity of the inversion to the initial guess, the H_2 level is initialized at 4 different values: 270 ppb, 310 ppb, 350 ppb, and 390 ppb. The inversion is run for each initial guess and the results are compared. To assess sensitivity to smoothing, we vary α across an order of magnitude. To determine the impact of analytical uncertainty, we use a Monte Carlo method in which we repeatedly sample the normal distributions defined by the depth-averaged measurements and the analytical uncertainty at each depth (Figure 3.5). We then invert the synthetic depth profiles that are generated by the repeated sampling. We perform 1000 Monte Carlo samplings at each combination of initial condition and α for a total of 8000 inversion runs for each site, accounting for uncertainties due to initial conditions, smoothing, and

analytical uncertainties. The Monte Carlo runs do not assess bias in the modeling parameterizations or Green's functions.

The Matrix Inversion Technique

The "matrix inversion technique," is adapted from Menke (1989) as detailed by Rommelaere et al. (1997). The matrix inversion deterministically minimizes an objective function similar to equation 2.10. First, the calculated Green's functions are interpolated onto the depths of each firn air measurements from the model depths. The modeled H_2 level at each depth as a function of a given atmospheric history may be written using matrix notation:

$$\boldsymbol{h_{mod}} = \boldsymbol{G m_{atm}} \tag{3.9}$$

Where $\boldsymbol{h_{mod}}$ is a vector of length n with each element corresponding to the modeled H_2 level at each unique depth, $\boldsymbol{G}$ is an n by t_n matrix where each row corresponds to the Green's function for that unique depth (referred to as the "kernels" by Rommeleaere et al. (1997)), and $\boldsymbol{m_{atm}}$ is a vector of length t_n that contains the discrete atmospheric history. The objective function, which is minimized, is: $I_s + \kappa^2 L$, where I_s is the sum of the squared residuals between measured and modeled firn H_2 levels weighted by the analytical error, L is a measure of solution roughness (the sum of the second time derivatives of $\boldsymbol{m_{atm}}$), and κ^2 is an arbitrary weighting parameter that controls the influence of L on the solution:

$$I_s = (\boldsymbol{G m_{atm}} - \boldsymbol{h_{obs}})' \boldsymbol{W_e} (\boldsymbol{G m_{atm}} - \boldsymbol{h_{obs}}) \tag{3.10}$$

$$L = \boldsymbol{m_{atm}}' \boldsymbol{D}' \boldsymbol{D m_{atm}} \tag{3.11}$$

Where $\boldsymbol{h_{obs}}$ is a vector of length n, which contains the measured H_2 levels at each depth, $\boldsymbol{W_e}$ is an n by n diagonal matrix with the inverse squared analytical errors (σ^{-2}) on the diagonal, and $\boldsymbol{D}$ is the roughness matrix. $\boldsymbol{D}$ is a t_n by t_n tridiagonal matrix with -2 on the main diagonal, and 1 on both the upper and lower diagonals. 2 is substituted at for 1 at position (1,2) and (t_n,t_{n-1}) to avoid spurious calculations of the second derivative at the first and final elements of the history. The solution is given:

$$\boldsymbol{m_{est}} = (\boldsymbol{G'W_eG} + \kappa^2\boldsymbol{D'D})^{-1}\boldsymbol{G'W_eh_{obs}} \quad (3.12)$$

Where $\boldsymbol{m_{est}}$ is a vector of length t_n that contains the atmospheric history that minimizes the objective function. Sensitivity to κ^2 is assessed by varying the parameter across a wide range of values. Effects of the analytical uncertainty in the measurements are assessed using a Monte Carlo method that is identical that used in the optimizer technique. The matrix inversion technique produces results that are nearly identical to the optimizer technique. The primary advantages of the matrix inversion technique over the optimizer technique are: 1) computationally, the matrix inversion is faster than the MATLAB optimizer by a factor of >10, and 2) there is no specified initial condition to which the solution is sensitive.

The Stan Technique

The "Stan technique," implements a Bayesian hierarchical model using the Stan probabilistic software package (mcstan.org; Aydin et al., 2020). Rather than applying a smoothing term, the atmospheric history is modeled as an auto-correlated random variable:

$$\boldsymbol{m_{atm}}[t_n] \sim N(\boldsymbol{m_{atm}}[t_{n-1}], \beta\, \boldsymbol{m_{atm}}[t_{n-1}]) \quad (3.13)$$

The atmospheric mixing ratio at time t_n is normally distributed around the atmospheric mixing ratio at time t_{n-1} with a standard deviation of $\beta\, \boldsymbol{m_{atm}}[t_{n-1}]$. β is a positive scalar which may be specified or varied as a free parameter. The atmospheric history is related to the firn air measurements:

$$\boldsymbol{h_{obs}} \sim N(\boldsymbol{G m_{atm}}, \boldsymbol{\sigma}) \quad (3.14)$$

Where $\boldsymbol{\sigma}$ is a vector of length *n*, which contains the analytical uncertainties of the firn air measurements. Stan samples the joint posterior probability distribution for the parameters, $\boldsymbol{m_{atm}}$ and β using a fast Hamiltonian Markov Chain Monte Carlo algorithm (Carpenter et al., 2017). Parameters are sampled from uniform prior distributions unless otherwise specified. Inversions are carried out using the MatlabStan 2.15.1.0 interface to cmdstan 2.27.0. The advantages of the Stan technique are 1) No artificial smoothing criteria is imposed (instead the atmospheric history is assumed to be auto-correlated), 2) Stan allows us to easily explore sensitivity to assumptions about free parameters by encoding those assumptions as priors, and 3) Stan allows us to efficiently compute probability distributions for each free parameter (see Chapter 4). For these reasons, the Stan technique is used for the remainder of this dissertation.

Comparison of inversion methods

The three inversion techniques were compared using the Megadunes data. The optimizer and matrix inversion techniques are sensitive to the arbitrarily selected weighting parameter for the smoothing term (α or κ^2). The Stan technique does not include any arbitrarily selected parameters. Inversions were carried out for Megadunes using the matrix inversion technique with κ^2=1 and κ^2=0.01 and using the Stan technique (Figure 3.10). Results from the optimizer technique are nearly identical to the those from the matrix inversion technique with similar sensitivity to the choice of α, so those results are omitted. The priors for the Stan inversion are 1) atmospheric H_2 levels are between 0 and 1000 ppb, and 2) β is a positive scalar (by definition). The features of the results from the matrix inversion technique are highly dependent on κ^2. With κ^2=1, the matrix inversion technique results show atmospheric H_2 levels that are nearly constant from 1850-1890 and then increase monotonically to modern levels over the 20th century. With κ^2=0.01, H_2 levels decrease from 1850-1890, and then increase for 50 years to a local maximum in 1940. From 1940-1955, H_2 levels decrease. After 1955, H_2 levels gradually increase to their modern levels. Additionally, the uncertainty in the inversion results is sensitive to the choice of κ^2. More smoothing (higher κ^2) yields a lower uncertainty than less smoothing, despite using the same measurements and errors. The Stan technique removes this sensitivity to arbitrarily chosen parameters, instead relying on the assumption of auto-correlation in the atmospheric history.

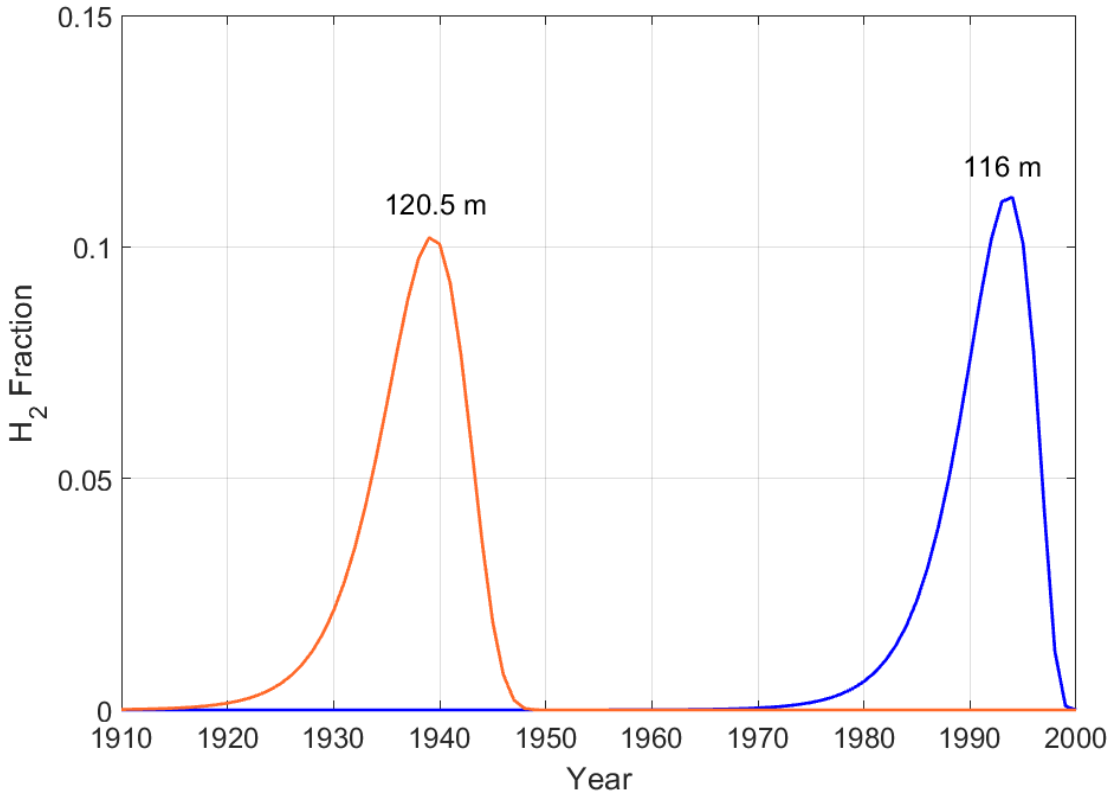

.

Figure 3.9- Age distributions or "Green's functions," calculated by the firn air model for South Pole at depths of 116.0 m (blue) and 120.5 m (orange). The age distribution at 120.5 m is older and broader than the age distribution at 116.0 m.

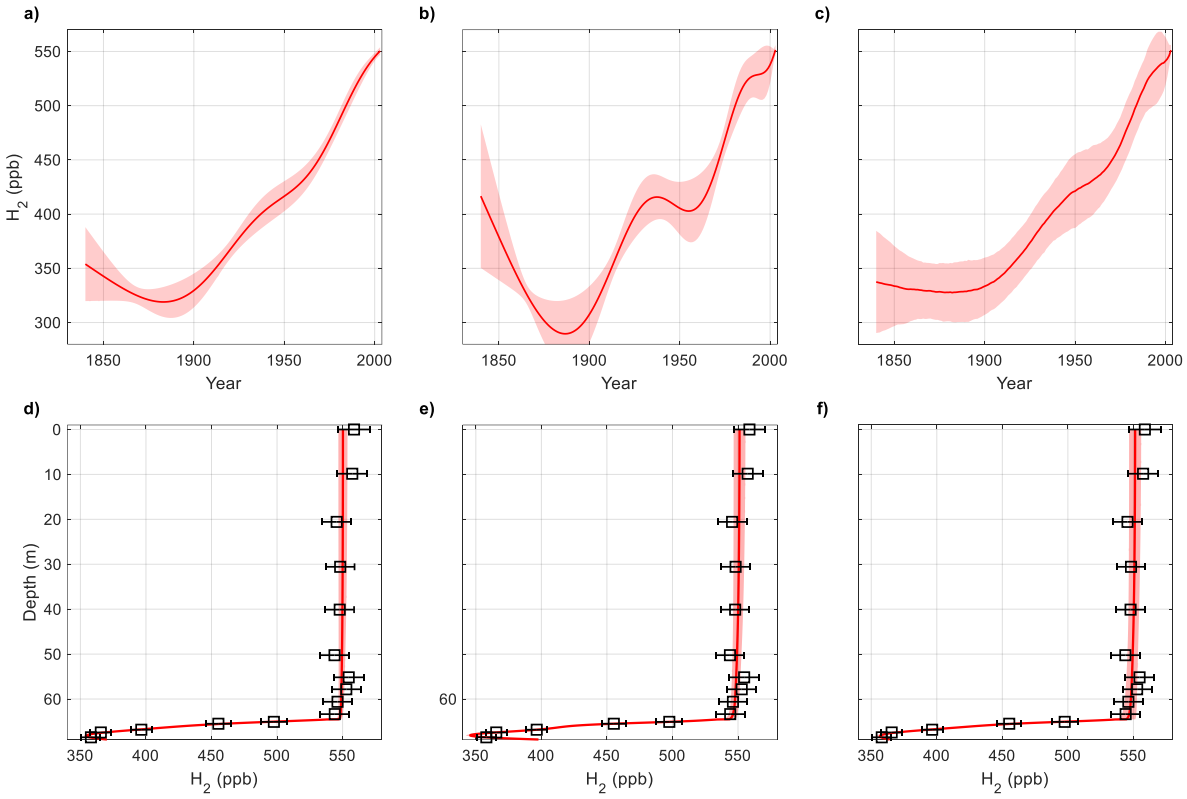

Figure 3.10- Atmospheric reconstructions (a-c) and measured firn air H_2 depth profiles (d-f) from Megadunes using various inversion methods. All three modelled depth profiles show good agreement with the measurements. Solid red lines are the mean result and shaded areas are the ±1σ uncertainties. Panels a, d) matrix inversion technique with κ^2=1; b, e) matrix inversion technique with κ^2=0.01; and c, f) Stan technique. Black boxes with error bars are the H_2 measurements and analytical uncertainties as in Figure 3.5b.

3.5 Antarctic firn results

3.5.1 Atmospheric reconstructions- Antarctica

High southern latitude atmospheric H_2 was reconstructed using firn air measurements from South Pole and Megadunes using the Stan technique with uniform priors for the atmospheric history and β (Figure 3.11). The sampling space was limited to positive numbers less than 1000 ppb for the atmospheric history, and β is positive by definition (Section 3.4.2).

The inversion results from South Pole constrain atmospheric levels as far back as 1930. Before 1930, the uncertainty in the reconstruction is large, indicating that the firn air

measurements cannot constrain atmospheric H_2 prior to this time. From 1930-1965, atmospheric H_2 increases at an average rate of 1.9 ppb y^{-1} from 356 ppb to 422 ppb. The rate of increase rises to 4.8 ppb y^{-1} for the next 10 years, with atmospheric levels reaching 470 ppb in 1975. From 1975 to 1997, the rate of increase is 3.6 ppb y^{-1}, with atmospheric levels reaching 550 ppb in 1997. After, 1997, there is a slight decrease to 545 ppb in 2000.

Firn air at Megadunes is significantly older than firn air at South Pole, and the reconstruction constrains atmospheric levels as far back as 1850. From 1850-1900, atmospheric H_2 is nearly constant at 335 ppb. From 1900-1965, atmospheric levels increase at an average rate of 1.6 ppb y^{-1} to 438 ppb. After 1965, the rate of increase rises to 3.0 ppb y^{-1}, with atmospheric levels reaching 550 ppb in 2003.

There is good agreement between the firn air histories from the two sites providing confidence in the atmospheric history of H_2 and in the modeling of the transport of a highly permeable gas in firn. The posterior distributions for β for the reconstructions are very similar (Figure 3.12). Both distributions are slightly right skewed. For the South Pole reconstruction, the median value is 0.033 and the mean value is 0.034. For the Megadunes reconstruction, the median value 0.030 and the mean value is 0.032.

We also conducted a joint reconstruction using the Stan technique. The joint reconstruction calculates the most probable atmospheric history given the firn air data from both South Pole and Megadunes (Figure 3.13). Joint reconstructions can help reduce error that is caused by bias in the modeling parameterizations or age distributions provided that the bias in the age distributions results from site-specific parameterizations and not inherent biases in the model physics. Prior to 1930, the joint reconstruction is dominated by the Megadunes data, with the atmospheric history nearly identical to the Megadunes firn air reconstruction in Figure 3.9 Between 1930 and 1965,

the joint reconstruction falls between the Megadunes and South Pole reconstructions. From 1965-1990, the independent reconstructions are identical, and the joint reconstruction shows good agreement with both. Interestingly, between 1990 and 2000, the joint reconstruction shares the features of the South Pole Reconstruction with a peak in atmospheric H_2 in 1997 and a small decrease until 2000. After 2000, there is a small increase in H_2 levels, which mirrors the increase in the independent Megadunes reconstruction. There is good agreement between the modelled and measured depth profiles in Figures 3.13b and 3.13c.

There is also good agreement between the firn air histories and the available modern flask measurements (Figure 3.11a). The flask data include measurements from 1985-1989 at Palmer Station, Antarctica and Cape Grim Observatory, Tasmania made by Khalil and Rasmussen (Khalil & Rasmussen, 1990), from 1992-2003 at Palmer, Syowa, South Pole, and Halley Stations, Antarctica and Cape Grim Observatory, Tasmania made by NOAA/GML (Novelli, 2006; Novelli et al., 1999), and from Casey, South Pole, and Mawson Stations, Antarctica, and Cape Grim and Macquarie Island, Tasmania made by CSIRO (Langenfelds et al., 2002). The NOAA/GML flask measurements were adjusted from the NOAA96 to the MPI09 calibration scale similarly to the firn measurements as described in section 3.3.3. The reconstructions were not constrained by the flask data.

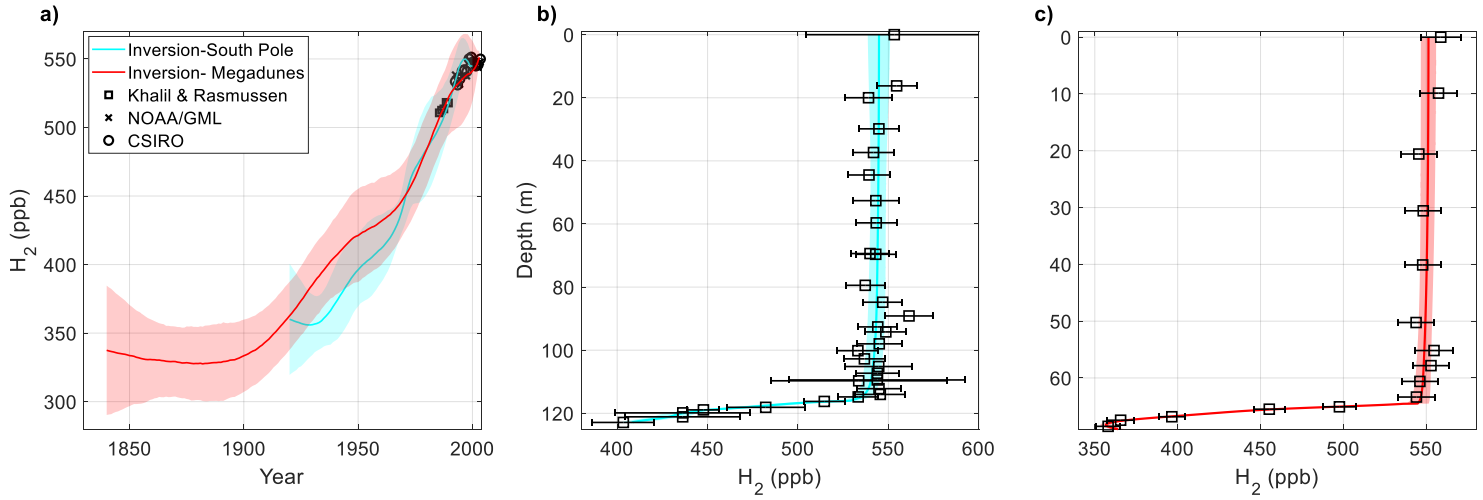

Figure 3.11- Firn air reconstructions from two Antarctic sites and associated depth profiles. a) blue line and shading- result from South Pole and associated ±1σ uncertainty; red line and shading- result from Megadunes and associated ±1σ uncertainty; black squares, black x's, and black circles – observed atmospheric H_2 annual means from high southern latitude sites from 1985-1989 and 1992-2003 (Khalil & Rasmussen, 1990; Langenfelds et al., 2002; Novelli, 2006; Novelli et al., 1999); b) black squares with error bars- measured H_2 depth profile at South Pole as in Figure 3.5a; blue line and shading- modeled depth profile using the atmospheric history plotted in blue in a) with the propagated ±1σ uncertainty; c) black squares with error bars- measured H_2 depth profile at Megadunes as in Figure 3.5b; red line and shading- modeled depth profile using the atmospheric history plotted in red in a) with the propagated ±1σ uncertainty

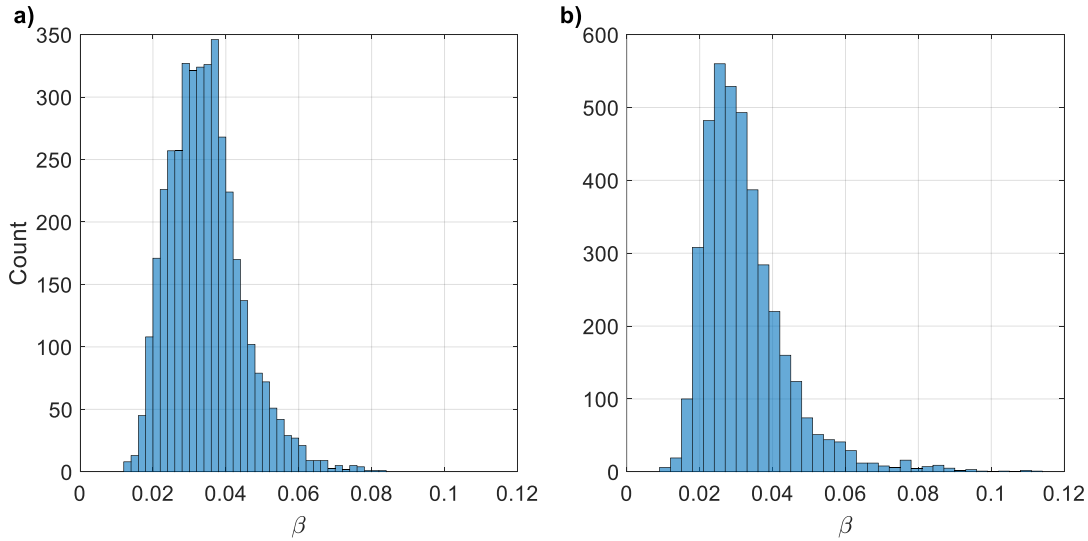

Figure 3.12- Histograms for the posterior distributions of β for a) the South Pole reconstruction and b) the Megadunes reconstruction

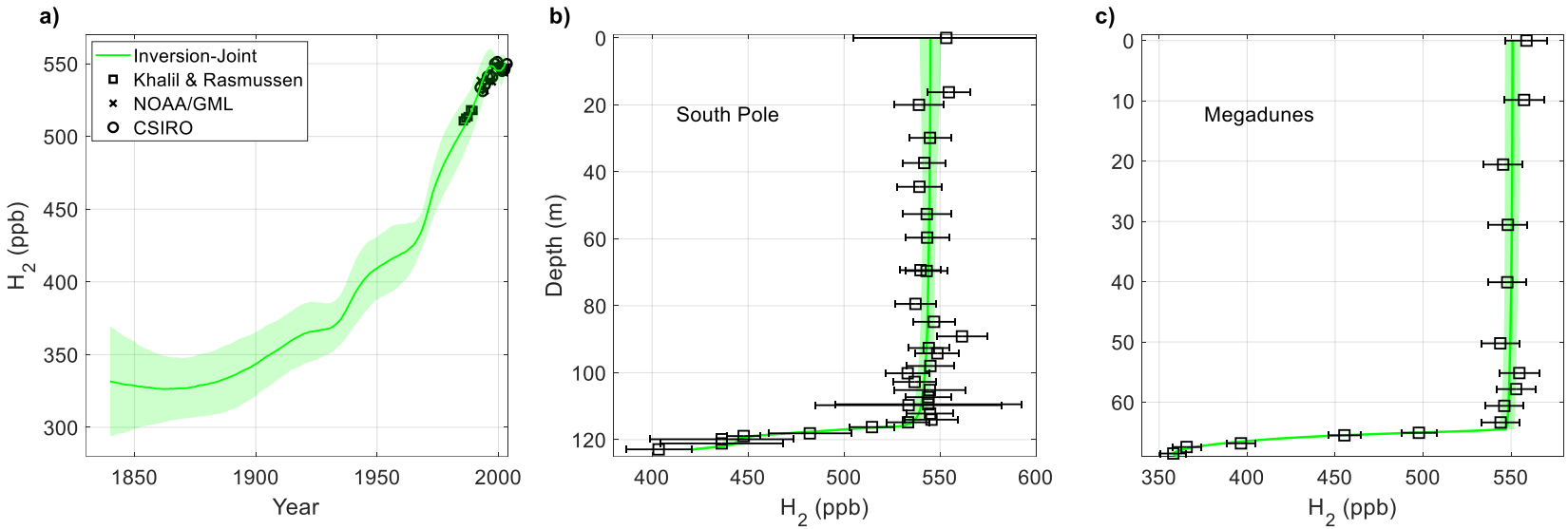

Figure 3.13- Joint atmospheric H_2 reconstructions from two Antarctic sites and associated depth profiles. a) green line and shading- result of the joint reconstruction and associated ±1σ uncertainty; black squares, black x's, and black circles – observed atmospheric H_2 annual means from high southern latitude sites from 1985-1989 and 1992-2003 (Khalil & Rasmussen, 1990; Langenfelds et al., 2002; Novelli, 2006; Novelli et al., 1999); b) black squares with error bars- measured H_2 depth profile at South Pole as in Figure 3.5a; green line and shading- modeled depth profile using the atmospheric history plotted in a) with the propagated ±1σ uncertainty; c) black squares with error bars- measured H_2 depth profile at Megadunes as in Figure 3.5b; green line and shading- modeled depth profile using the atmospheric history plotted in a) with the propagated ±1σ uncertainty

3.5.2 Assessing bias in the atmospheric reconstruction- Antarctica

The reconstruction technique does not assess bias or uncertainty in the model parameterizations (e.g., molecular diffusivity) or the Green's functions (age distributions) used in the inversion. Bias in the model can arise from inaccurate parameterizations, or incorrect assumptions such as constant accumulation rates and temperature. To assess bias or uncertainty in the inversion technique, we exploit the established atmospheric history of CH_4. Atmospheric CH_4 levels over the last several centuries are well constrained by high-resolution ice core measurements from Law Dome and modern flask measurements from NOAA/GML (Dlugokencky & Lan, 2020b; Etheridge et al., 1998). When the Megadunes firn air model is forced with this atmospheric history, the modeled depth profile shows a small bias in the lock-in zone relative to measured depth profile, indicating some bias in the firn-air model (Figure 3.6).

We developed an empirical correction for the bias. At each depth, the bias is calculated by translating the age distribution at that depth either older or younger to optimize the fit between modeled and measured CH_4 levels. At South Pole, the maximum bias is for the measurement at a depth of 121.1 m. The age distribution is biased old by 26 years or 30.5% of the calculated mean CH_4 age at that depth. At Megadunes, the maximum bias is at a depth of 66.8 m. The age distribution is biased old by 17 years or 20.8% of the mean CH_4 age at that depth (Figure 3.14).

Results from CH_4 reconstructions using both the original and corrected age distributions with the Stan technique are plotted in Figure 3.15. For all reconstructions, the corrected age distributions produce substantially better fit to the established atmospheric history compared to the original age distributions. For the South Pole reconstruction, using the corrected age distributions increases the R^2 between the reconstruction and the established history from .894 to

.995. The RMSE decreases from 89.0 to 18.6 ppb. For the Megadunes reconstruction, R^2 increases from .895 to .995, and the RMSE decreases from 97.4 to 21.4 ppb. For the joint reconstruction, the R_2 increases from .873 to .995, and the RMSE decreases from 107 to 20.5 ppb.

We validated our approach to correcting the age distributions for bias by applying the CH_4-based correction to reconstructions of CO_2 (South Pole and Megadunes) and CH_3CCl_3 (Megadunes only). The atmospheric history of CO_2 over the last 200 years is similarly well-constrained by ice core measurements from Law Dome and by NOAA/GML flask measurements (Dlugokencky & Lan, 2020a; Etheridge et al., 1996). CH_3CCl_3 is an atmospheric trace gas of solely industrial origin. Flask measurements of CH_3CCl_3 began in 1978 Prinn et al., 2005). Prior to 1978, industrial emissions are well constrained, and atmospheric levels of CH_3CCl_3 may be calculated with a high degree of certainty (Montzka et al., 2010). Firn air reconstructions using both the original, model calculated age distributions and the corrected age distributions were compared to the established histories. The applied corrections were identical to those calculated using CH_4. For example, the age distributions from 121.1 m at South Pole were translated so that the mean CO_2/CH_3CCl_3 age is 30.5% younger, and the distributions from 66.8 m at Megadunes were translated so that the mean age is 20.8% younger. Original and corrected reconstructions are plotted in Figures 3.16 and 3.17, and Table 3.3 summarizes the R^2 and RMSE for each reconstruction.

Reconstructions of CO_2 using the original age distributions show much less bias than reconstructions of CH_4. The R^2 values were .964, .974, and .979 for South Pole, Megadunes, and joint reconstructions respectively. The lower bias relative to the established history is the result of: 1) the tuning of model diffusivities based on CO_2 and 2) the relatively slower rate of change

of CO_2 in the atmosphere. Despite the already good agreement between the firn air reconstructions and established histories, applying the CH_4-based corrections to the CO_2 age distributions improved the agreement between the firn air reconstructions and the established history. R^2 values increased to .978, .985, and .988 for South Pole, Megadunes, and the joint reconstruction respectively. Applying the CH_4-based correction to the CH_3CCl_3 reconstruction from Megadunes increased the R^2 between the reconstruction and established history from .902 to .984. The atmospheric history of CH_3CCl_3 is qualitatively different than that of CO_2 and CH_4, with a rapid rise from 1960-1990 and a sharp decline thereafter. The results from the CO_2 and CH_3CCl_3 reconstructions demonstrate the broad applicability of the CH_4-based correction for gases with histories similar to that of CH_4 (i.e. CO_2) and for gases with very different histories (i.e. CH_3CCl_3). Here, we are using the correction empirically to account for bias in our reconstruction technique without regard for the underlying physical processes. In the future, investigating the calculated age distribution of gases with well-established atmospheric histories could lead to better firn air model parameterizations and improved representation of transport processes.

The results from applying the CH_4-based correction to the H_2 reconstructions are shown in Figure 3.18. For the South Pole reconstruction, corrected H_2 levels are ~10% lower than the original reconstruction in 1950. The difference between the original reconstruction and the corrected reconstruction decreases gradually until 1990, when the two reconstructions converge. It is notable that, unlike the original reconstruction, the uncertainty band increases dramatically prior to 1950. This occurs because, according to the CH_4-based correction, the age distributions for the deepest measurements are biased old. Shifting these age distributions younger yields more uncertainty during the oldest parts of the reconstruction. For the Megadunes reconstruction,

there is good agreement between the original and corrected reconstructions from 1850-1910. From 1910-1950, the difference between the two reconstructions increases to approximately 7% in 1950, with the corrected reconstruction lower than the original. After 1950, the difference decreases and the two reconstructions are separated by <10 ppb between 1970 and 2003. The trends are similar for the joint reconstruction, with good agreement between 1850 and 1890. After 1890, the difference between reconstructions increases slowly and reaches a maximum in of 7% in 1950. After 1950, the two reconstructions slowly converge, with good agreement after 1980. In all three cases, the corrected reconstructions fall within the $\pm 2\sigma$ uncertainty bounds of the original reconstructions. The differences between the original and corrected reconstructions are not important for the main conclusions of this dissertation.

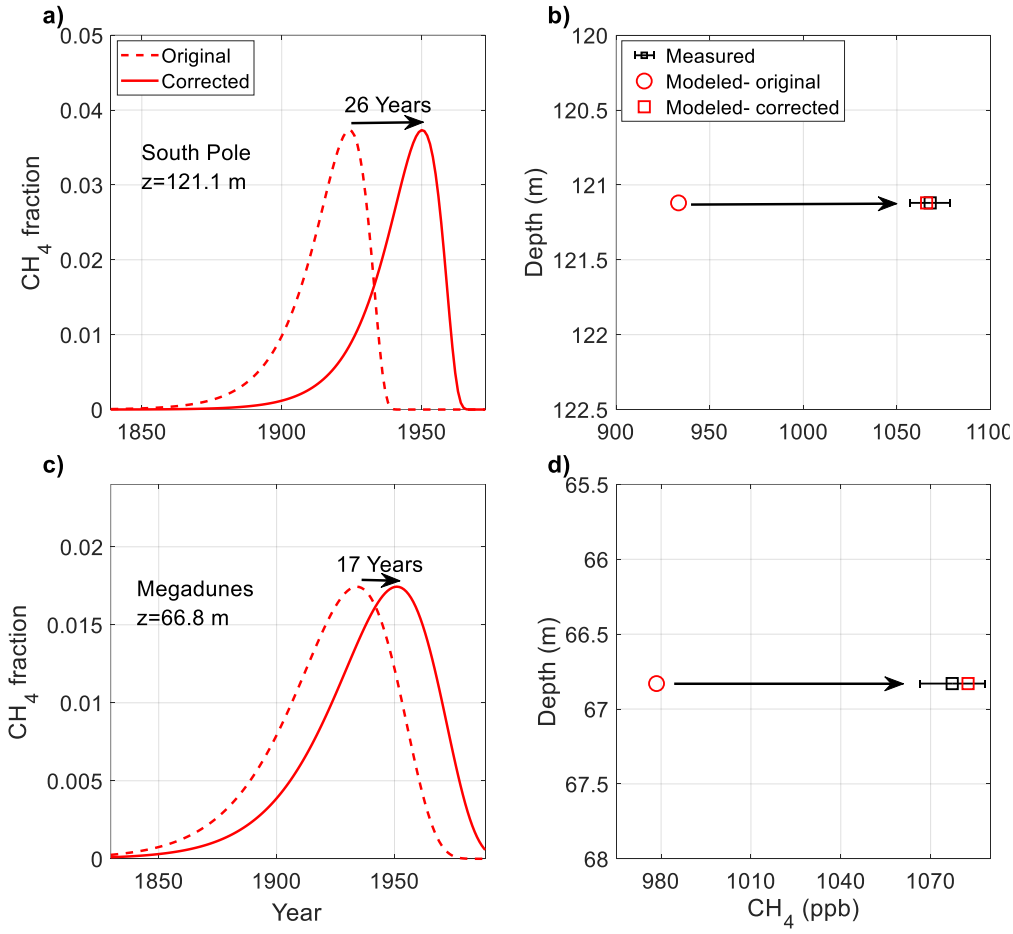

Figure 3.14- Development of the CH_4-based age distribution correction a) dashed red line- original calculated CH_4 age distribution for a depth of 121.1 m at South Pole, solid red line- the same modeled age distribution, translated 26 years younger to yield better agreement with the measurements when the model is forced with the established atmospheric history; b) black square with error-bars- measured H_2 level at 121.1 m at the South Pole; red circle- modeled H_2 level corresponding to the dashed red line a); red square- modeled H_2 level corresponding to the solid red line in a); c) and d)- as in a) and b) for a depth of 66.8 m at Megadunes. The applied correction is 17 years.

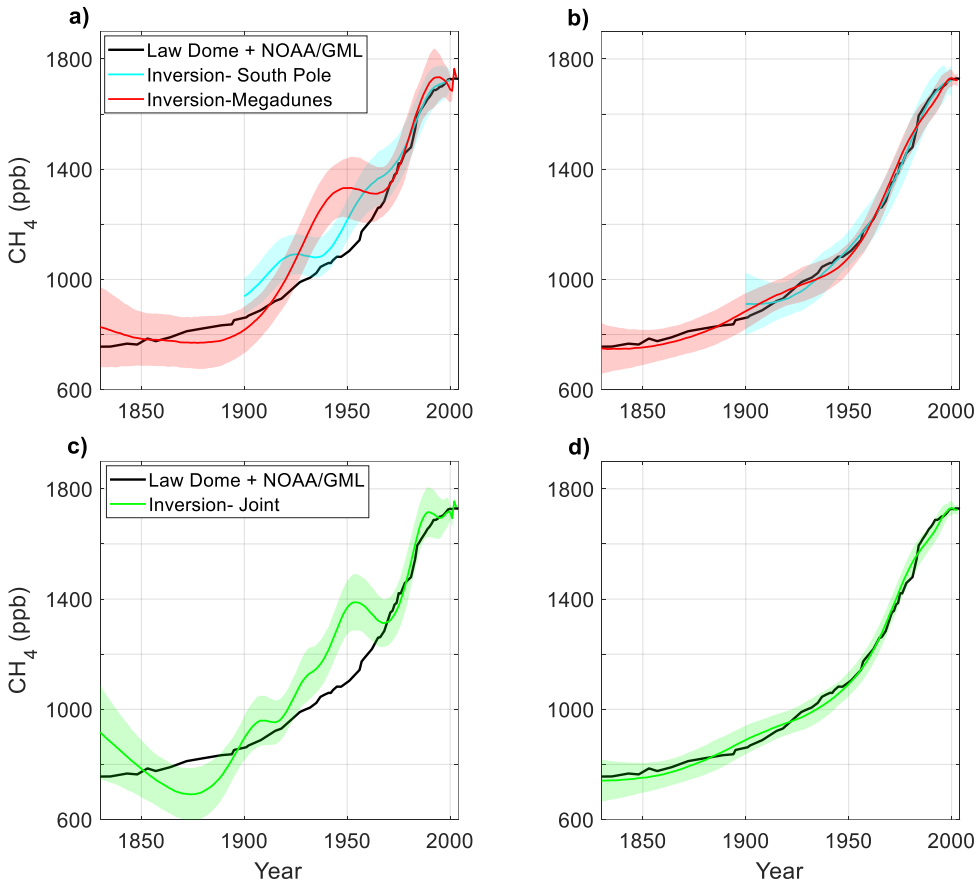

Figure 3.15- Reconstructions of atmospheric CH_4 using original and corrected age distributions a) blue line and shading- reconstruction from South Pole using original age distributions with the ±1σ uncertainty; red line and shading- reconstruction from Megadunes using original age distributions with the ±1σ uncertainty; black line- established atmospheric history of CH_4 from Dlugokencky & Lan (2020b) and Etheridge et al. (1998). b) as in a) using corrected age distributions. c) green line and shading- joint reconstruction and ±1σ uncertainty using the original age distributions; d) green line and shading- joint reconstruction and ±1σ uncertainty using the corrected age distributions

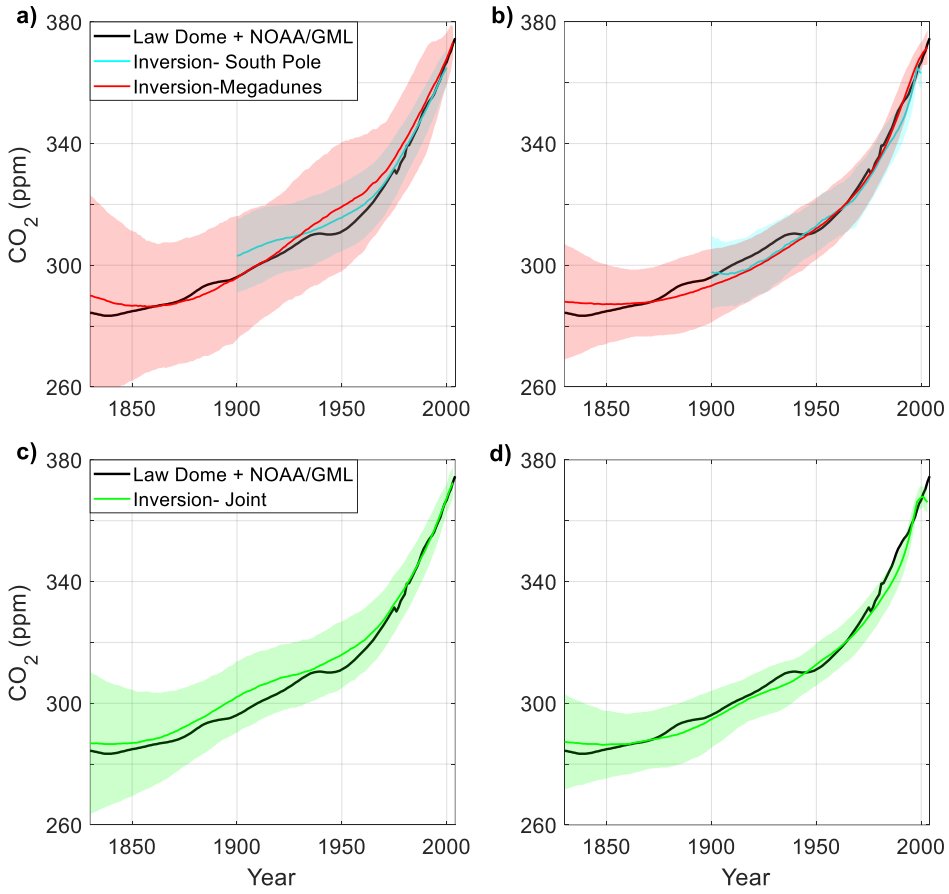

Figure 3.16- Reconstructions of atmospheric CO_2 using original age distributions and age distributions with the CH_4-based corrections applied; a) blue line and shading- reconstruction from South Pole using original age distributions with the ±1σ uncertainty; red line and shading- reconstruction from Megadunes using original age distributions with the ±1σ uncertainty; black line- established atmospheric history of CO_2 from Dlugokencky & Lan (2020a) and Etheridge et al. (1996). b) as in a) using corrected age distributions. c) green line and shading- joint reconstruction and ±1σ uncertainty using the original age distributions; d) green line and shading- joint reconstruction and ±1σ uncertainty using the corrected age distributions

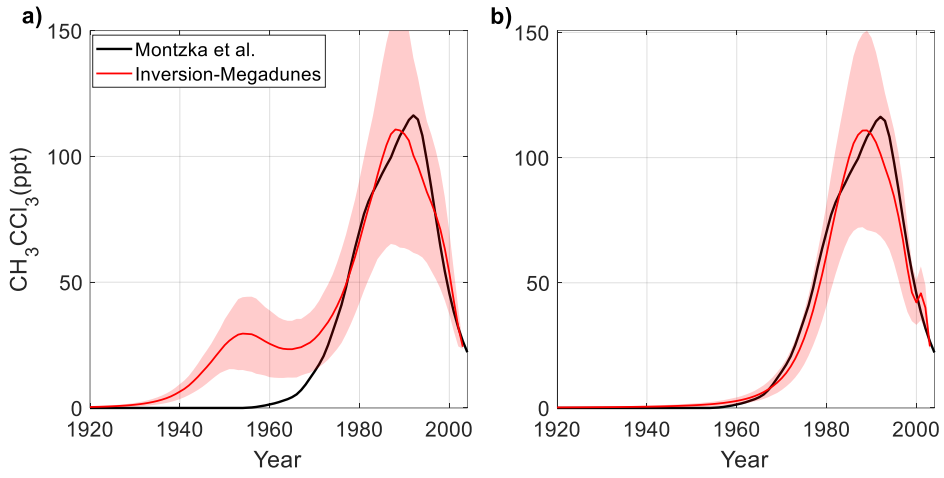

Figure 3.17- Reconstructions of atmospheric CH_3CCl_3 using original age distributions and age distributions with the CH_4-based corrections applied; a) red line and shading- reconstruction from Megadunes using original age distributions with the ±1σ uncertainty; black line- established atmospheric history of CH_3CCl_3 from Montzka et al. (2010) b) as in a) using corrected age distributions

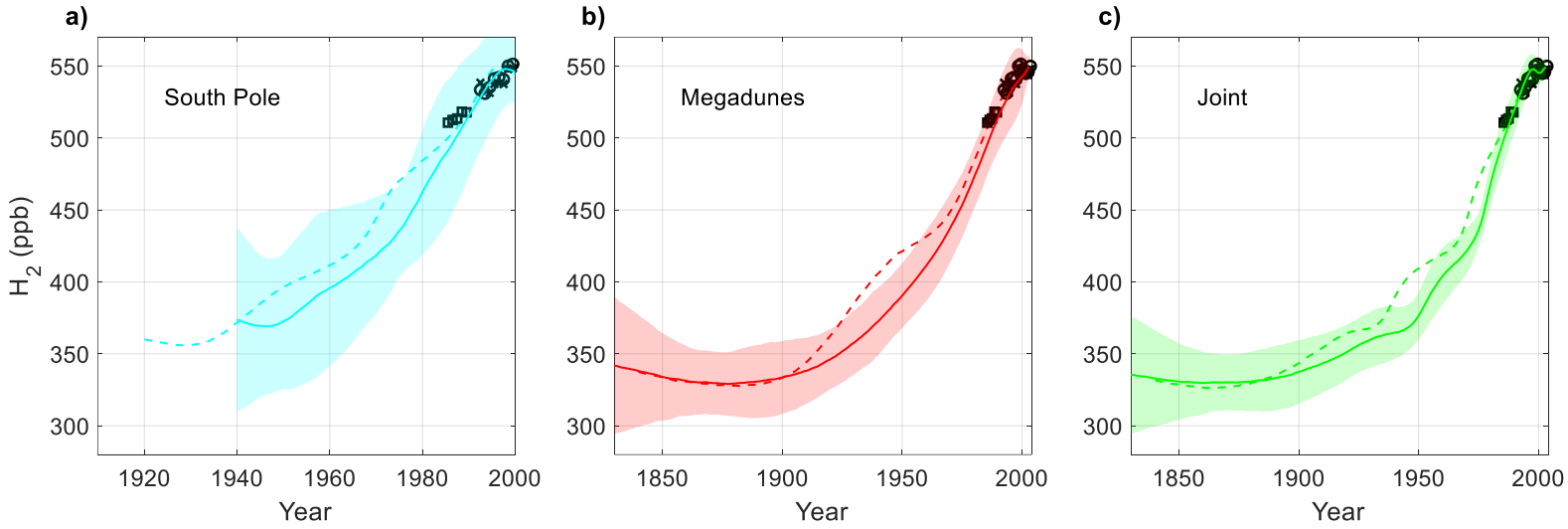

Figure 3.18- Comparison of atmospheric H_2 reconstructions using original age distributions and age distributions with the CH_4-based corrections applied. a) dashed blue line- South Pole reconstruction using the original age distributions; blue line and shading- South Pole reconstruction using corrected age distributions with the $\pm 1\sigma$ uncertainty; black squares, black x's, and black circles – observed atmospheric H_2 annual means from high southern latitude sites from 1985-1989 and 1992-2003 (Khalil & Rasmussen, 1990; Langenfelds et al., 2002; Novelli, 2006; Novelli et al., 1999); b) and c)- as in a) for the Megadunes reconstruction and the joint reconstruction respectively.

Table 3.3- R^2 and RMSE values for reconstructions compared to established atmospheric histories using original age distributions and corrected age distributions were calculated for CH_4, CO_2, and CH_3CCl_3.

Gas	Original						Corrected					
	South Pole		Megadunes		Joint		South Pole		Megadunes		Joint	
	R^2	RMSE	R^2	RMSE	R^2	RMSE	R^2	RMSE	R^2	RMSE	R^2	RMSE
CH_4	0.894	89.0 ppb	0.895	97.4 ppb	0.873	107 ppb	0.995	18.6 ppb	0.995	21.4 ppb	0.995	20.5 ppb
CO_2	0.964	3.6 ppm	0.974	3.7 ppm	0.979	3.3 ppm	0.978	2.8 ppm	0.985	2.7 ppm	0.988	2.5 ppm
CH_3CCl_3	N/A	N/A	0.902	9.6 ppt	N/A	N/A	N/A	N/A	0.984	3.9 ppt	N/A	N/A

3.6 Greenland firn results

3.6.1 Atmospheric reconstructions- Greenland

Atmospheric H_2 reconstructions were carried out for the high northern latitudes using firn air measurements at NEEM, Summit, and Tunu (Figure 3.19). The reconstruction technique is almost identical to the technique used for the Antarctic reconstructions. The only difference in the methodology used in the Greenland reconstructions is the exclusion of measurements that are affected by seasonality. The seasonal amplitude of atmospheric H_2 in the northern hemisphere is 60-70 ppb today, more than double that in the southern hemisphere. In Greenland, H_2 levels in the upper firn layers are strongly influenced by seasonal variations and firn air reconstructions cannot accurately reconstruct such high frequency variability. Therefore, measurements from the upper part of the firn were excluded from the reconstructions. A cut-off depth was determined by forcing the firn air model in forward mode with an atmospheric history that consisted of constant annually averaged H_2 levels with a realistic seasonal cycle imposed. Depths where the H_2 concentration varied by more than 1% from the annual average were excluded from the reconstruction. The cut-off depths were 62 m, 66 m, and 50 m for NEEM, Summit and Tunu respectively.

The NEEM, Summit, and Tunu sites have different physical characteristics (mean annual temperature and accumulation rate), and therefore very different firn air age distributions. Firn air measurements from NEEM are able to constrain atmospheric H_2 levels after 1950. From 1950-1989, atmospheric levels increase at an average rate of 3.1 ppb y^{-1} from 425 ppb to 545 ppb. After 1989, atmospheric levels decrease at an average rate of 1.6 ppb y^{-1} reaching 515 ppb in 2008.

The firn air at Summit is younger than at other sites and cannot constrain atmospheric H_2 prior to 1975. The Summit reconstruction shows atmospheric H_2 increasing from 505 ppb in 1975 to 530 ppb in 1993, an average rate of 1.5 ppb y^{-1}. After 1993, there is a slight decrease in atmospheric H_2 levels until 2003. After 2003, atmospheric H_2 decreases more rapidly at a rate of 1.5 ppb y^{-1}, reaching 515 ppb in 2013.

The Tunu firn air measurements can constrain atmospheric H_2 as far back as 1930. Prior to 1930, the uncertainty in the atmospheric history is too large for the reconstruction to be meaningful. According to the Tunu reconstruction, atmospheric H_2 rose from 370 ppb in 1930 to 510 ppb in 1990-1992, an average rate of 2.3 ppb y^{-1}. After 1992, H_2 levels decreased at a rate of 1.5 ppb y^{-1} to just over 500 ppb in 1996.

A joint reconstruction for atmospheric H_2 over Greenland was conducted utilizing the data from all three sites (Figure 3.20). The joint reconstruction is qualitatively different from the independent reconstructions. These differences are caused by an apparent offset between the data from Tunu and the other sites (further discussed below). The reconstruction shows atmospheric H_2 increasing from 330 ppb in 1930 to 525 ppb in 1986 at an average rate of 3.5 ppb y^{-1}. Over the next 10 years, atmospheric H_2 decreases at an average rate of 2.5 ppb y^{-1}, reaching 500 ppb in 1995. After 1995, H_2 levels increase exceptionally rapidly to 565 ppb in 1999. After 1999, atmospheric H_2 decreases rapidly at an average rate of 7.8 ppb y^{-1} to 512 ppb in 2006. Atmospheric H_2, then rises slightly, reaching 525 ppb in 2010 and decreases again to 512 ppb in 2013. The reconstruction's late-20th century "triple peak" structure and exceptionally rapid fluctuations in atmospheric H_2 are not supported by the NOAA/GML flask measurements from Summit, Greenland. These features are an artifact of the apparent offset between the Tunu data and the other sites. For example, H_2 levels increase 65 ppb between 1995 and 1999. This

remarkably rapid increase is the result of the probability model compensating for the offset. The reconstruction is forced lower by the Tunu measurements prior to 1996. After 1996, the reconstruction is no longer constrained by the Tunu measurements, and the reconstruction is increases rapidly in order to achieve better agreement with the firn air measurements from NEEM and Summit measurements. Despite the rapid fluctuations in the reconstruction, there is still poor agreement between the modeled and measured depth profiles (Figures 3.20b-d). Modeled H_2 levels at NEEM and Summit are biased low by as much as 30 ppb in the lock-in zone. Modeled H_2 levels at Tunu are biased high by as much as 20 ppb. We do not consider this joint reconstruction to be meaningful because of the confounding effects of the offset.

We conducted a second joint reconstruction in which we accounted for the apparent offset (Figure 3.21). We introduced another free parameter, γ , which is a dimensionless scalar multiplier for the data from Tunu. γ is drawn from a uniform prior between .9 and 1.1. Equation 3.14 is adapted for the measurements from Tunu.

$$\gamma \boldsymbol{h_{obs}} \sim N(\boldsymbol{G m_{atm}}, \boldsymbol{\sigma}) \tag{3.15}$$

The posterior distribution for γ is approximately normally distributed around 1.069 with a standard deviation of 0.012, implying an offset of about 6.9% for the Tunu measurements. The results of this joint reconstruction are more realistic than the previous joint reconstruction. Atmospheric H_2 levels increase from 390 ppb in 1930 to 545 ppb in 1990 at an average rate of 2.6 ppb y^{-1}. After 1990, atmospheric H_2 starts to decrease at an average rate of 1.4 ppb y^{-1}, reaching 515 ppb in 2013. The reconstruction is in reasonable agreement with the NOAA/GML

flask measurements and the agreement between the modeled and measured depth profiles is much improved compared to the first joint reconstruction.

Interpretation of the Greenland reconstructions is complicated by the aforementioned offset in H_2 levels between Tunu and the other sites. The Tunu reconstruction shows trends that are nearly identical to the NEEM reconstruction, but with absolute H_2 levels that are 20-30 ppb lower than the NEEM reconstruction (Figure 3.19a). The difference is further illustrated by the previously discussed results of the joint reconstruction (Figure 3.20). The origin of this offset is not clear. Given that the NOAA calibration scale was revised in 1996, when the Tunu measurements were made, and the known difficulties associated with maintaining a stable H_2 calibration, the simplest explanation is a calibration problem. It is notable that the H_2 mixing ratio in the working standard, which NOAA/GML used to calibrate the Tunu measurements, was revised upward by 6.4% in 1996. Revising the Tunu measurements upward by 6.4% yields a reconstruction in near perfect agreement with the NEEM reconstruction. Furthermore, the probability model suggests that adjusting the Tunu measurements upwards by 6.9% yields the best agreement between the three sites, in good agreement with the 6.4% calibration adjustment. Re-examination of the original NOAA laboratory notes indicates that the upward revision to the working standard was applied to the Tunu measurements (Andrew Crotwell, Personal Communication). So, although a calibration offset is the most logical explanation for the differences observed, it cannot be proven as the cause.

An additional challenge in interpreting the differences between Greenland sites is the lack of reliable modern flack measurements with which to compare the reconstructions. Spatial variability in H_2 levels is much larger in the high northern latitudes than the high southern latitudes because of the presence of the large soil sink in the high northern latitudes. The best

temporal coverage for flask measurements in the high northern latitudes is from the Barrow, Alaska and Alert, Canada sampling sites. However, both sites sample the boundary layer and are influenced by their proximity to active soils. Greenland H_2 levels are more reflective of the free troposphere due to its higher elevation and remoteness from the soils. The offset between Greenland H_2 levels and high northern latitude boundary layer sites also varies dramatically in time. The difference in annually averaged H_2 levels between NOAA/GML flask measurements from Barrow, Alaska and Summit Greenland, from 1998-2005 when measurements from both sites are available, varies between 3 and 17 ppb with an average of 11 ppb. The difference between Alert, Canada and Summit, Greenland during the same period varies between 5 and 25 ppb with an average of 17 ppb. Atmospheric chemistry models produce an offset in surface H_2 levels between Summit and Barrow in good agreement with the flasks (~10 ppb). Model results underestimate the difference between Summit and Alert by a factor of 2 (Paulot et al., 2021). The high variability in the measured difference between Summit and Barrow or Alert and the lack of model-measurement agreement makes direct comparisons between our firn air histories and flask measurements from those sites difficult. Further research into the spatial variability of surface H_2 levels in the high northern latitudes is warranted.

NOAA/GML has published flask measurements from Summit, Greenland from 1998-2007. Those measurements were corrected to the MPI09 calibration scale and are plotted in figures 3.17a and 3.18a. Reconstructed H_2 levels from NEEM and Summit are in approximate agreement with those flask measurements. Unlike the firn air reconstructions, there is no discernible decreasing trend in the flask measurements during this period.

It is possible that differences between the Greenland reconstructions could be explained by *in situ* H_2 production due to the photolysis of carbonyl containing organics such as

formaldehyde. Photochemical production of formaldehyde has been observed previously in the Arctic snowpack (Sumner & Shepson, 1999) and *in situ* CO production has been invoked to explain anomalously high levels in firn air from Devon Island in the Arctic (Clark et al., 2007). H_2 is often co-produced with CO via the photolysis of carbonyls (equation 1.1a). However, there is no evidence to suggest that the observed production at Devon Island occurs at other sites. Petrenko et al. (2013) concluded that *in situ* CO production at NEEM is not significant. Furthermore, *in situ* H_2 production would likely affect Tunu more than other sites because annual accumulation is lower at Tunu, and firn air is advected downward more slowly. Clearly, this is not the case, as measured firn air H_2 levels are lower at Tunu than at Summit or NEEM.

It is challenging to explain the enrichment of trace gases in the firn with depth. The typical *e-folding* depth for actinic flux in the snowpack is 5-25 cm, so photochemistry below the top few meters of the firn is negligible (Grannas et al., 2007). Photochemical production of trace gases in the upper few meters of the firn would not affect trace gas levels deeper in the firn because of strong convective mixing at the surface. Forward model runs using *ad hoc* production rates suggest that resolving the observed discrepancies would require production rates to be 4-5 times higher at NEEM than at Tunu. Such large discrepancies in production rates seem unrealistic. Further investigation of *in situ* H_2 production would require field studies and is beyond the scope of this dissertation.

The maximum in atmospheric H_2 near 1990 is a consistent feature of the reconstructions from all three sites. These results suggest that the inferred peak from Petrenko et al. (2013) is not an artifact of ignoring pore close-off fractionation but a robust feature of Greenland firn air H_2 reconstructions. The inclusion of the pore close-off fractionation in our firn air model yields a maximum that is similar in timing and shape to Petrenko et al.'s reconstruction using the LGGE-

GISPA firn air model, but similar in absolute magnitude to Petrenko et al.'s reconstruction using the INSTAAR firn air model (Figures 3.19a and 3.21a).

The maximum around 1990 is interesting for two reasons. First, the Antarctic firn reconstructions do not show a similar maximum. H_2 is reasonably well mixed between the northern and southern hemispheres, with an atmospheric lifetime of 2 years, so a maximum in the northern hemisphere and a continued monotonic increase in the southern hemisphere is surprising. Second, high northern latitude flask measurements do not support a monotonic downward trend in H_2 from 1990-2013, as is inferred from the firn air reconstructions. Unfortunately, the temporal coverage from the Summit, Greenland flasks does not extend to 1990. As mentioned previously, surface flask measurements from most high northern latitude sites are not directly comparable to surface H_2 levels over Greenland because of the influence of the soil microbial sink on boundary layer H_2 levels. Nonetheless we would expect similar long-term trends in the surface flasks and in H_2 levels over Greenland. Flask measurements from Barrow, Alaska (Khalil & Rasmussen and NOAA/GML) and Alert, Canada (CSIRO) are plotted in Figure 3.22. The measurements from NOAA/GML from 1992-2005 were corrected to the MPI09 using the previously mentioned matched flask intercomparison project. Data from NOAA/GML is not available after 2005, and we do not have information about the NOAA/GML calibration prior to 1992. Additionally, we have no information about how the calibration of Khalil & Rasmussen compares to the modern MPI09 calibration scale.

The data from Khalil & Rasmussen (1991) show an increase in atmospheric H_2 of 2.1 ppb y^{-1} from 1985-1989. The data from NOAA/GML show a rapid decrease in atmospheric H_2 from 1989-1993, at a rate of 5.0 ppb y^{-1}. From 1993-2013, there is no discernible trend in atmospheric H_2. The combination of the two data sets implies a maximum in atmospheric H_2 in 1989, in good

agreement with the firn air reconstruction. However, the reconstructions show a longer, slower decrease in atmospheric H_2 compared to the rapid decrease and subsequent stabilization shown in the flask measurements. The implied maximum in the flask measurements should be interpreted with caution because of low confidence in the calibration from 1985-1992.

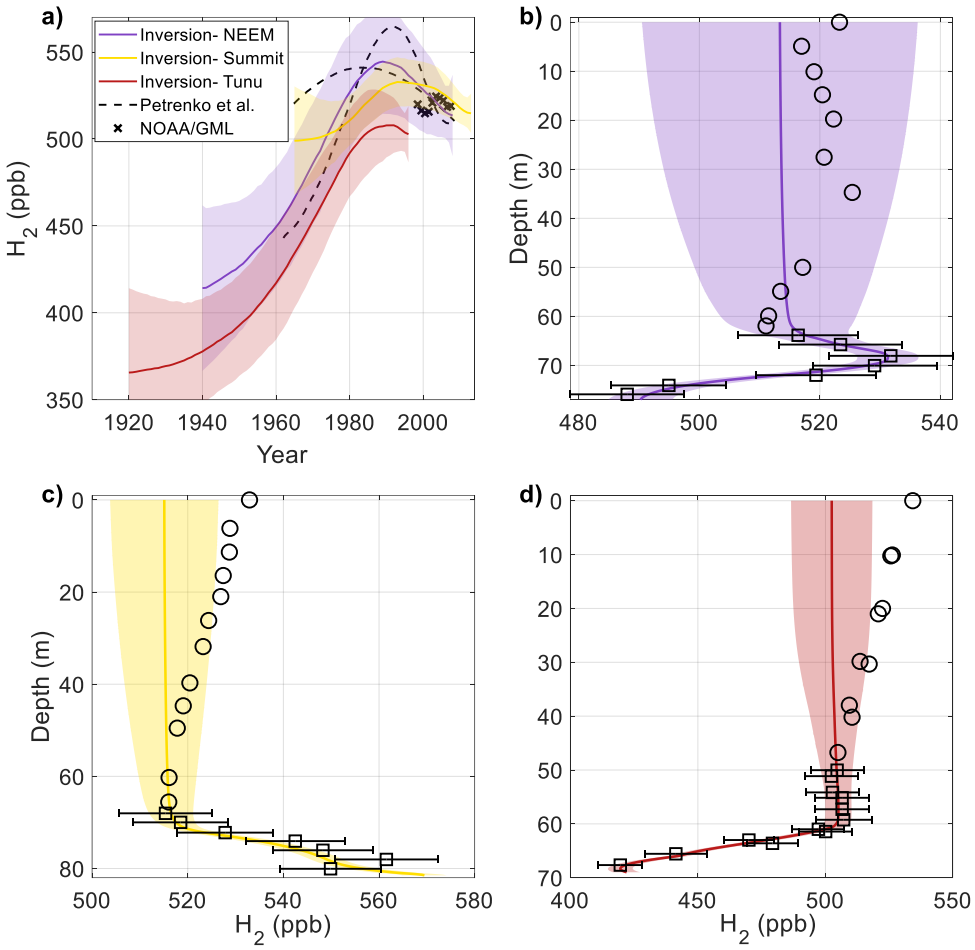

Figure 3.19- Firn air reconstructions from three Greenland sites and associated depth profiles. a) purple line and shading- result from NEEM and associated ±1σ uncertainty; yellow line and shading- result from Summit and associated ±1σ uncertainty; dark red line and shading- result from Tunu and associated ±1σ uncertainty; dashed black lines- reconstructions from NEEM from Petrenko et al. (2013) using the LGGE-GISPA firn air model and the INSTAAR firn air model; black x's– observed atmospheric H_2 annual means from Summit, Greenland from 1997-2006 (Novelli, 2006); b) black markers- measured H_2 depth profile at NEEM as in Figure 3.5c; squares with error bars are measurements used in the reconstruction, and circles are measurements excluded from the reconstruction because of seasonality ; purple line and shading- modeled depth profile using the atmospheric history plotted in purple in a) with the propagated ±1σ uncertainty; c) and d) as in b) for Summit and Tunu respectively

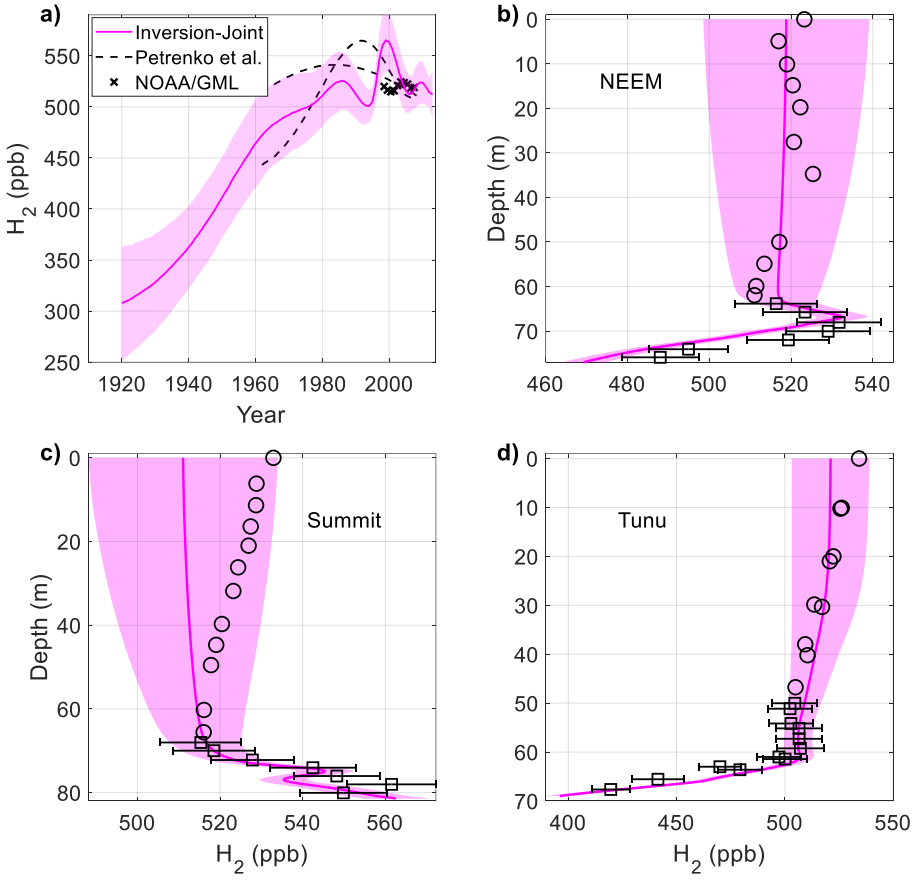

Figure 3.20- Joint atmospheric H_2 reconstruction using firn air from three Greenland sites and associated depth profiles. The joint atmospheric reconstruction is dramatically affected by an apparent offset between the measurements from Tunu and the other sites. There is poor agreement between the modeled and measured depth profiles a) magenta line and shading- result from the joint reconstruction and associated ±1σ uncertainty; dashed black lines- reconstructions from NEEM from Petrenko et al. (2013) using the LGGE-GISPA firn air model and the INSTAAR firn air model; black x's– observed atmospheric H_2 annual means from Summit, Greenland from 1997-2006 (Novelli, 2006); b) black markers- measured H_2 depth profile at NEEM as in Figure 3.19b; magenta line and shading- modeled depth profile using the atmospheric history plotted in magenta in a) with the propagated ±1σ uncertainty; c) and d) as in b) for Summit and Tunu respectively

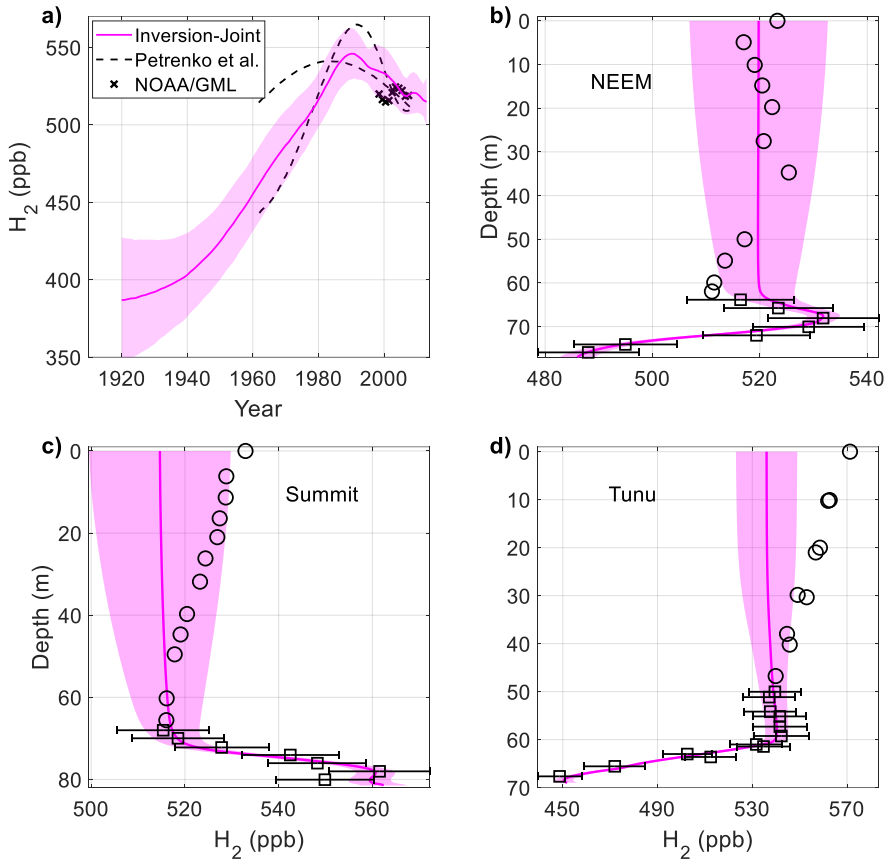

Figure 3.21- Joint atmospheric H_2 reconstruction using firn air from three Greenland sites and associated depth profiles. The reconstruction was conducted using equation 3.15 instead of equation 3.14 for the Tunu data (see text). All lines and markers are the same as in Figure 3.20. The Tunu measurements are adjusted upwards by 6.9% (see text).

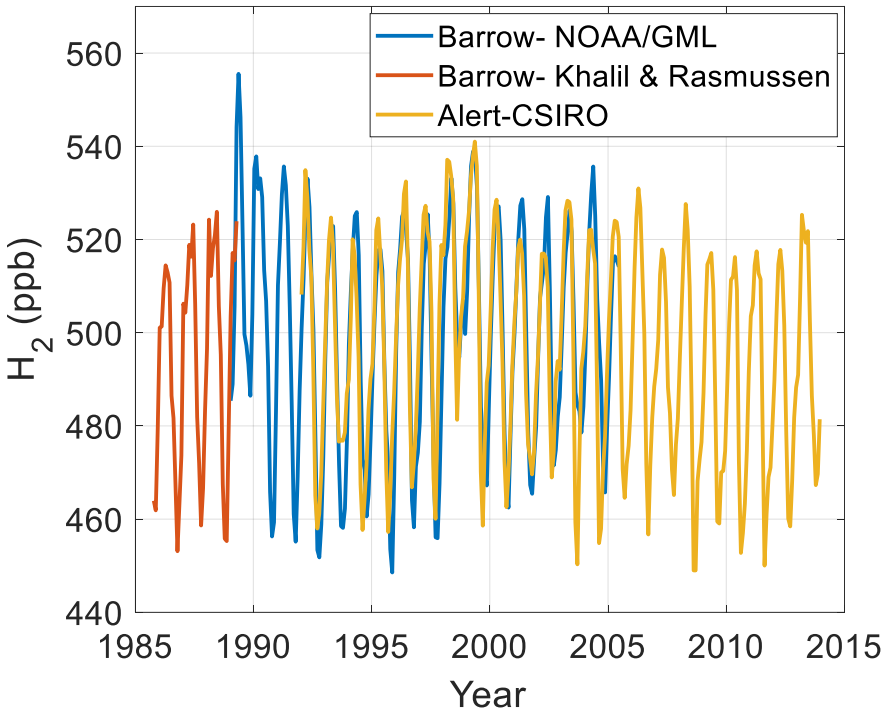

Figure 3.22- Surface flask measurements of atmospheric H_2 at high northern latitude sites. Blue line- measurements from Barrow, Alaska made by NOAA/GML and corrected to the MPI09 calibration scale (Novelli, 2006); orange line- measurements from Barrow, Alaska made by Khalil & Rasmussen (1990); yellow line- measurements from Alert, Canada made by CSIRO (Langenfelds et al., 2002). The measurements suggest a maximum in atmospheric H_2 in 1989 and a subsequent decline until 1993. Annually averaged atmospheric H_2 levels are nearly constant from 1993-2013.

3.6.2 Assessing bias in the atmospheric reconstruction- Greenland

A similar assessment of bias in the atmospheric reconstructions from Greenland firn air was carried out (Section 3.5.2). We compared firn air reconstructions of CH_4 and CO_2 to the well-established atmospheric histories of those gases. The established histories are based on Law Dome ice core measurements, adjusted to the northern hemisphere, and high northern latitude NOAA/GML flask measurements as described in Buizert et al. (2012). CH_4 age distributions were corrected to optimize the fit between modeled and measured CH_4 levels. At NEEM, the maximum bias is for the measurement at a depth of 77.5 m. The age distribution is biased young

by 3 years or 4.5% of the calculated mean CH_4 age at that depth. At Summit, the maximum bias is at a depth of 74.1 m. The age distribution is biased young by 6 years or 29.7% of the mean CH_4 age at that depth. And at Tunu, the maximum bias is at a depth of 67.7 m, where the age distribution is biased young by 14 years or 19.8% of the mean CH_4 age.

CH_4 reconstructions were conducted using both the original and corrected age distributions with the Stan technique (Figure 3.23). For the NEEM-based reconstructions, using corrected age distributions only marginally improves agreement with the established history because the original age distributions agree well with the established history. The original age distributions produce an R^2 of .994 and an RMSE Of 19.0 ppb between the reconstruction and the established history. The corrected age distributions slightly improve the R^2 to .998 and the RMSE to 9.9 ppb. For the other sites and the joint reconstruction, using the corrected age distributions substantially improves agreement between the inferred histories and the established history (Table 3.4)

We then applied the CH_4-based correction to reconstructions of CO_2. Corrections to the CH_4 age distributions were mapped onto the CO_2 age distributions as described in Section 3.5.2. Firn air reconstructions using both the original, model calculated age distributions and the corrected age distributions were compared to the established histories (Figure 3.24). Applying the CH_4-based corrections to the CO_2 age distributions improved the agreement between the firn air reconstructions and the established history for the Summit, Tunu, and joint reconstructions. R^2 values increased from .978, .875, and .973 to .981, .949, and .977 for Summit, Tunu, and the joint reconstructions respectively (Table 3.4). For NEEM, using corrected age distributions worsens the fit between the firn air reconstruction and the established history. The R^2 value decreases from .982 to .964 and the RMSE value increases from 3.1 ppm to 4.4 ppm. The CH_4-

based corrections for NEEM were very small because of the good fit between the reconstruction and the established history using the original age distributions. Evidently, the small corrections applied to the age distributions are not generalizable to other gases at this site. Nonetheless, the good agreement (R^2>.95) between the joint CH_4 and CO_2 reconstructions and the established histories using both original and corrected age distributions furnishes increased confidence in our atmospheric reconstructions.

The CH_4 based corrections were applied to the H_2 distributions and the corrected age distributions were used to reconstruct atmospheric H_2 (Figure 3.25). The corrected NEEM reconstruction is identical to the original reconstruction. The earliest parts of the Summit reconstruction are shifted higher by about 5 ppb. The maximum in atmospheric H_2 is shifted higher by about 4 ppb and earlier by 2 years to 1991. The corrected and original reconstructions converge around 2004. The Tunu record is shifted higher by about 15 ppb in 1930. The corrected reconstruction rises more slowly than the original reconstruction and reaches a maximum in 1993, two years later than the original. The maximum for the corrected reconstruction is 4 ppb higher than the maximum in the original. After 1993, the corrected reconstruction shows a decrease that is similar to the decrease in the original reconstruction. It is notable that the original CO_2 and CH_4 reconstructions for Tunu show an erroneous local maximum near 1990. The erroneous maximums are removed by the CH_4-based correction (Figure 3.23a and b; Figure 3.24a and b). The inferred maximum in H_2 is not removed by the CH_4-based correction. Instead, it is shifted younger and higher. The corrected joint reconstruction was carried out using equation 3.15 for Tunu. The joint reconstruction is higher than the original by 17 ppb in 1930. The original and corrected reconstructions converge before 1960. The differences between the

two reconstructions after 1960 are negligible. These results suggest that the effects of model-bias on the original reconstructions are small.

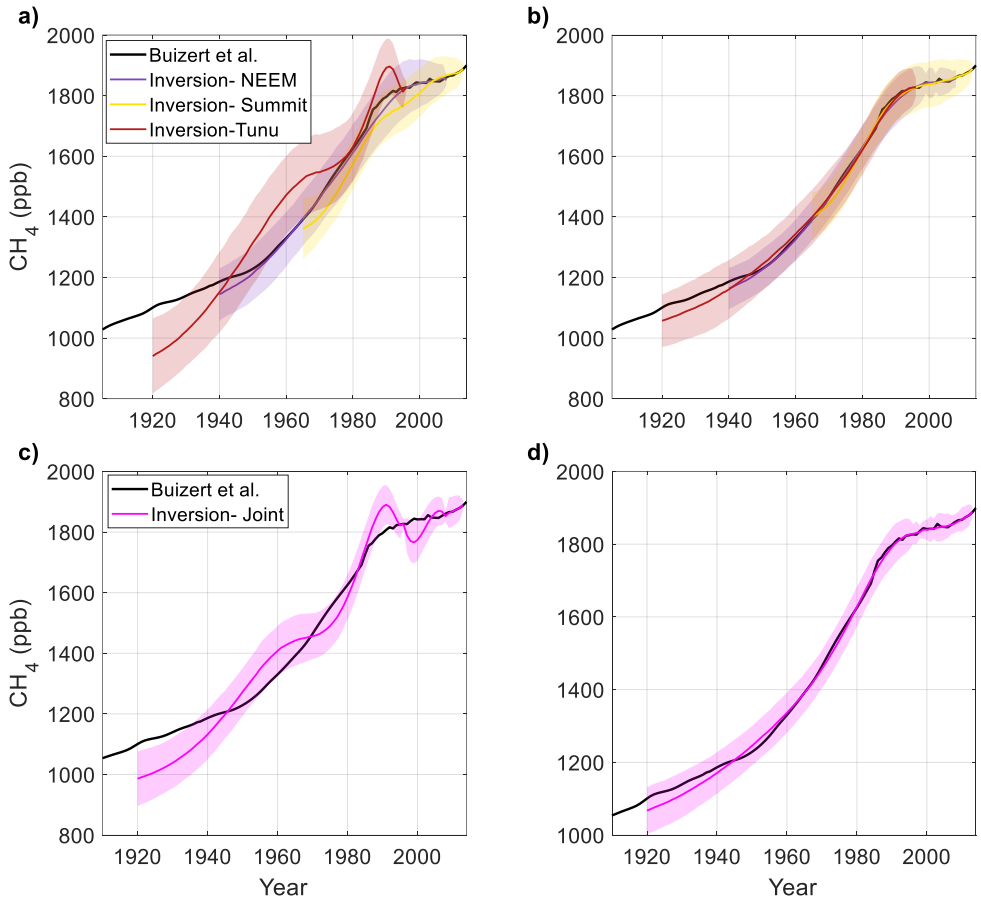

Figure 3.23- Reconstructions of northern hemisphere atmospheric CH_4 using original and corrected age distributions a) purple line and shading- reconstruction from NEEM firn air using original age distributions with the ±1σ uncertainty; yellow line and shading- reconstruction from Summit using original age distributions with the ±1σ uncertainty; dark red line and shading- reconstruction from Tunu using original age distributions with the ±1σ uncertainty; black line- established atmospheric history of CH_4 from Buizert et al. (2012). b) as in a) using corrected age distributions. c) magenta line and shading- joint reconstruction and ±1σ uncertainty using the original age distributions; d) magenta line and shading- joint reconstruction and ±1σ uncertainty using the corrected age distribution

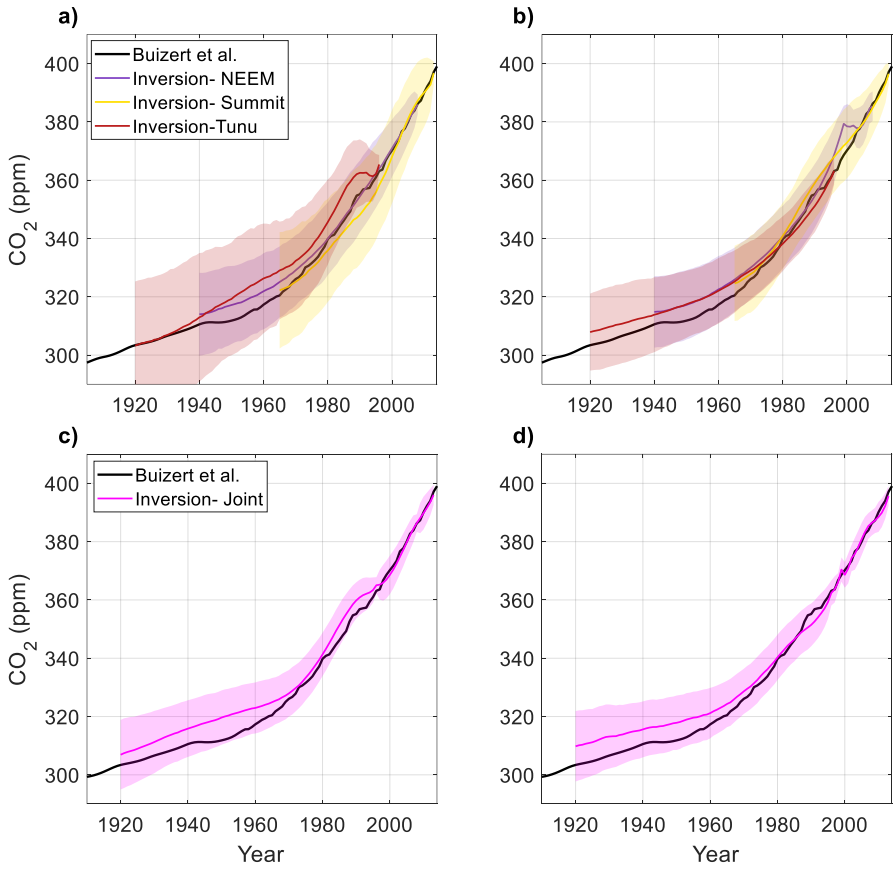

Figure 3.24- Reconstructions of northern hemisphere atmospheric CO_2 using original age distributions and age distributions with the CH_4 based correction applied. a) purple line and shading- reconstruction from NEEM firn air using original age distributions with the ±1σ uncertainty; yellow line and shading- reconstruction from Summit using original age distributions with the ±1σ uncertainty; dark red line and shading- reconstruction from Tunu using original age distributions with the ±1σ uncertainty; black line- established atmospheric history of CH_4 from Buizert et al. (2012). b) as in a) using the corrected age distributions. c) magenta line and shading- joint reconstruction and ±1σ uncertainty using the original age distributions; d) magenta line and shading- joint reconstruction and ±1σ uncertainty using the corrected age distribution

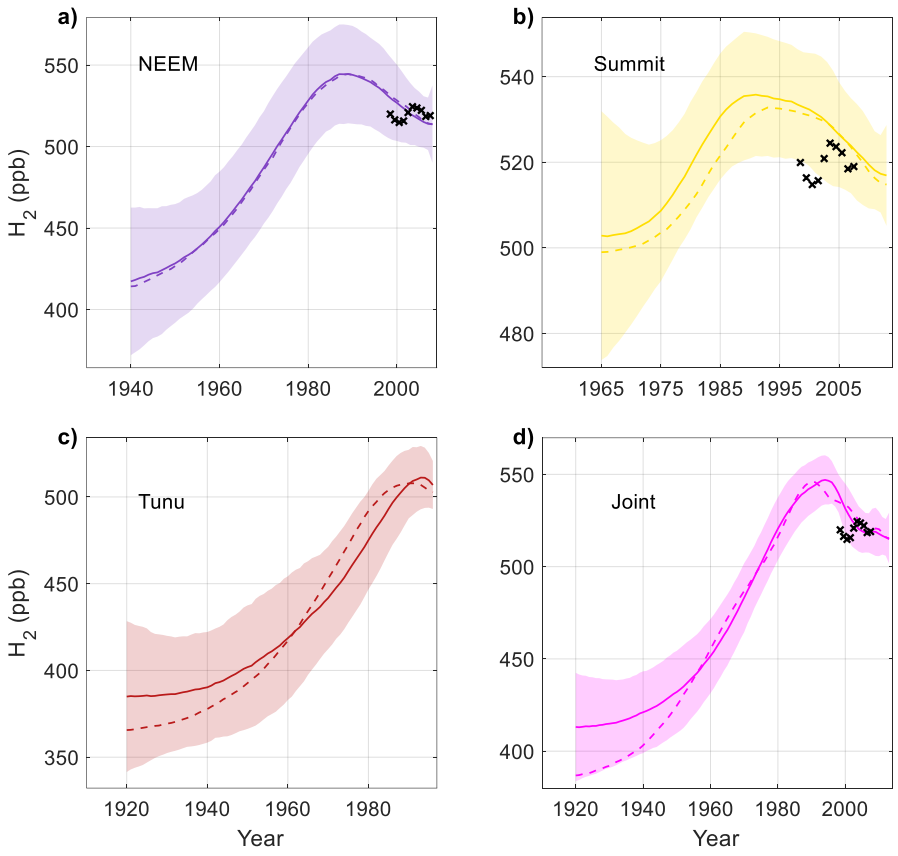

Figure 3.25- Comparison of northern hemisphere atmospheric H_2 reconstructions using original age distributions and age distributions with the CH_4-based corrections applied. a) dashed purple line- NEEM reconstruction using the original age distributions; purple line and shading- NEEM reconstruction using corrected age distributions with the ±1σ uncertainty; black x's– observed atmospheric H_2 annual means from Summit, Greenland from 1997-2006 (Novelli, 2006); b), c), and c)- as in a) for the Summit, Tunu, and joint reconstructions respectively

Table 3.4- R^2 and RMSE values for reconstructions compared to established atmospheric histories using original age distributions and corrected age distributions were calculated for CH_4 and CO_2.

Gas	Original								Corrected							
	NEEM		Summit		Tunu		Joint		NEEM		Summit		Tunu		Joint	
	R^2	RMSE	R^2	RMSE	R^2	RMSE	R^2	RMSE	R^2	RMSE	R^2	RMSE	R^2	RMSE	R^2	RMSE
CH_4	0.994	19.0 ppb	0.902	49.1 ppb	0.844	93.9 ppb	0.951	62.5 ppb	0.998	9.9 ppb	0.994	12.5 ppb	0.991	22.3 ppb	0.997	15.4 ppb
CO_2	0.982	3.1 ppm	0.978	3.3 ppm	0.875	6.1 ppm	0.973	4.5 ppm	0.964	4.4 ppm	0.981	3.1 ppm	0.949	3.9 ppm	0.977	4.2 ppm

3.7 Summary and conclusions

Atmospheric H_2 was reconstructed using firn air measurements from two Antarctic sites and three Greenland sites. H_2 levels over Antarctica were approximately constant at 330-340 ppb from 1850 to 1900. After 1900, southern hemisphere atmospheric H_2 rose, reaching 545-550 ppb at the beginning of the 21st century. Independent reconstructions from the two sites show good agreement with each other and with available surface flask measurements. Bias in the firn air reconstructions was estimated by comparing firn air reconstructions of CH_4, CO_2, and CH_3CCl_3 to the well-established atmospheric history of those gases. Those results suggest that any bias in the reconstructions falls well within the stated uncertainty of the reconstructions.

The atmospheric reconstructions from the Greenland sites are more challenging to interpret. The Greenland firn air is younger because of different site physical characteristics, and atmospheric H_2 levels could only be constrained as far back as 1930. All reconstructions display a maximum in atmospheric H_2 between 1990 and 1994, indicating that the maximum is likely a feature of the real atmospheric history. The maximum is not a modeling artifact of related to pore close-off fractionation as posited by Petrenko et al. (2013) and Patterson et al. (2021). The results from Tunu show an offset of 6-7% from the data at the other sites. This likely reflects a calibration offset, but there is no direct evidence with which to confirm this. Our best estimate is that H_2 levels over Greenland increased from about 400 ppb in 1930 to a maximum of about 545 ppb between 1990 and 1994. Thereafter, H_2 levels decreased to about 515 ppb in 2013.

The late 20th century northern hemisphere maximum inferred from the firn air records is surprising because a decreasing trend is not evident in high northern latitude surface flask measurements during the 1990's. Combining flask data from multiple laboratories implies an atmospheric maximum in 1989 and rapid decrease from 1990-1993, but a lack of inter-laboratory

calibration renders this trend uncertain. Antarctic firn air reconstructions and flask measurements show a monotonic increase in H_2 levels during the 1990's, with no evidence of a peak during the early 1990's. As discussed in Chapter 4, it is surprising to see such different trends in the two hemispheres given that H_2 has a 2-year atmospheric lifetime, and the interhemispheric transport time is about 1 year.

Another surprising result of the firn air reconstructions is the implication that the modern interpolar difference in H_2 is a relatively recent phenomenon. Both flask air and firn air measurements indicate that Antarctic H_2 levels have exceeded those over Greenland by 20-30 ppb ($\Delta_{ipd}H_2$; Antarctica-Greenland) for the past two decades. Between 1930 and 1990, however, the firn results indicate $\Delta_{ipd}H_2$ averaging about -27 ppb with the northern hemispheric levels exceeding those in the southern hemisphere. One would expect northern hemisphere H_2 to have been lower than southern hemisphere H_2 throughout the 20th century because of the extreme asymmetry of the soil-microbial sink, which accounts for about ~70% of total H_2 losses. Chapter 4 explores possible explanations for the inferred trends in the two hemispheres.

CHAPTER 4

Synthesis of northern hemisphere and southern hemisphere atmospheric H_2 reconstructions

4.1 Overview

In this chapter, we use a simple atmospheric box model to explore the implications of the firn air reconstructions for changes to the biogeochemical cycling of H_2 over the last century. The box model is described, and its performance is evaluated. The model is run for the last century and the sensitivity of H_2 levels to changes in sources and sinks is assessed. We also discuss the possibility of unaccounted for bias in the Greenland reconstructions.

4.2 Introduction

The atmospheric reconstructions in Chapter 3 show H_2 levels over Antarctica increasing by ~60% from 1900-1998 and H_2 levels over Greenland increasing by ~40% from 1930-1993. Here we use a simple 6-box model of the atmosphere and published estimates of H_2 sources and sinks to investigate what changes to the biogeochemical cycle of H_2 could have caused the atmospheric increase. The performance of the 6-box model is evaluated by comparing it to output from a modern chemical transport model and to modern flask measurements. The box model is run for the years 1900-2014, and the output is compared to the firn air reconstructions.

Two interesting aspects of the firn air reconstructions are investigated in more detail. The Greenland firn air reconstruction shows an atmospheric maximum in the early 1990's and a decrease in H_2 levels thereafter. The Antarctic reconstruction shows H_2 levels increasing until 1998. The apparent divergence in hemispheric trends during the 1990's is surprising because of the 2-year lifetime of atmospheric H_2. The box model is used to investigate the changes in the

biogeochemical cycle that could cause opposite trends in H_2 levels over Greenland and Antarctica.

The firn air reconstructions also show higher H_2 levels over Greenland than over Antarctica from 1930-1993 ($\Delta_{ipd}H_2 \approx$ -27 ppb). This is surprising because the major sink of H_2, processing by soil microbes, is concentrated in the northern hemisphere. Additionally, atmospheric flask measurements since the 1980's show that H_2 levels in the high northern latitudes were lower than H_2 levels in the high southern latitudes ($\Delta_{ipd}H_2 \approx$ 25 ppb). We explore whether a reversal in the sign of the $\Delta_{ipd}H_2$ could be explained by uncertainty in the strength or distribution of sources or sinks of H_2, and we investigate whether the surprisingly high reconstructed H_2 levels over Greenland could be caused by bias in the firn air reconstruction.

4.3 Atmospheric box modeling

The atmospheric box model is a simplified simulation of the biogeochemical cycling of H_2. The box model is fast and computationally inexpensive, making it a useful tool for sensitivity studies. There are two primary limitations of the box model. Atmospheric transport is 1-dimensional and highly simplified, and the box model cannot capture spatial gradients caused by proximity to sources or sinks. A recent 3-dimensional chemical transport model such as GFDL-AM4.1 does not have these same limitations (Paulot et al., 2021). We compare output from the box model to output GFDL-AM4.1 model to evaluate the limitations of the box model, and the box model is used to conduct sensitivity studies.

4.3.1 6-box model overview

A simple tropospheric box model of the H_2 budget is used to simulate the biogeochemical cycle of H_2. The model consists of six 30^o-wide zonal boxes, with transport based on the modern atmospheric distribution of SF_6 (Marik, 1998). H_2 sources are composed of anthropogenic H_2

emissions (including direct emissions from fossil fuel burning and oxidation of anthropogenic NMHCs), biomass burning emissions, oxidation of CH_4, oxidation of biogenic NMHCs, and terrestrial and marine N_2 fixation. The model includes first-order losses of H_2 to soils, photochemistry, and oceans. The "base-case" budget used to force the model is based primarily on a chemical transport modeling experiment using the GFDL-AM4.1 model (Paulot et al. 2021 and references therein). The model was run for the years 1995-2014 in that experiment. A detailed description of the strength and distribution of each source and sink is given in section 4.3.2. The model is run at a temporal resolution of ~1 day (360 timesteps y^{-1}) with a forward Euler time-stepping scheme. Realistic seasonal cycles are imposed for atmospheric transport, biomass burning emissions, CH_4 oxidation, the soil sink, and the photochemical sink (Marik, 1998; Paulot et al., 2021).

A minor difference between this and previous models is the inclusion of a dynamic treatment of the oceans. Because the oceans are both a source and sink of H_2, each atmospheric box is coupled to an underlying surface ocean box. The ocean box has a constant oceanic production rate and first order losses within the water column to simulate microbial cycling and downward advection (Butler, 1994; Supporting Information). The oceanic source was based on a total ocean H_2 production of 11 Tg/yr based on the global marine N_2 fixation of 150 Tg/yr and 1:1 molar stoichiometry (Brock & Madigan, 1991; Deutsch et al., 2007; Price et al., 2007). A spatially uniform loss rate constant for the surface ocean is assumed (Punshon et al., 2007) and gas transfer velocities estimated using the COAREG model modified for H_2 (Fairall et al., 2011). Although surface ocean H_2 observations are sparse, this parameterization captures the basic latitudinal pattern of surface ocean saturation state, with supersaturation in warm waters and undersaturation at high latitudes (Herr et al., 1981, 1984; Scranton et al., 1982, 1984).

4.3.2 Detailed description of sources and sinks

Sources

CH_4 oxidation: Time-dependent atmospheric CH_4 concentration is prescribed from Dlugokencky & Lan (2020b) and Etheridge et al. (1998). The average monthly OH concentration and tropospheric temperature for each latitudinal box is computed from the output of a 20-year run of the GFDL-AM4.1 model (Paulot et al., 2021). The temperature dependent rate constant of the reaction of OH with CH_4 is calculated from Burkholder et al. (2015). Latitude-dependent tH_2 yields from the oxidation of CH_4 by OH are from Novelli et al. (1999).

Anthropogenic H_2: This source includes only direct anthropogenic emissions of H_2 (not oxidation of anthropogenic NMHCs). The time-varying strength and distribution of the anthropogenic H_2 source is prescribed as in Paulot et al. (2021). Source specific H_2/CO emissions ratios were applied to CO emissions from the Community Emissions Data System v2017-05-18 to calculate total anthropogenic emissions (Ehhalt & Rohrer, 2009; Hoesly et al., 2016; Vollmer et al., 2012). There is no seasonal variability in the anthropogenic emissions term.

Biomass burning: The time-varying distribution and strength of biomass burning H_2 emissions are prescribed from the gridded data set of Van Marle et al. (2017). The data set is used at monthly resolution.

Anthropogenic NMHC oxidation: The magnitude of this time-varying source is estimated by subtracting the calculated CH_4 oxidation source from the total photochemical production of Paulot et al. (2021) for the year 2014. The remaining photochemical source is partitioned

between biogenic NMHC and anthropogenic NMHC oxidation using Ehhalt & Rohrer (2009). The source is assumed to scale in time with total anthropogenic NMHC emissions. For the 1970-2013 period, the source is scaled with the historical inventory of Huang et al., (2017). For the years prior to 1970, the source is scaled with the historical inventory of Lamarque et al. (2010). The latitudinal distribution of the source is prescribed from Huang et al., (2017).

Biogenic NMHC oxidation: The magnitude of this source is estimated by subtracting the calculated CH_4 oxidation source from the total photochemical production of Paulot et al. (2021) for the year 2014. The remaining photochemical source is partitioned between biogenic NMHC and anthropogenic NMHC oxidation using Ehhalt & Rohrer (2009). The source is assumed to be constant in time, and there is no seasonal variability. The distribution of the source is tuned to yield the same distribution of total photochemical H_2 production as in Paulot et al. (2021).

N_2 fixation-oceans: Total production of H_2 in the surface ocean is estimated using global marine N_2 fixation of 150 Tg y^{-1} and 1:1 molar stoichiometry (Brock & Madigan, 1991; Price et al., 2007). It is distributed according to Deutsch et al. (2007). Ocean-atmosphere exchange is parameterized using the method of Butler (1994). The H_2 loss constant is assumed to be uniform in each box, and it is tuned to yield the same ocean-atmosphere flux as Paulot et al. (2021) in 2014. The transfer velocity is dependent on temperature, salinity, wind speed, and, humidity for each box and is calculated from Fairall et al. (2011). The ocean model includes latitude-dependent mixed layer depths. All parameters, except for atmospheric H_2 concentration, are held constant throughout the model run.

N_2 fixation-terrestrial: H_2 emissions from terrestrial biological N_2 fixation are prescribed. For the year 2014, the emissions of Paulot et al. (2021) are used. For other years, emissions are assumed to scale with historical biological N_2 fixation from Fowler et al. (2013). The emissions are geographically distributed using the gridded estimates of NPP from the MODIS satellite (Running et al., 2015).

Sinks

Soil microbial respiration: The soil microbial sink is assumed to be first order. The rate constant and distribution are calculated from the 20-year run of GFDL-AM4.1 using the Ehhalt_MC parameterization in Paulot et al. (2021). Monthly average loss rates are used for the years prior to 1995. Actual loss rates from the model run are used for the years 1995-2014.

OH oxidation: The average monthly OH concentration and average tropospheric temperature for each latitudinal box is computed from the output of a 20-year run of the GFDL-AM4.1 model (Paulot et al., 2021). The temperature dependent rate constant of the oxidation of H_2 by OH is calculated from Burkholder et al. (2015).

4.4 Box model evaluation

Output from the box model for the years 1995-2014 was compared to output from the 20-year run of the GFDL-AM4.1 model and flask measurements from Summit, Greenland, Alert, Canada, and South Pole, Antarctica (Figures 4.1-4.3; Paulot et al., 2021; Novelli, 2006; Langenfelds et al., 2002). The annually averaged H_2 mixing ratio in the 60^o-90^o N box is biased low relative to the GFDL-AM4.1 output from Summit by ~ 20 ppb and low relative to the

calibration corrected NOAA/GML flask measurements by 10-30 ppb (Figure 4.2a). The wintertime maxima in H_2 levels are similar, but the box model overestimates the magnitude of the seasonal cycle, with substantially lower summer minima (Figures 4.1a, 4.3a). The box model and GFDL-AM4.1 output show similar long-term trends in annually averaged H_2 levels. Both models show a 15 ppb increase in H_2 levels over Summit in 1998, due to the strong ENSO event and associated biomass burning emissions. H_2 levels in both models decrease by about 25 ppb between 1998 and 2010. The flask measurements do not show the same trends. NOAA/GML first measured H_2 over Summit at the end of 1997, so the ENSO associated peak is not visible in the flask measurements. Unlike the box model and GFDL-AM4.1, there is no long-term trend visible in the flask measurements between 1998 and 2007, the last year that flask measurements are available. The flask measurements from Summit should be interpreted with caution because of the uncertainty in the NOAA96 calibration scale.

A similar comparison was conducted for H_2 levels over Alert, Canada. CSIRO has continuously monitored H_2 over Alert since 1992, and their measurements are reliably calibrated on the MPI09 scale. The high northern latitude box is biased low relative to the GFDL-AM4.1 model output by ~10 ppb (Figure 4.2b). Interestingly, the box model output agrees very well with the CSIRO flask measurements from Alert. Observed seasonal cycles at Alert are nearly identical in the box model, GFDL-AM4.1, and the flask measurements (Figure 4.2c). The magnitude of the 1998 ENSO maximum is similar in the box model and the flask measurements (Figure 4.2b). However, the box model produces H_2 levels that decrease gradually from the ENSO maximum until 2010. In contrast, the flask measurements show a rapid ~20 ppb decrease between 1998 and 2001, followed by a much slower decrease until 2010.

For South Pole, H_2 levels in the 60°-90°S box are biased high by 5-20 ppb relative to the GFDL-AM4.1 output and the CSIRO flask measurements. The annual maxima in H_2 levels are similar, but the box model substantially underestimates the seasonal cycle at South Pole, with much higher annual minima (Figures 4.1c and 4.3c). The 1998 ENSO peaks from the box model and the GFDL-AM4.1 are both ~15 ppb (Figure 4.2b), compared to ~10 ppb in the flask measurements. There is no discernible trend in H_2 levels in the models or flask measurements from 2002-2012. The models show a small decrease in H_2 levels from 2012-2014, while the flask measurements show a small increase during that time frame.

The differences between the box model and the GFDL-AM4.1 model primarily reflect spatial gradients in H_2 levels and disparities in the representation of transport. The box model calculates average tropospheric concentrations across 30° latitudinal bands. The averaged values may not be directly comparable to surface H_2 levels from the three sites. Spatial gradients in H_2 levels caused by proximity to sources and sinks are not captured by the box model. Additionally, the simplistic representation of transport in the box model may bias the distribution of atmospheric H_2, with more H_2 in the Southern hemisphere and less in the Northern hemisphere. The more complex 3-dimensonal chemical transport model, GFDL-AM4.1, shows significantly less bias relative to the flask measurements.

Despite the more accurate simulation of absolute H_2 levels, the GFDL-AM4.1 model does not confer a substantial advantage in reproducing long-term trends in atmospheric H_2 over the box model. Trends produced by the box model and GFDL-AM4.1 are nearly identical at all three sites. The model-generated trends show good agreement with the more reliable flask measurements at Alert and South Pole. The magnitude of the 1998 ENSO spike is similar in the box model, GFDL-AM4.1, and the flask measurements at Alert and South Pole. In future studies,

we could conduct our sensitivity studies using GFDL-AM4.1 or similar 3-dimensional chemical transport model, but the computational overhead precludes this for now. The box model generates the same long trends as the more complex chemical transport model, and it is readily available for these sensitivity studies.

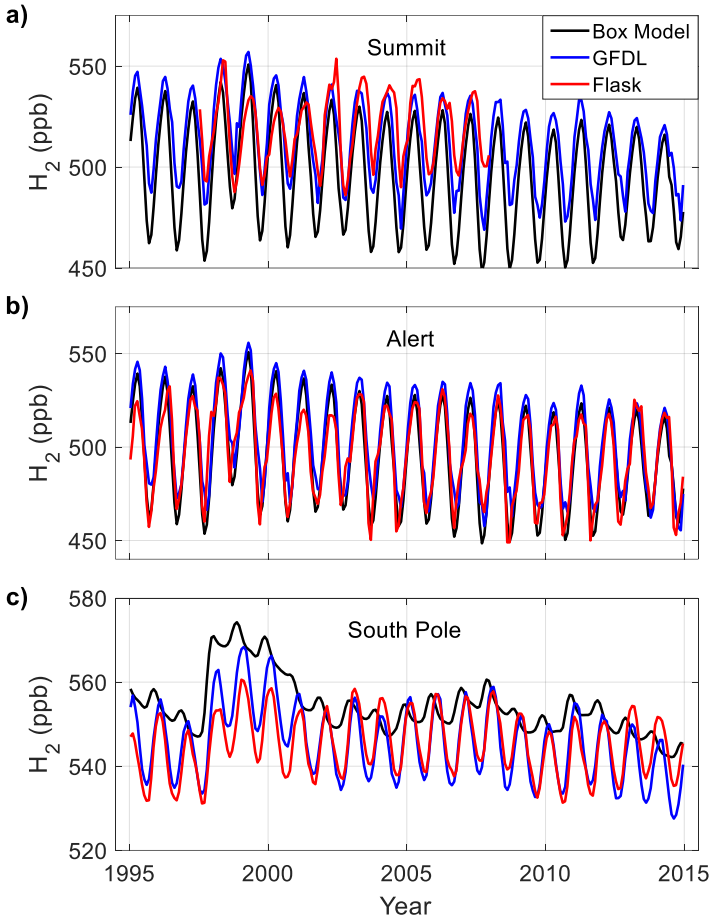

Figure 4.1- Comparison of monthly atmospheric H_2 levels from 1995-2014 generated by the box model (black lines), GFDL-AM4.1 (blue lines), and flask measurements (red lines) at a) Summit Greenland; b) Alert, Canada; and c) South Pole, Antarctica (Paulot et al., 2021; Novelli, 2006; Langenfelds et al., 2002).

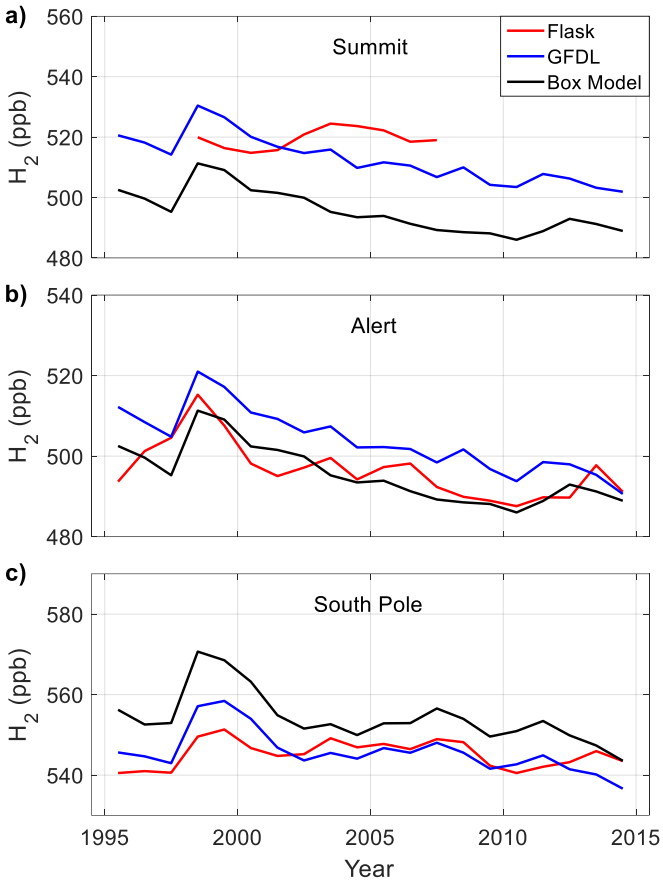

Figure 4.2- Comparison of annually averaged atmospheric H_2 levels from 1995-2014 at a) Summit, Greenland; b) Alert, Canada; and c) South Pole, Antarctica. Black lines, blue lines, and red lines are as in Figure 4.1(Paulot et al., 2021; Novelli, 2006; Langenfelds et al., 2002).

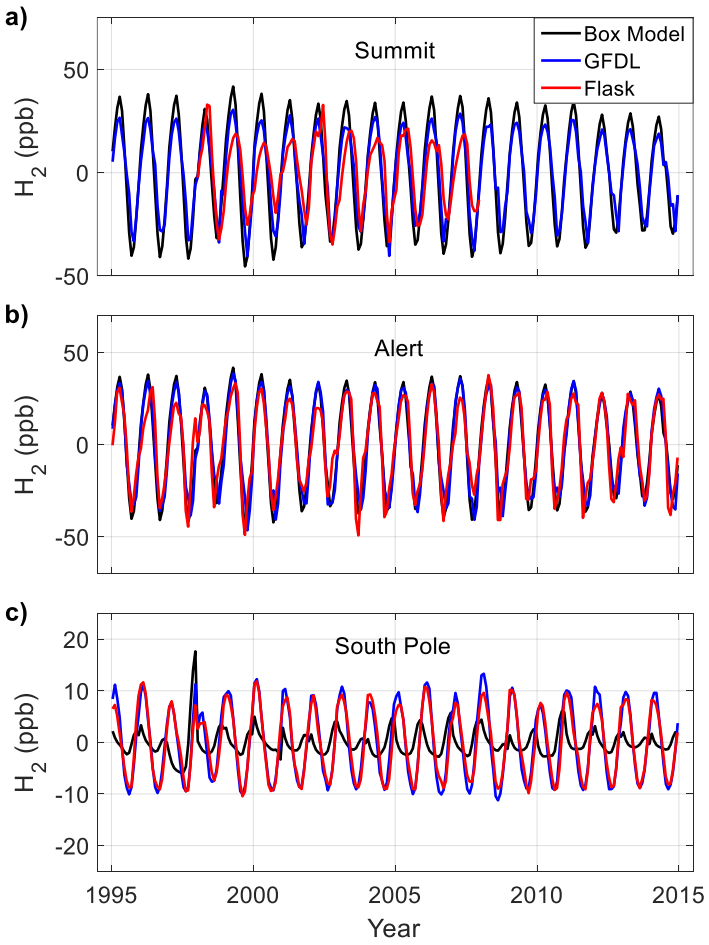

Figure 4.3- Monthly seasonal cycles computed from the monthly H_2 levels in Figure 4.1 and annually averaged H_2 levels in Figure 4.2 at a) Summit, Greenland; b) Alert, Canada; and c) South Pole, Antarctica. Black lines, blue lines, and red lines are as in Figure 4.1 (Paulot et al., 2021; Novelli, 2006; Langenfelds et al., 2002).

4.5 20th century changes to the H_2 sources

The base-case box model simulation for the years 1910-2014 was compared to the box model reconstruction (Figure 4.4). Annually averaged H_2 levels in the 60°-90° S box rise at an average rate of 1.0 ppb y^{-1} from 1910-1950, reaching 410 ppb in 1950. Then the average rate increases to 3.3 ppb y^{-1} and H_2 levels reach a maximum of 570 ppb in 1998. H_2 levels subsequently decrease to 550 ppb in 2003. The box model output is high relative to the Antarctic firn air reconstruction by an average of 14.8 ppb or 3.6% (Figure 4.4b). The smoothed annual rate of change of atmospheric H_2 from the box model is similar to that from the Antarctic firn air reconstruction. (Figure 4.4d).

Annually averaged H_2 levels in the 60-90° N box rise from 340 ppb in 1930 to 510 ppb in 1992 at an average rate of 2.6 ppb y^{-1}. H_2 levels then decrease to 495 ppb in 1997. In 1998, H_2 levels increase rapidly to a second peak at 510 ppb. Then, H_2 levels decrease at an average rate of 1.3 ppb y^{-1}, reaching 490 ppb in 2013. The box model output is biased low relative to the Greenland firn air reconstruction by an average of 46.2 ppb or 9.9%. Like the Southern hemisphere, the smoothed annual rate of change in the high northern latitude box shows good agreement with the the Greenland firn air reconstruction (Figure 4.4e).

The box model output is biased high relative to surface H_2 levels over Antarctica, and low relative to surface levels over Greenland (Section 4.4). However, the box model reliably reproduces trends observed in flask measurements from 1994-2015 (Section 4.4), and the trends in atmospheric H_2 observed in the box model and the firn air reconstructions agree well (Figure 4.4d and 4.4e). The good agreement suggests that the emissions and chemical production used to force the box model could plausibly explain changes to the H_2 levels in the firn air

reconstruction. We suspect that the biases are due to systematic 3-dimensional transport structures that are washed out in our model.

The primary drivers of changes in the H_2 levels generated by the box model are increased photochemical production from atmospheric CH_4 oxidation and changes to anthropogenic emissions. Production from CH_4 increased from 11 Tg y^{-1} in 1910 to 23 Tg y^{-1} in 2013. Direct anthropogenic emissions increase from 4 Tg y^{-1} in 1910 to a maximum of 17 Tg y^{-1} in 1989. Anthropogenic emissions decrease 14 Tg y^{-1} between 1989 and 2013. Variability in biomass burning emissions of H_2 also plays an important role in determining trends in atmospheric H_2 during the late 20th century (Section 4.6). The firn air reconstruction results from 1910-1990 are consistent with increasing production from CH_4 oxidation and changes in anthropogenic emission

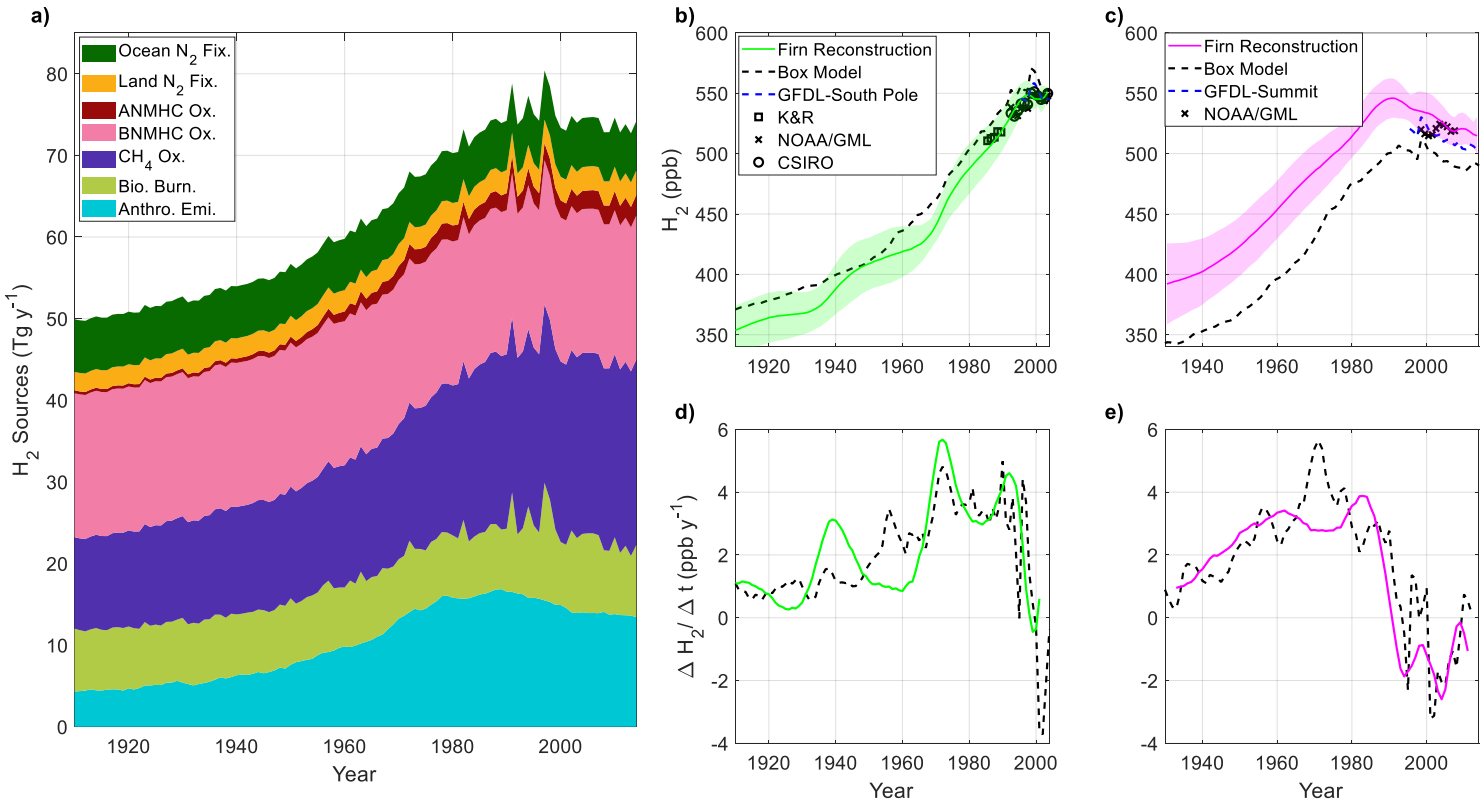

Figure 4.4- Global H_2 sources and results from the 1910-2013 base-case box model run compared to the firn air reconstruction and modern flask measurements. a) Global H_2 sources from 1910-2013 from the atmospheric box model (see text); b) green line and shading, black squares, black x's, and black circles – as in Figure 3.13a; dashed black line- annually averaged output from the 60°-90° S box of the atmospheric box model; dashed blue line-results from the 20-year run of the GFDL-AM4.1 model over the South Pole (Paulot et al. 2021); c)- magenta line and shading and black x's- as in Figure 3.20a; dashed black line- annually averaged output from the 60°-90° N box of the atmospheric box model; dashed blue line-results from the 20-year run of the GFDL-AM4.1 model over Summit, Greenland (Paulot et al. 2021); d)- annual change in atmospheric H_2 levels with a 5-year moving average filter applied for the high southern latitude box (dashed black line) and Antarctic firn air reconstruction (green line). e)- annual change in atmospheric H_2 levels with a 5-year moving average filter applied for the high northern latitude box (dashed black line) and Greenland firn air reconstruction (magenta line).

4.6 Late 20th century atmospheric H_2 trends

The firn air reconstructions show that H_2 levels in the northern and southern hemispheres exhibit different trends in atmospheric H_2 during the 1990's. H_2 levels increase over Antarctica, reaching a maximum in 1998, while H_2 levels over Greenland reach a maximum in 1990-1993 and slowly decrease thereafter. It was somewhat surprising to see such differences between trends in the two hemispheres given the 2-year atmospheric lifetime of H_2. However, the 1910-2014 box model simulation does a reasonable job of simulating the trends. The trends are largely accounted for by decreasing anthropogenic emissions and 3 strong biomass burning pulses of H_2 burning during the intense ENSO years of 1991-1992, 1993-1994, and 1997-1998 (Figure 4.5).

To investigate the impact of these ENSO-related emissions, a "constant burning" experiment (CB) was done with the box model. Average monthly burning emissions were calculated from the emissions inventory of Van Marle et al. (2017) for the years 1910-1989. The box model was then forced with the calculated average monthly emissions for the years 1990-2014, disregarding the ENSO emissions pulses during the 1990's. All other inputs are the identical to the base-case box model run (Section 4.5). The results were compared to the bae-case 1910-2014 box model run, which was forced using Van Marle et al. (2017) emissions for the entire run (Figure 4.6). H_2 levels in the 60^o-90^o S box plateau after 1990 in the CB run, with <3 ppb of variability throughout the decade. In contrast, H_2 levels from that box in the base-case run increase ~18 ppb from 1990-1997, with an additional 15 ppb increase from 1997-1998. The difference in H_2 levels between the base-case run and the CB run are less dramatic in the 60^o-90^o N box. In the CB run, H_2 levels decrease slightly faster and there is not a second maximum in 1998. The differences between the base-case box model run and the CB clearly illustrate the importance of the ENSO pulses in driving trends in atmospheric H_2 during the 1990's.

These findings are somewhat different from Patterson et al. (2021), in which we concluded that an additional unknown source of H_2 was needed to account for the divergent trends at the two poles. In retrospect, there were two reasons for this incorrect inference. First, Patterson et al. (2021) used the steady state solution to the box model. The steady-state model generates unrealistic fluctuations in atmospheric H_2 (up to 50 ppb y^{-1}; Figure 4.7) when forced with emissions that have strong interannual variability (such as biomass burning). To avoid those fluctuations, the steady-state box model was forced with burning emissions estimated from the CO emissions inventory of Lamarque et al. (2010). That inventory did not include ENSO-related emissions pulses and decreased during the 1990's (Figure 4.5).

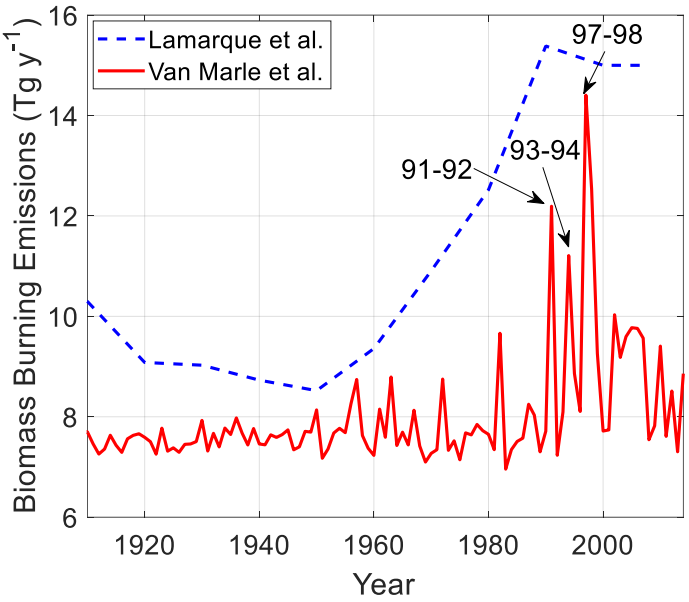

Figure 4.5- Global biomass burning emissions of H_2 from Van Marle et al. (2017; red line) and calculated from Lamarque et al. (2010) as used in Patterson et al. (2021, dashed blue line). The 1990's ENSO emissions pulses are labeled with black arrows.

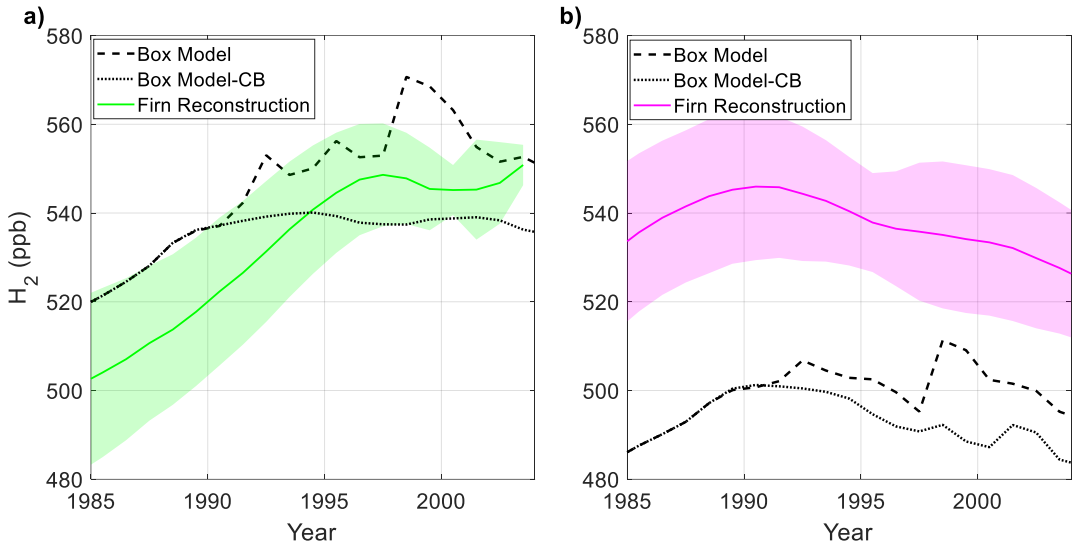

Figure 4.6- Comparison of box model output from the base-case 1910-2014 run and the CB run. a) dashed black line- annually averaged box model output from the 60°-90° S box from the base-case 1910-1914 run; dotted black line- annually averaged box model output from the 60°-90° S box from the CB run; green line and shading- joint Antarctic firn air reconstruction; b)- dashed and dotted black lines- as in (a) for the 60°-90° N box; magenta line and shading- joint Greenland firn air reconstruction

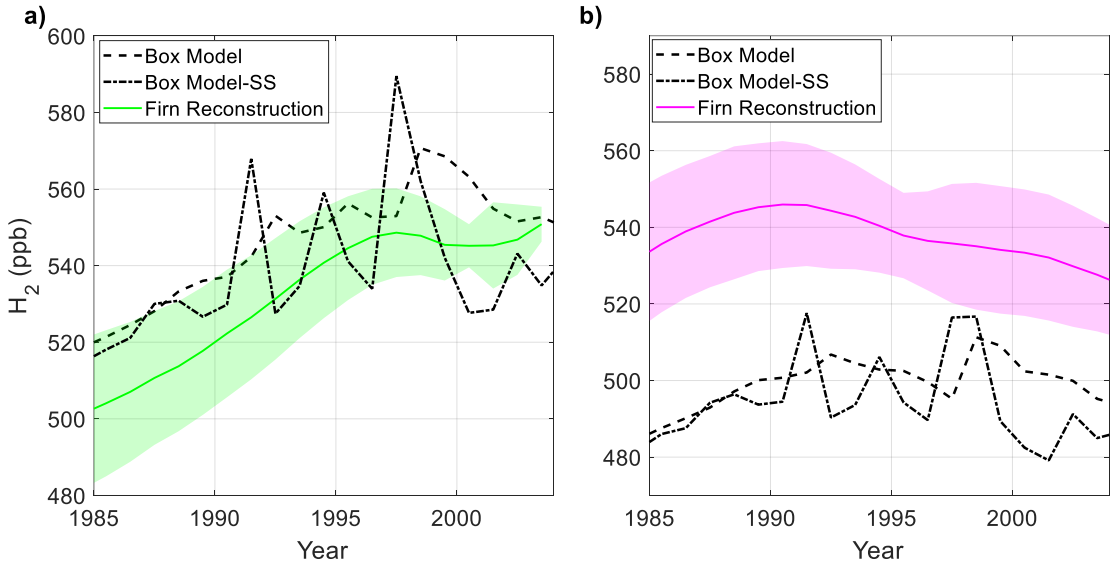

Figure 4.7- Comparison of box model output from the base-case 1910-2014 run and the steady state run. a) dashed black line- annually averaged box model output from the 60°-90° S box from the base-case 1910-1914 run; dash-dot black line- annually averaged box model output from the 60°-90° S box from the steady state run; green line and shading- joint Antarctic firn air reconstruction; b)- dashed and dash-dot black lines- as in (a) for the 60°-90° N box; magenta line and shading- joint Greenland firn air reconstruction

4.7 Comparison of atmospheric H_2 over Antarctica and Greenland

The firn air reconstructions show atmospheric H_2 levels that are ~27 ppb higher over Greenland than Antarctica from 1930-1994 (Figure 4.8). This result is surprising because: 1) atmospheric flask measurements since the 1980's that H_2 levels in the high northern latitudes were lower than H_2 levels in the high southern latitudes and 2) modern flask measurements and atmospheric modeling suggest that the extreme northern hemisphere bias of the soil-microbial sink precludes higher levels of H_2 in the high northern latitudes. In this section, we investigate whether uncertainties in the budget or bias in the firn air reconstruction could explain the reversal in the sign of the reconstructed $\Delta_{ipd}H_2$.

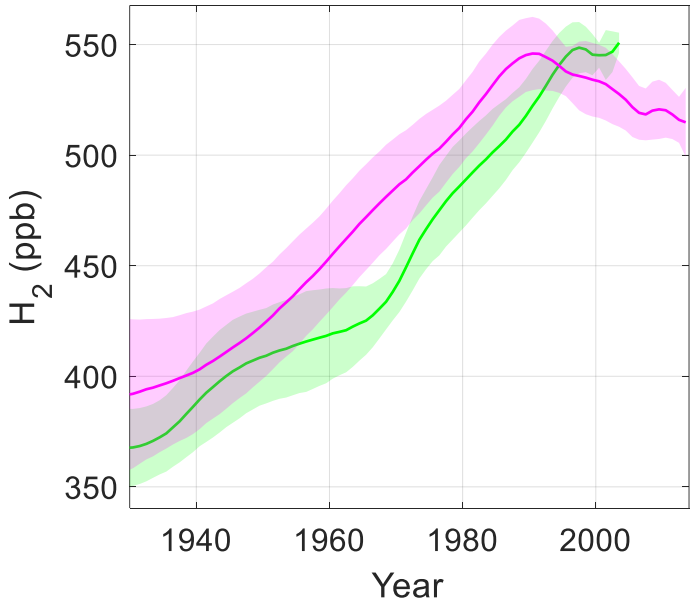

Figure 4.8- Comparison of joint firn air reconstructions from Antarctica (green line and shading) and Greenland (magenta line and shading) as in Figures 3.13 and 3.21.

4.7.1 Uncertainties in the budget?

A reversal of the $\Delta_{ipd}H_2$ implies that the distribution of sources and sinks has changed over time, or the current understanding of the distribution of sources and sinks is wrong. In this section, we investigate the magnitude of changes to sources and sinks that would be required to drive Greenland H_2 levels higher than Antarctic H_2 levels from 1930-1993.

H_2 levels over Greenland can be driven higher than Antarctic levels by changing the distribution of sources and sinks or changing the relative importance of sources and sinks with differing distributions. In the first sensitivity experiment we altered the distribution of the soil sink. In the base-case run, 4.9% of losses to soils occur in the high northern latitude box, and 29.3% occur in the southern tropical box. In this experiment, soil losses in the high northern latitude box are reduced to 0, and the soil sink in the southern tropical box is increased by the same amount, keeping the atmospheric H_2 burden approximately constant. The results show that H_2 levels in the 60^o-90^o N box are very sensitive to the change in soil sink distribution while levels in the 60^o-90^o S box are not affected (Figure 4.9). Modeled H_2 levels in the high northern latitude box are ~50 ppb higher than the base-case throughout the run. The box model output shows agreement with the Greenland reconstruction from 1930-1985. After 1985, the box model output is biased high by 15-20 ppb. The $\Delta_{ipd}H_2$ is near 0 from 1930-1950. After 1950, high northern latitude levels surpass high southern latitude levels and remain higher until 2006. After 2006, output from the two high latitude boxes is very similar. The pattern of the $\Delta_{ipd}H_2$ is similar to the firn air reconstructions, with the change of sign coming somewhat later.

We conducted a second experiment with a modified soil sink distribution. In this experiment, the soil sink in the high northern latitudes is reduced to half of its base-case strength.

Again, the strength of the soil sink in the southern tropical box increases by the same amount. Output from the 60°-90° N box is halfway between the base case and the previous experiment (Figure 4.10). The box model output is 30 ppb lower than the Greenland firn air reconstruction in 1930. By 1990, the bias between the box model and the firn reconstruction is reduced to ~10 ppb. The box model output in the 60°-90° S is not affected by the perturbation and shows reasonable agreement with the Antarctic firn air reconstruction throughout the model run. The $\Delta_{ipd}H_2$ is 25 ppb in 1930 and declines to near 0 ppb by 1970. Between 1970 and 1993, H_2 levels in the high latitude boxes remain similar. After 1993, the $\Delta_{ipd}H_2$ grows to ~25 ppb.

We also conducted an experiment in which the distribution of the soil sink was varied in time. The strength of the soil sink in the 60°-90° N box is reduced to 0 from 1910-1960. Then, the soil sink in that box is linearly ramped to half of its strength in the base-case from 1961-2014. The reduction in the strength of the soil sink in the high northern latitude box is balanced by a corresponding increase in the southern tropical soil sink throughout the model run. The box model output from this run show agreement with both firn air reconstructions throughout the model run (Figure 4.11). Output from the high latitude boxes is approximately equal from 1930-1950. After 1950, high northern latitude levels are higher than high southern latitude levels until 1992. After 1992, the sign of the $\Delta_{ipd}H_2$ reverses with high southern latitude H_2 levels higher than high northern latitude levels. The $\Delta_{ipd}H_2$ pattern in this box model run is very similar to the pattern in the firn air reconstructions.

We conducted a similar experiment with the box model in which source strengths were varied instead of the distribution of the soil sink. In the box model, 92% of anthropogenic emissions are in the northern hemisphere, while only 56% of production from CH_4 occurs in the northern hemisphere. H_2 levels in the 60°-90° N box can be driven higher by increasing the

importance of anthropogenic emissions relative to production from CH_4. The box model was run with anthropogenic emissions scaled higher by 75%. The change was balanced by reducing production from CH_4 by 46%, keeping the total tropospheric burden of H_2 approximately constant. The results show that H_2 in the high northern latitude box is lower than in the high southern latitude box from 1930-1970 (Figure 4.12). After 1992, the sign of the $\Delta_{ipd}H_2$ reverses with high northern latitude H_2 levels higher than high southern latitude levels. After 1990, H_2 in the high northern latitude box decreases below H_2 in the high southern latitude box. The box model output is biased 20-30 ppb low relative to the Greenland reconstruction from 1930-1980. The box model and the Greenland reconstruction show reasonable agreement from 1980-2013. The box model and the Antarctic reconstruction are in agreement from 1930-1960. The box model is biased high relative to the Antarctic reconstruction thereafter.

Modifying the anthropogenic and CH_4 oxidation source to achieve better agreement during the earlier parts of the reconstruction would require increasing anthropogenic emissions by a factor of >10 because of the low anthropogenic emissions during this period. The atmospheric levels produced by such a large change to the anthropogenic source are not realistic, and those results are not included here. The sensitivity experiments in this section demonstrate that H_2 levels in the high northern latitudes are very sensitive to the distribution of the soil sink. Adjusting the distribution of <5% of the soil sink increases H_2 levels in the 60^o-90^o N box by as much as 50 ppb and produces a $\Delta_{ipd}H_2$ that is very similar to the firn air reconstructions. H_2 levels in the high northern latitude box are also very sensitive to anthropogenic emissions. However, prior to 1980, there were not enough anthropogenic emissions to yield a negative $\Delta_{ipd}H_2$.

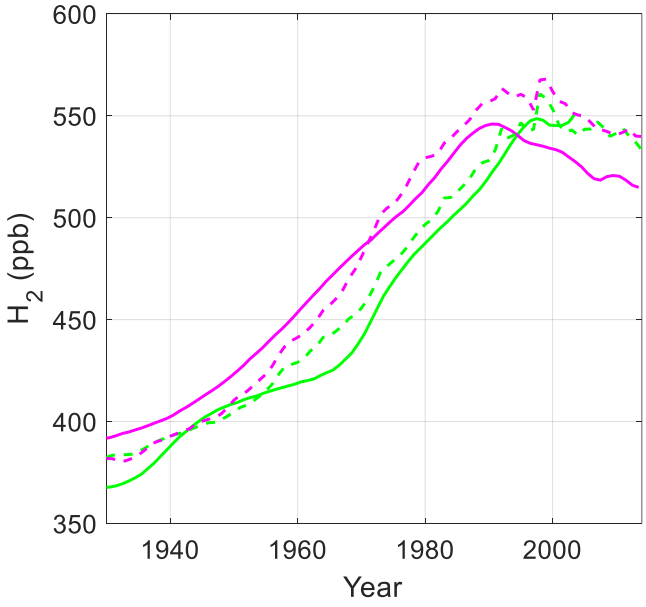

Figure 4.9- Comparison of firn air reconstructions (solid lines) with the box model run with the high northern latitude soil sink reduced to 0 and the southern tropical box soil sink increased by the corresponding amount; solid green line- joint Antarctic reconstruction as in Figure 4.8; solid magenta line- joint Greenland reconstruction as in Figure 4.8.; dashed green line- box model output from the 60º-90º S box; dashed magenta line- box model output from the 60º-90º N box

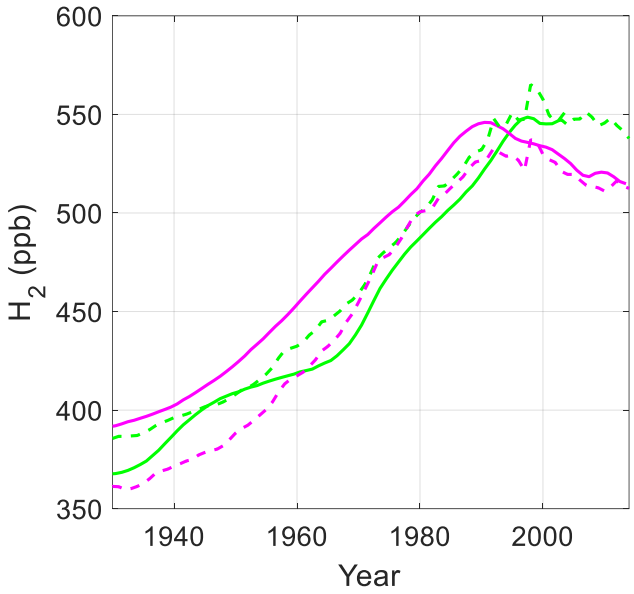

Figure 4.10- Comparison of firn air reconstructions (solid lines) with the box model run with the high northern latitude soil sink reduced to half of its base-case strength and the southern tropical box soil sink increased by the corresponding amount; solid green line- joint Antarctic reconstruction as in Figure 4.8; solid magenta line- joint Greenland reconstruction as in Figure 4.8.; dashed green line- box model output from the 60^{o}-90^{o} S box; dashed magenta line- box model output from the 60^{o}-90^{o} N box

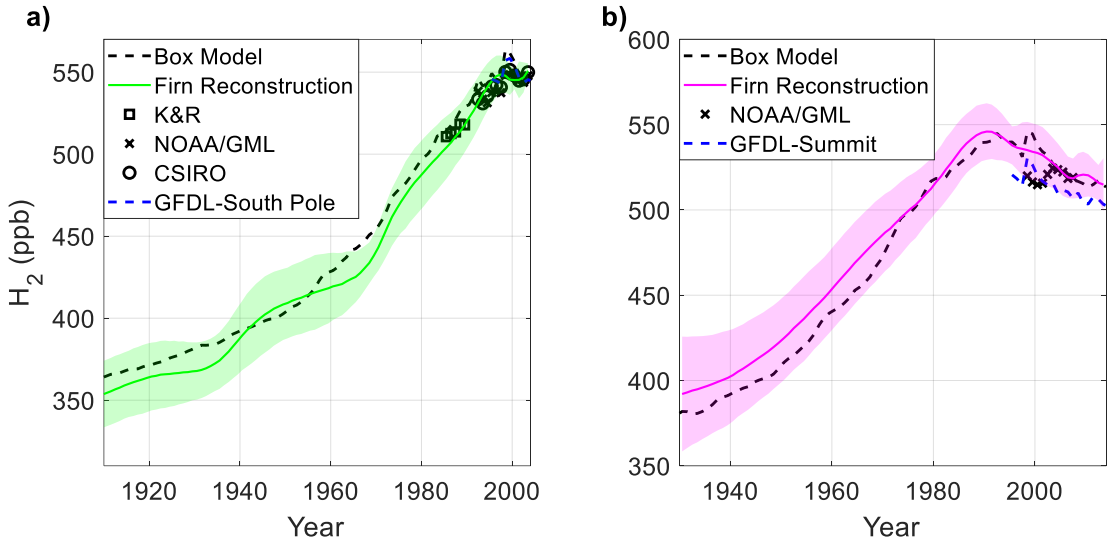

Figure 4.11- Comparison of firn air reconstructions (solid lines and shading) with the box model run with the high northern latitude soil sink ramped from 0 to half of its base-case strength as described in the text. All lines and markers are as in Figure 4.4b and 4.4c.

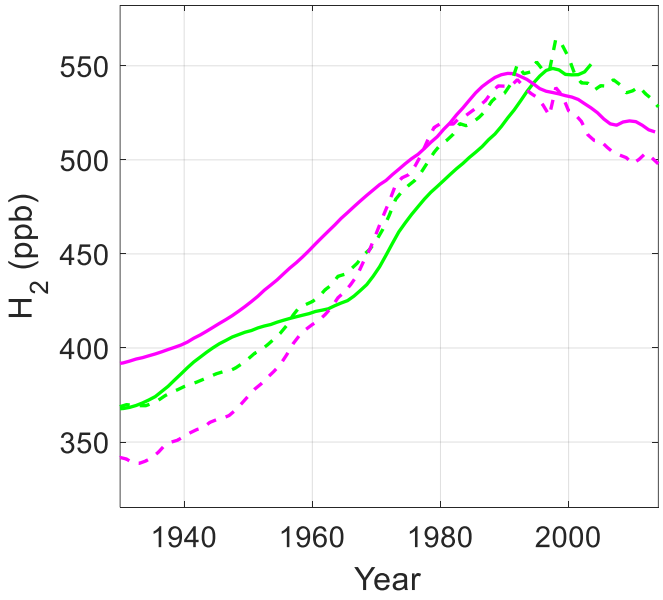

Figure 4.12- Comparison of firn air reconstructions (solid lines) with the box model run with the strength of anthropogenic emissions increased by 75% from its base-case strength and the production from CH_4 oxidation reduced by 46% from its base-case strength; solid green line- joint Antarctic reconstruction as in Figure 4.8; solid magenta line- joint Greenland reconstruction as in Figure 4.8.; dashed green line- box model output from the 60º-90º S box; dashed magenta line- box model output from the 60º-90º N box

4.7.2 Bias in the Greenland reconstruction?

We also investigated the possibility that the higher H_2 levels in the Greenland reconstruction are caused by bias. It is more likely that the Greenland reconstruction is biased than the Antarctic reconstruction. The independent reconstructions from the Antarctic sites show good agreement with each other and with available flask measurements, beginning in 1987, giving us higher confidence in the reconstructions (Figure 3.11). The independent Greenland reconstructions show some disagreement, and there are no modern flask measurements with which to compare the reconstructions prior to 1998, giving us somewhat lower confidence in the Greenland reconstructions (Figure 3.19).

Errors in the calibration of the firn air measurements could cause bias in the reconstruction. In section 3.6.1, we attributed the disagreement between the Tunu reconstruction and the Summit and NEEM reconstructions to uncertainty in the calibration of the Tunu measurements. However, the measurements from Summit and NEEM had large (>20 ppb) calibration corrections applied to them. It is possible that the measurements from those sites were over-corrected. H_2 levels from the independent Tunu reconstruction are less than or equal to H_2 levels from the Antarctic reconstruction (Figure 4.13). We conducted another joint reconstruction in which we assume that the measurements from Tunu were accurate and that the measurements from Summit and NEEM required calibration correction. Equation 3.15 was applied to the measurements from NEEM and Summit instead of the measurements from Tunu. The new joint reconstruction yields drastically reduced H_2 levels relative to the previous joint reconstruction (Figure 4.14). The posterior distributions for γ show that the Summit and NEEM measurements should be adjusted lower by 6.5% and 6.7% respectively to achieve agreement with the Tunu measurements. On average, the newer reconstruction is 31 ppb lower than the

previous reconstruction and approximately equal to reconstructed H_2 levels over Antarctica before 1993 (Figure 4.14). However, flask measurements show that the modern $\Delta_{ipd}H_2$ is 20-30 ppb (Figure 4.2). If the modern $\Delta_{ipd}H_2$ can be extrapolated in time, the calibration offset cannot fully account for unexpectedly high levels of H_2 in the Greenland reconstruction.

An unknown firn process could also bias the Greenland reconstruction. The possibility of *in situ* H_2 production is discussed in Section 3.6.1. *In situ* production would cause the firn air reconstructions to be biased high. Underestimating the enrichment associated with pore close-off fractionation could also cause the firn air reconstructions to be biased high. As mentioned previously, the partial pressure of H_2 reaches equilibrium between the closed and open pores. However, inaccurate pore close-off parameterizations could lead to an underestimate of the H_2 enrichment in the open pores. As an illustrative example, we performed another joint inversion in which we assumed the modeled enrichment is underestimated. First the enrichment (***en***) of the age distribution at each depth was calculated:

$$\boldsymbol{en} = \boldsymbol{G} - \frac{\boldsymbol{G}}{\sum_t \boldsymbol{G}} \tag{4.1}$$

Where ***en*** is a matrix of the same dimensions as ***G***. A scaling factor for the enrichment (*f*) was introduced to equations 3.14 and 3.15:

$$\boldsymbol{h_{obs}} \sim N((\boldsymbol{G} + f\boldsymbol{en})\boldsymbol{m_{atm}}, \boldsymbol{\sigma}) \tag{4.2}$$

$$\gamma\boldsymbol{h_{obs}} \sim N((\boldsymbol{G} + f\boldsymbol{en})\boldsymbol{m_{atm}}, \boldsymbol{\sigma}) \tag{4.3}$$

Where *f* is sampled from a uniform prior that is greater than or equal to 0. Equation 4.2 was used for the data from NEEM and Summit. Equation 4.3 was used for the data from Tunu.

The inversion results show substantially reduced H_2 levels during the earliest parts of the inversion (Figures 4.15 and 4.16). The means of the posterior distributions for *f* are 1.43, .24, and 1.60 for NEEM, Summit, and Tunu respectively. The *f* values correspond to scaling enrichment higher by 143%, 24%, and 160% at the three sites. The mean of the posterior distribution for γ is 1.054, implying an offset of about 5.4% for the Tunu measurements. The modeled H_2 depth profiles show good agreement with the measured depth profiles (Figure 4.15b-d). H_2 levels in the new reconstruction are 50 ppb lower than the original reconstruction in 1930 (Figure 4.16). Between 1930 and 1998, the difference between the original and new reconstruction decreases. After 1998, the difference between the two reconstructions is negligible. H_2 levels in the new reconstruction surpass levels in the Antarctic reconstruction in 1965 and remain higher until 1992. So, this reconstruction does not fully explain the surprisingly high levels of H_2 in the Greenland reconstruction relative to the Antarctic reconstruction. However, this reconstruction is meant as a simple illustrative example. It is possible that calculating and scaling enrichment differently could drive H_2 levels in the Greenland reconstruction lower than in the Antarctic reconstruction. Firn air measurements of neon and helium, which are highly diffusive noble gases, would help to further constrain the magnitude of the enrichment associated with pore close-off fractionation at these sites.

Alternatively, a so-called "seasonal rectifier effect" could cause a high bias in the Greenland reconstructions. Rectifier effects have been proposed to explain anomalous measurements of $\delta^{15}N$ and $\delta^{40}Ar$ in the firn air at South Pole and Dome Fuji (Morgan et al., 2022). For example, if convective mixing is stronger during the winter when H_2 levels are at

their annual maximum, firn air levels of H_2 could be biased towards the higher wintertime values. There is no evidence of a rectifier effect in firn air measurements of CO_2 or CH_4 at these sites (Section 3.6.2). However, H_2 is significantly more diffusive and has a stronger relative seasonal cycle than CO_2 or CH_4. So, seasonally varying convection could affect H_2 differently. The measured amplitude of the seasonal cycle at Summit is 40-50 ppb (Figure 4.3a). In the extreme case of firn air measurements reflecting only the wintertime maximum H_2 levels, our reconstructions would be biased high by ~25 ppb. The $\Delta_{ipd}H_2$ is about -27 ppb in the original reconstructions (Figure 4.8). So, a seasonal rectifier effect cannot fully explain the unexpectedly high reconstructed H_2 levels over Greenland.

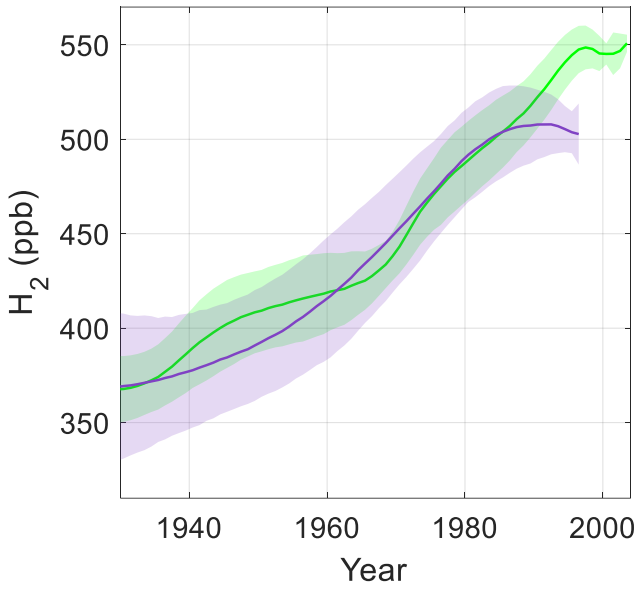

Figure 4.13- Comparison of firn air reconstructions from Antarctica (green line and shading) and Tunu (purple line and shading) as in Figures 3.13 and 3.19

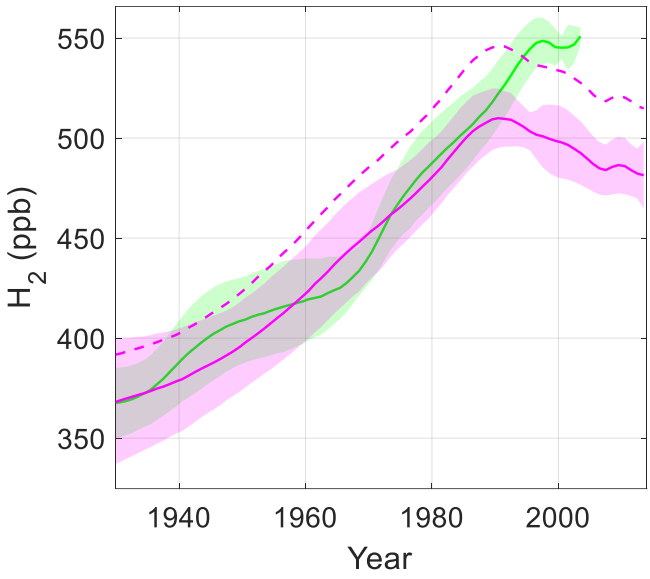

Figure 4.14- Comparison of firn air reconstructions from Antarctica (green line and shading) and Greenland (magenta lines and shading); dashed magenta line- original joint reconstruction as in Figure 4.8; solid magenta line and shading- joint reconstruction using equation 3.15 for NEEM and Summit and equation 3.14 for Tunu (see text).

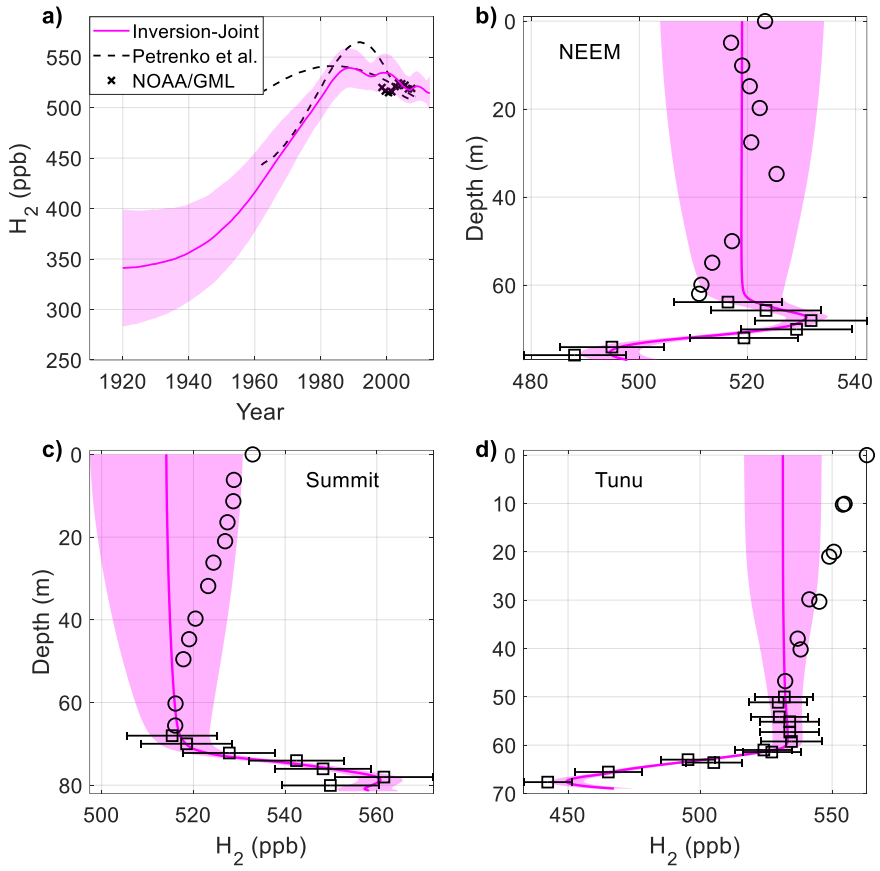

Figure 4.15- Joint atmospheric H_2 reconstruction using firn air from three Greenland sites and associated depth profiles. The reconstruction was carried out using equation 4.2 for NEEM and Summit and equation 4.3 for Tunu (see text) a) magenta line and shading- result from the joint reconstruction and associated ±1σ uncertainty; dashed black lines- reconstructions from NEEM from Petrenko et al. (2013) using the LGGE-GISPA firn air model and the INSTAAR firn air model; black x's– observed atmospheric H_2 annual means from Summit, Greenland from 1997-2006 (Novelli, 2006); b) black markers- measured H_2 depth profile at NEEM as in Figure 3.19b; magenta line and shading- modeled depth profile using the atmospheric history plotted in magenta in a) with the propagated ±1σ uncertainty; c) and d) as in (b) for Summit and Tunu respectively

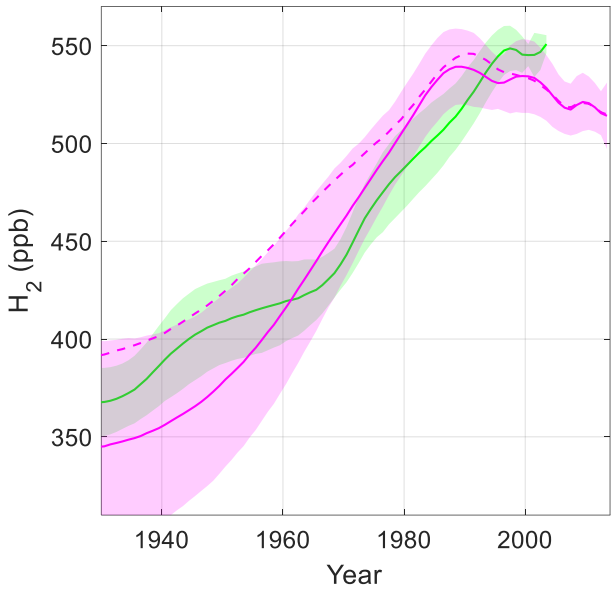

Figure 4.16- Comparison of firn air reconstructions from Antarctica (green line and shading) and Greenland (magenta lines and shading); dashed magenta line- original joint reconstruction as in figure 4.8; solid magenta line and shading- results from the joint reconstruction using equations 4.2 and 4.3 as in Figure 4.15a.

4.8 Summary and conclusions

The drivers for the changes in H_2 levels inferred from firn air were explored using an atmospheric box model. The 20th century increase in atmospheric H_2 levels is consistent with increasing anthropogenic emissions from fossil fuel burning and increasing photochemical production from the oxidation of CH_4. Surprisingly, the firn air reconstructions show that H_2 increased over Antarctica but decreased over Greenland during the 1990's. Here, we showed that the divergent trends can be explained by decreasing anthropogenic emissions combined with three large biomass burning emissions pulses that were associated with strong ENSO events. This result contradicts our previously published conclusions, which asserted that an additional unknown source of H_2 is required to explain the differing trends in the two hemispheres (Patterson et al., 2021).

The firn air reconstructions show an unexpected reversal in the sign of the $\Delta_{ipd}H_2$. It is surprising that H_2 levels would be higher over Greenland than Antarctica because of the dominant role the soil sink plays in the biogeochemical cycle of H_2. Our sensitivity experiments demonstrate that H_2 levels over Greenland are very sensitive to the distribution of the soil sink. Published parameterizations of soil sink show significant variability in their spatial distributions due to differences in dependencies on temperature, moisture, and soil carbon content (Paulot et al., 2021). The wide range in published estimates suggests that the spatial distribution of the soil sink is not well constrained. In our model, less than 5% of the total soil sink is located in the 60°-90° N box. Redistribution of the part of the soil sink that is located in the 60°-90° N box to the 0°-30° S box increases H_2 levels in high northern latitudes by 50 ppb. Ramping the strength of the soil sink in the 60°-90° N box produces a H_2 levels in good agreement with the firn air reconstruction and a similar reversal in the sign of the $\Delta_{ipd}H_2$. These modifications to the soil sink distribution are small relative to the range of published estimates. Perturbation of the anthropogenic source does not produce the same reversal in the $\Delta_{ipd}H_2$. We also considered several mechanisms that could bias the Greenland reconstruction high, causing the unexpected reversal in the $\Delta_{ipd}H_2$. It is unlikely that any single mechanism could cause a bias large enough to explain the $\Delta_{ipd}H_2$ in the firn air reconstruction, but we cannot rule out bias as a contributing factor. Further investigation of the temporal evolution of the $\Delta_{ipd}H_2$ is warranted.

CHAPTER 5

Conclusions and future directions

The major goal of this dissertation was to reconstruct changes in atmospheric H_2 over the past century and understand the likely causes of those changes. Reconstructing the atmospheric history of H_2 is useful for testing scientific theories about the biogeochemical cycling of H_2 and making informed predictions about future changes in the biogeochemical cycle in a changing climate. This work involved 1) conducting laboratory experiments to determine the permeability of H_2 in ice, 2) studying the implications of the permeability measurements for the incorporation of H_2 into polar firn and ice, 3) reconstructing the atmospheric history of H_2 using firn air measurements from Greenland and Antarctica, and 4) carrying out global biogeochemical model calculations. Progress was made towards the major goals, with some caveats. The key findings from this study and prospects for future research are discussed below.

5.1 Key findings and outstanding questions

Significant changes in atmospheric H_2 occurred over the past century. H_2 levels increased by roughly 60% over Antarctica and roughly 40% over Greenland. The Antarctic reconstructions show good agreement with each other and with available flask measurements, giving us a high degree of confidence of in that reconstruction. Confidence is somewhat lower for the Greenland reconstructions. The independent reconstructions from the three sites show some disagreement, and there are few flask measurements with which to compare. There are several mechanisms that could bias the Greenland firn air reconstructions. Further work is required to better constrain historical levels of H_2 over Greenland.

For most of the 20th century, H_2 levels were slightly higher over Greenland than Antarctica. This $\Delta_{ipd}H_2$ is reversed from the present day. The reversal is surprising because of

the dominant role the soil sink plays in the biogeochemical cycle of H_2. After 1990, trends were different in the two hemispheres, with Greenland levels decreasing and Antarctic levels increasing. It was surprising to see different trends in the two hemispheres, because the atmospheric lifetime of H_2 (2 years) is twice the interhemispheric mixing time (1 year). Model simulations suggest that the 20th century increase in atmospheric H_2 is attributable to increasing anthropogenic emissions and increasing photochemical production from CH_4. The opposite trends in the two hemispheres during the 1990's were likely caused by decreasing anthropogenic emissions combined with intense biomass burning emissions pulses associated with three strong ENSO events

Surprisingly, the reconstructions show that H_2 levels over Greenland were higher than over Antarctica until the early 1990's. After this time, H_2 was higher over Antarctica. This reversal of the sign of the interpolar difference ($\Delta_{ipd}H_2$) deserves further scientific attention, pending confirmation of the Greenland firn air history. A possible explanation for the reversal is an increase in the strength of the soil sink in the high northern latitudes. It is possible to reproduce the $\Delta_{ipd}H_2$ from the firn air reconstructions by reducing strength of the soil sink to 0 in the high northern latitudes during the early-mid 20th century and slowly increasing it during the late 20th century. Temperatures are rising more quickly in the Arctic compared to other parts of the Earth (eg. Manabe & Stouffer, 1980; Previdi et al., 2021; Serreze et al., 2009). Paulot et al. (2021) estimate a temperature dependent increase in H_2 deposition velocity of 2-4% K^{-1}. A reversal in the sign of the $\Delta_{ipd}H_2$ driven by Arctic warming implies substantially higher temperature dependence of the soil sink. The potential for bias in the Greenland reconstruction precludes us from making firm conclusions about changes to the distribution of the soil sink

without additional research. Other possible drivers of the reconstructed changes to the $\Delta_{ipd}H_2$ should be investigated in addition to the soil sink.

Another goal for this project was to use our understanding of H_2 permeability in ice to assess the potential for studying atmospheric H_2 on longer time scales using polar ice cores. It is shown that H_2 permeation is likely to result in equilibration between open and closed pores in the firn column. This equilibration causes H_2 enrichment in firn air measurements from the lock-in zone and must be taken into account in firn air analyses. It also results in loss of H_2 relative to air during air enclosure, a process that would need to be accounted for in interpreting ice core measurements. Furthermore, the rapid permeation of H_2 in polar ice leads to diffusive smoothing of vertical gradients. For ice with gas ages of several centuries, this smoothing would be on the order of decades, comparable to that caused by diffusion during firn air enclosure. On millennial time scales, this smoothing will likely preclude the reconstruction of higher frequency (decadal) variability.

The permeation measurements also have implications for the sampling of polar ice cores for H_2. The permeation of H_2 from shallow bubble-containing ice should be slow enough to permit analysis of H_2 up to a year after drilling. Deeper ice core samples with higher bubble-pressure and/or clathrates will need to be sealed in an evacuated flask or extracted immediately upon recovery to prevent diffusive losses from the supersaturated ice to the atmosphere. These findings are based on idealized models and require validation using real polar ice.

5.2 Broader context and future directions

There is growing scientific interest in understanding the processes controlling atmospheric H_2 levels. Anthropogenic perturbations to the biogeochemical cycle of H_2 are unequivocal and likely to increase as H_2 becomes a more important energy source. It is estimated

that H_2 could meet 18% of global energy demand by 2050 (Hydrogen Council, 2017). Deploying H_2 energy at this scale could be a significant step in the reduction of carbon intensity necessary to limit global warming. However, any reduction in carbon emissions is contingent on the implementation of "green hydrogen" production. Currently, the vast majority of H_2 is produced by reforming hydrocarbons, a process that emits carbon to the atmosphere (International Energy Agency, 2019). If H_2 were instead produced via the electrolysis of water using renewable energy sources, the H_2 energy sector would emit no carbon to the atmosphere. Coupling H_2 production from hydrocarbons to carbon capture technologies is another option. Deploying carbon capture at H_2 production facilities is significantly cheaper and easier than at electricity plants (Damen et al., 2006).

Approximately 2500 Tg y^{-1} of H_2 would be required to replace fossil fuel energy with energy from H_2 (Derwent et al., 2020). In the more realistic scenario of the replacement of 20% of fossil fuel energy with energy from H_2, ~500 Tg y^{-1} would be required. Estimated leakage rates range from .2-10% (Van Ruijven et al., 2011). A 5% leakage rate would yield an additional 25 Tg y^{-1} of anthropogenic H_2, a 90% increase from the estimated 2014 anthropogenic emissions and a 33% increase in total H_2 sources.

There are several promising avenues for researchers seeking to understand how such a perturbation could affect the biogeochemical cycling of H_2 in a changing climate. Anthropogenic impacts drove large changes in atmospheric H_2 over the last century. The large anthropogenic signal overwhelms any climate signal in the firn air record. Ice core measurements of H_2 would allow atmospheric reconstructions on much longer timescales. Researchers could use the longer atmospheric history to investigate the climate sensitivity of biogeochemical cycle of H_2, because large anthropogenic impacts should be limited to the industrial period. Such research is critical

for making accurate projections of how the H_2 biogeochemical cycle will respond to a warming climate. Measurements of the deuterium content of H_2 in polar firn air and ice cores could further constrain past changes to the biogeochemical cycling of H_2. Strong isotopic fractionation is associated with each source and sink of H_2, so changes in sources and sinks should produce a strong atmospheric signal (Pieterse et al, 2011; Price et al., 2007).

The soil sink is the largest single flux in the biogeochemical cycle of H_2, but there is no scientific consensus of how it varies with climate on a global scale. Significant differences exist in published parameterizations of the dependence of H_2 deposition velocity on temperature, soil moisture, and soil carbon content (Paulot et al., 2021). Projecting the response of the soil sink to changing temperature, precipitation, and land-use requires further study. Landscape-scale studies (eg. Belviso et al., 2013; Meredith et al., 2014) and laboratory-scale experiments (eg. Smith-Downey et al., 2006) would both advance understanding of the climate dependence of the soil sink. Expanding coverage across a wide range of soil types and ecosystems is of paramount importance for projecting the response of the H_2 soil sink to climate change. Better understanding of the soil sink will improve model parameterizations and allow researchers predict how the biogeochemical cycle of H_2 will respond to increasing anthropogenic emissions in a changing climate.

This dissertation has advanced understanding of H_2 cycling in the recent past. It is surprising that so little is understood about past and future changes to the biogeochemical cycle of H_2, considering its importance and abundance in the atmosphere. Anthropogenic H_2 emissions are likely to increase dramatically in the coming decades. The current moment presents a unique opportunity to conduct research to better understand the response of the H_2 biogeochemical cycle

before radical perturbations to atmospheric H_2 in a changing climate. Such research should inform decisions about the role of H_2 in future green energy systems.

BIBLIOGRAPHY

Ackermann, M., Ahrens, J., Bai, X., Bartelt, M., Barwick, S. W., Bay, R. C., et al. (2006). Optical properties of deep glacial ice at the South Pole. *Journal of Geophysical Research Atmospheres*, *111*(13), 1–26. https://doi.org/10.1029/2005JD006687

Agency, I. E. (2019). *The Future of Hydrogen*. *The Future of Hydrogen*. Paris. https://doi.org/10.1787/1e0514c4-en

Ahn, J., Headly, M., Brook, E. J., Wahlen, M., Mayewski, P. A., & Taylor, K. C. (2008). CO2 Diffusion in Polar Ice : Observations from Naturally Formed CO2 Spikes in the Siple Dome (Antarctica) Ice Core. *Journal of Glaciology*, *54*(187).

Alley, R. B. (2000). Ice-core evidence of abrupt climate changes. *Proceedings of the National Academy of Sciences of the United States of America*, *97*(4), 1331–1334. https://doi.org/10.1073/pnas.97.4.1331

Assonov, S. S., Brenninkmeijer, C. A. M., Jöckel, P., Mulvaney, R., Bernard, S., & Chappellaz, J. (2007). Evidence for a CO increase in the SH during the 20th century based on firn air samples from Berkner Island, Antarctica. *Atmospheric Chemistry and Physics*, *7*(2), 295–308. https://doi.org/10.5194/acp-7-295-2007

Aydin, M., Britten, G. L., Montzka, S. A., Buizert, C., Primeau, F., Petrenko, V., et al. (2020). Anthropogenic Impacts on Atmospheric Carbonyl Sulfide Since the 19th Century Inferred From Polar Firn Air and Ice Core Measurements. *Journal of Geophysical Research: Atmospheres*, *125*(16), 1–23. https://doi.org/10.1029/2020JD033074

Bader, H. (1964). Density of Ice as a Function of Temperature and Stress. *Special Report (U.S. Army Cold Regions Research and Engineering Laboratory)*, *64*, 1–6.

Battle, M., Bender, M., Sowers, T., Tans, P. P., Butler, J. H., Elkins, J. W., et al. (1996). Atmospheric gas concentrations over the past century measured in air from firn at the South Pole. *Nature*, *383*(6597), 231–235. https://doi.org/10.1038/383231a0

Battle, M. O., Severinghaus, J. P., Sofen, E. D., Plotkin, D., Orsi, A. J., Aydin, M., et al. (2011). Controls on the movement and composition of firn air at the West Antarctic Ice Sheet Divide. *Atmospheric Chemistry and Physics*, *11*(21), 11007–11021. https://doi.org/10.5194/acp-11-11007-2011

Belviso, S., Schmidt, M., Yver, C., Ramonet, M., Gros, V., & Launois, T. (2013). Strong similarities between night-time deposition velocities of carbonyl sulphide and molecular hydrogen inferred from semi-continuous atmospheric observations in Gif-sur-Yvette, Paris region. *Tellus B: Chemical and Physical Meteorology*, *65*(1), 20719. https://doi.org/10.3402/tellusb.v65i0.20719

Bender, M., Sowers, T., & Lipenkov, V. (1995). On the concentrations of O2, N2, and Ar in trapped gases from ice cores. *Journal of Geophysical Research*, *100*(D9).

Bereiter, B., Schwander, J., Lüthi, D., & Stocker, T. F. (2009). Change in CO2 concentration and O2/N2 ratio in ice cores due to molecular diffusion. *Geophysical Research Letters*, *36*(5), 1–5. https://doi.org/10.1029/2008GL036737

Brock, T. D., & Madigan, M. T. (1991). *Biology of microorganisms* (6th ed.). EngleWood Cliffs, NJ: Prentice-Hall.

Brook, E. J., & Buizert, C. (2018). Antarctic and global climate history viewed from ice cores. *Nature*, *558*(7709), 200–208. https://doi.org/10.1038/s41586-018-0172-5

Buizert, C., Martinerie, P., Petrenko, V. V., Severinghaus, J. P., Trudinger, C. M., Witrant, E., et al. (2012). Gas transport in firn: Multiple-tracer characterisation and model intercomparison for NEEM, Northern Greenland. *Atmospheric Chemistry and Physics*, *12*(9), 4259–4277. https://doi.org/10.5194/acp-12-4259-2012

Burkholder, J. B., Abatt, J. P. D., Huie, R. E., Kurylo, M. J., Wilmouth, D. M., Sander, S. P., et al. (2015). *Chemical Kinetics and Photochemical Data for Use in Atmospheric Studies Evaluation Number 18*. *JPL Publication 15-10*. Pasadena, CA.

Burr, A., Ballot, C., Lhuissier, P., Martinerie, P., Martin, C. L., & Philip, A. (2018). Pore morphology of polar firn around closure revealed by X-ray tomography. *Cryosphere*, *12*(7), 2481–2500. https://doi.org/10.5194/tc-12-2481-2018

Butler, J. H. (1994). The potential role of the ocean in regulating atmospheric CH3Br. *Geophysical Research Letters*, *21*(3), 185–188.

Butler, J. H., Battle, M., Bender, M. L., Montzka, S. A., Clarke, A. D., Saltzman, E. S., et al. (1999). A record of atmospheric halocarbons during the twentieth century from polar firn air. *Nature*, *399*(6738), 749–755. https://doi.org/10.1038/21586

Carpenter, B., Gelman, A., Hoffman, M. D., Lee, D., Goodrich, B., Betancourt, M., et al. (2017). Stan: A probabilistic programming language. *Journal of Statistical Software*, *76*(1). https://doi.org/10.18637/jss.v076.i01

Clark, I. D., Henderson, L., Chappellaz, J., Fisher, D., Koerner, R., Worthy, D. E. J., et al. (2007). CO2 isotopes as tracers of firn air diffusion and age in an Arctic ice cap with summer melting, Devon Island, Canada. *Journal of Geophysical Research Atmospheres*, *112*(1), 1–13. https://doi.org/10.1029/2006JD007471

Craig, H., & Chou, C. C. (1982). Helium isotopes and gases in Dye 3 ice cores. *Eos*, *63*, 298.

Crank, J. (1975). THE MATHEMATICS OF DIFFUSION.

Damen, K., Troost, M. Van, Faaij, A., & Turkenburg, W. (2006). A comparison of electricity and hydrogen production systems with CO 2 capture and storage. Part A: Review and selection of promising conversion and capture technologies. *Progress in Energy and Combustion Science*, *32*(2), 215–246. https://doi.org/10.1016/j.pecs.2005.11.005

Derwent, R. G., Stevenson, D. S., Utembe, S. R., Jenkin, M. E., Khan, A. H., & Shallcross, D. E. (2020). Global modelling studies of hydrogen and its isotopomers using STOCHEM-CRI: Likely radiative forcing consequences of a future hydrogen economy. *International Journal of Hydrogen Energy*, *45*(15), 9211–9221. https://doi.org/10.1016/j.ijhydene.2020.01.125

Deutsch, C., Sarmiento, J. L., Sigman, D. M., Gruber, N., & Dunne, J. P. (2007). Spatial coupling of nitrogen inputs and losses in the ocean. *Nature*, *445*(7124), 163–167. https://doi.org/10.1038/nature05392

Dlugokencky, E., & Lan, X. (2020a). Atmospheric Carbon Dioxide Dry Air Mole Fractions from the NOAA GML Carbon Cycle Cooperative Global Air Sampling Network, 1968-2019. Retrieved from ftp://aftp.cmdl.noaa.gov/data/trace_gases/co2/

Dlugokencky, E., & Lan, X. (2020b). Atmospheric Methane Dry Air Mole Fractions from the NOAA GML Carbon Cycle Cooperative Global Air Sampling Network, 1983-2019. Retrieved from ftp://aftp.cmdl.noaa.gov/data/trace_gases/ch4/

Ehhalt, D. H., & Rohrer, F. (2009). The tropospheric cycle of H2: A critical review. *Tellus, Series B: Chemical and Physical Meteorology*, *61*(3), 500–535. https://doi.org/10.1111/j.1600-0889.2009.00416.x

Ehhalt, D. H., Schmidt, U., & Heidt, L. E. (1977). Vertical Profiles of Molecular Hydrogen in the Troposphere and Stratosphere. *Journal of Geophysical Research*, *82*(37), 5907–5911. https://doi.org/10.1007/s11214-006-9067-0

Etheridge, D. M., Steele, L. P., Langenfelds, R. L., & Francey, R. J. (1996). Natural and anthropogenic changes in atmospheric CO 2 over the last 1000 years from air in Antarctic ice and firn. *Journal of Geophysical Research*, *101*(D2), 4115–4128. https://doi.org/10.1074/jbc.271.44.27509

Etheridge, D. M., Steele, L. P., Francey, R. J., & Langenfelds, R. L. (1998). Atmospheric methane between 1000 A.D. and present: Evidence of anthropogenic emissions and climatic variability. *Journal of Geophysical Research*, *103*(D13), 15,979-15,993.

Fairall, C. W., Yang, M., Bariteau, L., Edson, J. B., Helmig, D., McGillis, W., et al. (2011). Implementation of the Coupled Ocean-Atmosphere Response Experiment flux algorithm with CO2, dimethyl sulfide, and O3. *Journal of Geophysical Research: Oceans*, *116*(10). https://doi.org/10.1029/2010JC006884

Gow, A. J. (1971). Relaxation of ice in deep drill cores from Antarctica. *J Geophys Res*, *76*(11), 2533–2541. https://doi.org/10.1029/jb076i011p02533

Grannas, A. M., Jones, A. E., Dibb, J., Ammann, M., Anastasio, C., Beine, H. J., et al. (2007). An overview of snow photochemistry: Evidence, mechanisms and impacts. *Atmospheric Chemistry and Physics*, *7*(16), 4329–4373. https://doi.org/10.5194/acp-7-4329-2007

Haan, D. (1996). *Teneurs en monoxyde de carbone de l ' air contenu dans la glace de l ' Antarctique et du Groenland*. Universite Joseph Fourier- Grenoble 1.

Herr, F. L., Scranton, M. I., & Barger, W. R. (1981). Dissolved hydrogen in the Norwegian Sea: Mesoscale surface variability and deep-water distribution. *Deep-Sea Research*, *28A*(9), 1001–1016.

Herr, F. L., Frank, E. C., Leone, G. M., & Kennicutt, M. C. (1984). Diurnal variability of dissolved molecular hydrogen in the tropical South Atlantic Ocean. *Deep Sea Research Part A, Oceanographic Research Papers*, *31*(1), 13–20. https://doi.org/10.1016/0198-0149(84)90069-4

Hmiel, B., Petrenko, V. V., Dyonisius, M. N., Buizert, C., Smith, A. M., Place, P. F., et al. (2020). Preindustrial 14CH4 indicates greater anthropogenic fossil CH4 emissions. *Nature*, *578*(7795), 409–412. https://doi.org/10.1038/s41586-020-1991-8

Hoesly, R. M., Smith, S. J., Feng, L., Kllimont, Z., Janssens-Maenhout, G., Pitkanen, T., et al. (2016). Historical (1750–2014) anthropogenic emissions of reactive gases and aerosols from the Community Emissions Data System (CEDS), 7–8.

Huang, G., Brook, R., Crippa, M., Janssens-Maenhout, G., Schieberle, C., Dore, C., et al. (2017). Speciation of anthropogenic emissions of non-methane volatile organic compounds: A global gridded data set for 1970-2012. *Atmospheric Chemistry and Physics*, *17*(12), 7683–7701. https://doi.org/10.5194/acp-17-7683-2017

Huber, C., Beyerle, U., Leuenberger, M., Schwander, J., & Kipfer, R. (2006). Evidence for molecular size dependent gas fractionation in firn air derived from noble gases , oxygen , and nitrogen measurements. *Earth and Planetary Science Letters*, *243*, 61–73. https://doi.org/10.1016/j.epsl.2005.12.036

Hydrogen Council. (2017). Hydrogen Scaling Up.

Ikeda-Fukazawa, T., Horikawa, S., Hondoh, T., & Kawamura, K. (2002). Molecular dynamics studies of molecular diffusion in ice Ih. *Journal of Chemical Physics*, *117*(8), 3886–3896. https://doi.org/10.1063/1.1495844

Ikeda-Fukazawa, T., Kawamura, K., & Hondoh, T. (2004). Mechanism of molecular diffusion in ice crystals. *Molecular Simulation*, *30*(13–15), 973–979. https://doi.org/10.1080/08927020410001709307

Ikeda-Fukazawa, T., Fukumizu, K., Kawamura, K., Aoki, S., Nakazawa, T., & Hondoh, T. (2005). Effects of molecular diffusion on trapped gas composition in polar ice cores. *Earth and Planetary Science Letters*, *229*(3–4), 183–192. https://doi.org/10.1016/j.epsl.2004.11.011

Ildyakov, A. V., & Manakov, A. Y. (2014). Solubility of hydrogen in ice Ih at pressures up to 8 MPa. *International Journal of Hydrogen Energy*. https://doi.org/10.1016/j.ijhydene.2014.09.069

Ildyakov, A. V., Manakov, A. Y., Aladko, E. Y., Kosyakov, V. I., & Shestakov, V. A. (2013). Solubility of helium in ice Ih at pressures up to 2000 bar: Experiment and calculations.

Journal of Physical Chemistry B, *117*(25), 7756–7762. https://doi.org/10.1021/jp400985w

Jacob D. Morgan, Christo Buizert, Tyler J. Fudge, Kenji Kawamura, J. P. S., & Trudinger, C. M. (2022). Gas isotope thermometry in the South Pole and Dome Fuji Ice Cores provides evidence for seasonal rectification of ice core gas records. *The Cryosphere Discussions*, (March), 1–31. Retrieved from https://tc.copernicus.org/preprints/tc-2022-49/

Jean-Baptiste, P., Raynaud, D., Mantisi, F., Sowers, T., & Barkov, N. (1993). Measurement of helium isotopes in Antarctic ice: Preliminary results from Vostok. *C.R. Acad. Sci. Paris*, *316*(2), 491–497.

Jean-Baptiste, P., Petit, J.-R., Lipenkov, V. Y., Raynaud, D., & Barkov, N. I. (2001). Constraints on hydrothermal processes and water exchange in Lake Vostok from helium isotopes. *Nature*, *411*, 460–462.

Jordan, A., & Steinberg, B. (2011). Calibration of atmospheric hydrogen measurements. *Atmospheric Measurement Techniques*, *4*(3), 509–521. https://doi.org/10.5194/amt-4-509-2011

Khalil, M. A. K., & Rasmussen, R. A. (1990). Global increase of atmospheric molecular hydrogen. *Nature*, *347*, 743–745. https://doi.org/10.1016/0021-9797(80)90501-9

Khan, M. N., Rovetto, L. J., Peters, C. J., Sloan, E. D., Sum, A. K., & Koh, C. A. (2015). Effect of hydrogen-to-methane concentration ratio on the phase equilibria of quaternary hydrate systems. *Journal of Chemical and Engineering Data*, *60*(2), 418–423. https://doi.org/10.1021/je500675q

Kristensen, L. E., Amiaud, L., Fillion, J., Dulieu, F., & Lemaire, J. (2011). H2 , HD , and D2 abundances on ice-covered dust grains. *Astronomy & Astrophysics*, *44*, 1–7. https://doi.org/10.1051/0004-6361/200912124

Lamarque, J., Bond, T. C., Eyring, V., Granier, C., Heil, A., Klimont, Z., et al. (2010). Historical (1850 – 2000) gridded anthropogenic and biomass burning emissions of reactive gases and aerosols : methodology and application. *Atmospheric Chemistry and Physics*, *10*, 7017–7039. https://doi.org/10.5194/acp-10-7017-2010

Langenfelds, R. L., Francey, R. J., Pak, B. C., Steele, L. P., Lloyd, J., Trudinger, C. M., & Allison, C. E. (2002). Interannual growth rate variations of atmospheric CO2 and its δ13C, H2, CH4, and CO between 1992 and 1999 linked to biomass burning. *Global Biogeochemical Cycles*, *16*(3). https://doi.org/10.1029/2001gb001466

Lu, H., Wang, J., Liu, C., Ratcliffe, C. I., Becker, U., Kumar, R., & Ripmeester, J. (2012). Multiple H 2 occupancy of cages of clathrate hydrate under mild conditions. *Journal of the American Chemical Society*, *134*(22), 9160–9162. https://doi.org/10.1021/ja303222u

Lüthi, D., Bereiter, B., Stauffer, B., Winkler, R., Schwander, J., Kindler, P., et al. (2010). CO2 and O2/N2 variations in and just below the bubble-clathrate transformation zone of Antarctic ice cores. *Earth and Planetary Science Letters*, *297*(1–2), 226–233.

https://doi.org/10.1016/j.epsl.2010.06.023

Manabe, S., & Stouffer, R. J. (1980). Sensitivity of a global climate model to an increase of CO2 concentration in the atmosphere. *Journal of Geophysical Research*, *85*(C10), 5529–5554. https://doi.org/10.1029/JC085iC10p05529

Manakov, A. Y., Aladko, E. Y., & Ildyakov, A. V. (2017). Solubility of hydrogen in ice Ih along the ice melting curve. *International Journal of Hydrogen Energy*, *42*(1), 322–326. https://doi.org/10.1016/j.ijhydene.2016.12.120

Mao, W. L., & Mao, H. K. (2004). Hydrogen storage in molecular compounds. *Proceedings of the National Academy of Sciences of the United States of America*, *101*(3), 708–710. https://doi.org/10.1073/pnas.0307449100

Marik, T. (1998). *Atmospheric δ13C and δD measurements to balance the global methane budget*. Ruprecht-Karls-Univ.

Van Marle, M. J. E., Kloster, S., Magi, B. I., Marlon, J. R., Daniau, A. L., Field, R. D., et al. (2017). Historic global biomass burning emissions for CMIP6 (BB4CMIP) based on merging satellite observations with proxies and fire models (1750-2015). *Geoscientific Model Development*, *10*(9), 3329–3357. https://doi.org/10.5194/gmd-10-3329-2017

Matthews, J. H., & Fink, K. K. (2004). *Numerical Methods Using MATLAB* (4th ed.). Upper Saddle River, New Jersey: Prentice-Hall.

Menke, W. (1989). *Geophysical Data Analysis: Discrete Inverse Theory*. *Geophysical Data Analysis: Discrete Inverse Theory* (2nd ed.). San Diego, California: Academic Press Inc. https://doi.org/10.1016/b978-0-12-397160-9.00001-1

Meredith, L. K., Commane, R., Munger, J. W., Dunn, A., Tang, J., Wofsy, S. C., & Prinn, R. G. (2014). Ecosystem fluxes of hydrogen: A comparison of flux-gradient methods. *Atmospheric Measurement Techniques*, *7*(9), 2787–2805. https://doi.org/10.5194/amt-7-2787-2014

Miller, S. L. (1969). Clathrate Hydrates of Air in Antarctic Ice. *Science*, *165*(3892), 489–490.

Montzka, S. A., Spivakovsky, C. M., Butler, J. H., Elkins, J. W., Lock, L. T., & Mondeel, D. J. (2000). New observational constraints for atmospheric hydroxyl on global and hemispheric scales. *Science*, *288*(5465), 500–503. https://doi.org/10.1126/science.288.5465.500

Montzka, S. A., Kuijpers, L., Battle, M. O., Aydin, M., Verhulst, K. R., Saltzman, E. S., & Fahey, D. W. (2010). Recent increases in global HFC-23 emissions. *Geophysical Research Letters*, *37*(2). https://doi.org/10.1029/2009GL041195

Morgan, J. D., Buizert, C., Fudge, T. J., Kawamura, K., Severinghaus, J. P., and Trudinger, C. M. (2022). Gas isotope thermometry in the South Pole and Dome Fuji Ice Cores provides evidence for seasonal rectification of ice core gas records, *The Cryosphere Discuss.* [preprint], https://doi.org/10.5194/tc-2022-49. *Accepted*

Mousis, O., Chassefière, E., Lasue, J., Chevrier, V., Elwood Madden, M. E., Lakhlifi, A., et al. (2013). Volatile trapping in martian clathrates. *Space Science Reviews*, *174*(1–4), 213–250. https://doi.org/10.1007/s11214-012-9942-9

Namiot, A. Y., & Gorodetskaya, L. Y. (1969). Solubility of gases in ice. *Dokl. Akad. Nauk USSR*, *190*(3), 604–605.

Neftel, A., Oeschger, H., Schwander, J., & Stauffer, B. (1983). Carbon dioxide concentration in bubbles of natural cold ice. *Journal of Physical Chemistry*, *87*(21), 4116–4120. https://doi.org/10.1021/j100244a025

Noguchi, M., Tachibana, S., & Nagahara, H. (2019). Diffusivity and solubility of methane in ice Ih. *Geochemical Journal*, *53*(1), 83–89. https://doi.org/10.2343/geochemj.2.0537

Novelli, P. C. (2006). Atmospheric Hydrogen Mixing Ratios from the NOAA GMD Carbon Cycle Cooperative Global Air Sampling Network, 1988-2005.

Novelli, P. C., Crotwell, A. M., & Hall, B. D. (2009). Application of gas chromatography with a pulsed discharge helium ionization detector for measurements of molecular hydrogen in the atmosphere. *Environmental Science and Technology*. https://doi.org/10.1021/es803180g

Novelli, Paul C., Lang, P. M., Masarie, K. A., Hurst, D. F., Mycrs, R., & Elkins, J. W. (1999). Molecular hydrogen in the troposphere: Global distribution and budget. *Journal of Geophysical Research*, *104*(D23), 30427–30444.

P. Forster, T. Storelvmo, K. Armour, W. Collins, J. L. Dufresne, D. Frame, et al. (2021). *The Earth's Energy Budget, Climate Feedbacks, and Climate Sensitivity*. *Climate Change 2021: The Physical Science Basis. Contribution of Working Group I to the Sixth Assessment Report of the Intergovernmental Panel on Climate Change*. https://doi.org/10.1017/9781009157896.009.923

Paneth, F. A. (1937). The chemical composition of the Atmosphere. *Q. J. R. Meteorol. Soc.*, *63*, 433–438. https://doi.org/10.1002/qj.49706327114

Parrish, W. R., & Prausnitz, J. M. (1972). Dissociation Pressures of Gas Hydrates Formed by Gas Mixtures. *Industrial and Engineering Chemistry Process Design and Development*, *11*(1), 26–35. https://doi.org/10.1021/i260041a006

Patterson, J. D., Aydin, M., Crotwell, A. M., Petron, G., Severinghaus, J. P., & Saltzman, E. S. (2020). Atmospheric History of H2 Over the Past Century Reconstructed From South Pole Firn Air. *Geophysical Research Letters*, *47*(14), 1–8. https://doi.org/10.1029/2020GL087787

Patterson, John D., & Saltzman, E. S. (2021a). Diffusivity and solubility of H2 in ice Ih: Implications for the behavior of H2 in polar ice. *Journal of Geophysical Research Atmospheres*, *126*. https://doi.org/. https://doi. org/10.1029/2020JD033840

Patterson, John D., & Saltzman, E. S. (2021b). Diffusivity and solubility of H2 in ice Ih:

Implications for the behavior of H2 in polar ice. *Journal of Geophysical Research Atmospheres*, *126*, 1–14. https://doi.org/10.1029/2020JD033840

Patterson, John D, Aydin, M., Crotwell, A. M., Pétron, G., & Severinghaus, J. P. (2021). H 2 in Antarctic firn air : Atmospheric reconstructions and implications for anthropogenic emissions. *Proceedings of the National Academy of Sciences of the United States of America*, *118*. https://doi.org/10.1073/pnas.2103335118/-/DCSupplemental.90

Paulot, F., Paynter, D., Naik, V., Malyshev, S., Menzel, R., & Horowitz, L. W. (2021). Global modeling of hydrogen using GFDL-AM4.1: Sensitivity of soil removal and radiative forcing. *International Journal of Hydrogen Energy*, *46*(24), 13446–13460. https://doi.org/10.1016/j.ijhydene.2021.01.088

Petrenko, V. V., Martinerie, P., Novelli, P., Etheridge, D. M., Levin, I., Wang, Z., et al. (2013). A 60 yr record of atmospheric carbon monoxide reconstructed from Greenland firn air. *Atmospheric Chemistry and Physics*, *13*(15), 7567–7585. https://doi.org/10.5194/acp-13-7567-2013

Pieterse, G., Krol, M. C., Batenburg, A. M., Steele, L. P., Krummel, P. B., Langenfelds, R. L., & Röckmann, T. (2011). Global modelling of H2 mixing ratios and isotopic compositions with the TM5 model. *Atmospheric Chemistry and Physics*, *11*(14), 7001–7026. https://doi.org/10.5194/acp-11-7001-2011

Pieterse, G., Krol, M. C., Batenburg, A. M., Steele, L. P., Krummel, P. B., & Langenfelds, R. L. (2011). Global modelling of H2 mixing ratios and isotopic compositions with the TM5 model. *Atmospheric Chemistry and Physics*, *11*, 7001–7026. https://doi.org/10.5194/acp-11-7001-2011

Pieterse, G., Krol, M. C., Batenburg, A. M., M. Brenninkmeijer, C. A., Popa, M. E., O'Doherty, S., et al. (2013). Reassessing the variability in atmospheric H 2 using the two-way nested TM5 model . *Journal of Geophysical Research: Atmospheres*, *118*(9), 3764–3780. https://doi.org/10.1002/jgrd.50204

Prather, M. J. (2003). An environmental experiment with H2. *Science*, *302*(5645), 581–582. https://doi.org/10.1126/science.1091060

Previdi, M., Smith, K. L., & Polvani, L. M. (2021). Arctic amplification of climate change: A review of underlying mechanisms. *Environmental Research Letters*, *16*(9). https://doi.org/10.1088/1748-9326/ac1c29

Price, H., Jaeglé, L., Rice, A., Quay, P., Novelli, P. C., & Gammon, R. (2007). Global budget of molecular hydrogen and its deuterium content: Constraints from ground station, cruise, and aircraft observations. *Journal of Geophysical Research Atmospheres*, *112*(22), 1–16. https://doi.org/10.1029/2006JD008152

Prinn, R. G., Huang, J., Weiss, R. F., Cunnold, D. M., Fraser, P. J., Simmonds, P. G., et al. (2005). Evidence for variability of atmospheric hydroxyl radicals over the past quarter century. *Geophysical Research Letters*, *32*(7), 1–4. https://doi.org/10.1029/2004GL022228

Prinn, R.G., Weiss, R. F., Aduini, J., Arnold, T., Dewitt, H., Fraser, P. J., et al. (2019). History of chemically and radiatively important atmospheric gases from the Advanced Global Atmospheric Gases Experiment (AGAGE). https://doi.org/https://doi.org/10.3334/CDIAC/atg.db1001

Prinn, Ronald G., Weiss, R. F., Arduini, J., Arnold, T., Langley Dewitt, H., Fraser, P. J., et al. (2018). History of chemically and radiatively important atmospheric gases from the Advanced Global Atmospheric Gases Experiment (AGAGE). *Earth System Science Data*, *10*(2), 985–1018. https://doi.org/10.5194/essd-10-985-2018

Punshon, S., Moore, R. M., & Xie, H. (2007). Net loss rates and distribution of molecular hydrogen (H2) in mid-latitude coastal waters. *Marine Chemistry*, *105*(1–2), 129–139. https://doi.org/10.1016/j.marchem.2007.01.009

Reid, R. C., Prausnitz, J. M., Sherwood, T. K., & Poling, B. E. (1987). *The properties of gases and liquids* (4th ed.). New York: McGraw-Hill.

van Renssen, S. (2020). The hydrogen solution? *Nature Climate Change*, *10*(September), 799–801. https://doi.org/10.1038/s41558-020-0891-0

Rommelaere, V., Arnaud, L., & Barnola, J. (1997). Reconstructing recent atmospheric trace gas concentrations from polar firn and bubbly ice data by inverse methods. *Journal of Geophysical Research*, *102*(D25), 30069–30083.

Van Ruijven, B., Lamarque, J. F., Van Vuuren, D. P., Kram, T., & Eerens, H. (2011). Emission scenarios for a global hydrogen economy and the consequences for global air pollution. *Global Environmental Change*, *21*(3), 983–994. https://doi.org/10.1016/j.gloenvcha.2011.03.013

Salamatin, A. N., Hondoh, T., Uchida, T., & Lipenkov, V. Y. (1998). Post-nucleation conversion of an air bubble to clathrate air-hydrate crystal in ice. *Journal of Crystal Growth*, *193*(1–2), 197–218. https://doi.org/10.1016/S0022-0248(98)00488-6

Satoh, K., Uchida, T., Hondoh, T., & Mae, S. (1996). Diffusion coefficient and solubility measurements of noble gases in ice crystals. *Proc, NIPR Symp.Polar Meteorol, G]Aciol*, *10*, 73–81.

Schmidt, U. (1974). Molecular hydrogen in the atmosphere. *Tellus 26*, 78–90. https://doi.org/10.1038/270297a0

Schultz, M. G., Diehl, T., Brasseur, G. P., & Zittel, W. (2003). Air Pollution and Climate-Forcing Impacts of a Global Hydrogen Economy. *Science*, *302*(5645), 624–627. https://doi.org/10.1126/science.1088057

Schwander, J., Barnola, J. M., Andrie, C., Leuenberger, M., Ludin, A., Raynaud, D., & Stauffer, B. (1993). The Age of the Air in the Firn and the Ice at Summit, Greenland. *Journal of Geophysical Research*, *98*, 2831–2838.

Scranton, M. I., Jones, M. M., & Herr, F. L. (1982). Distribution and variability of dissolved hydrogen in the Mediterranean Sea. *Journal of Marine Research*, *40*(3), 873–892.

Scranton, Mary I., Novelli, P. C., & Loud, P. A. (1984). The distribution and cycling of hydrogen gas in the waters of two anoxic marine environments,. *Limnology and Oceanography*, *29*(5), 993–1003. https://doi.org/10.4319/lo.1984.29.5.0993

Serreze, M. C., Barrett, A. P., Stroeve, J. C., Kindig, D. N., & Holland, M. M. (2009). The emergence of surface-based Arctic amplification. *The Cryosphere*, *3*(1), 11–19. https://doi.org/10.5194/tc-3-11-2009

Severinghaus, J. P., & Battle, M. O. (2006). Fractionation of gases in polar ice during bubble close-off: New constraints from firn air Ne, Kr and Xe observations. *Earth and Planetary Science Letters*. https://doi.org/10.1016/j.epsl.2006.01.032

Severinghaus, J. P., Grachev, A., & Battle, M. (2001). Seasonal Temperature Gradients. *Geochemistry Geophysics Geosystems*, *2*(7).

Severinghaus, J. P., Albert, M. R., Courville, Z. R., Fahnestock, M. A., Kawamura, K., Montzka, S. A., et al. (2010). Deep air convection in the firn at a zero-accumulation site, central Antarctica. *Earth and Planetary Science Letters*, *293*(3–4), 359–367. https://doi.org/10.1016/j.epsl.2010.03.003

Shoji, H., & Langway, C. C. (1982). Air hydrate inclusions in fresh ice core. *Nature*, *298*(5874), 548–550. https://doi.org/10.1038/298548a0

Smith-Downey, N. V., Randerson, J. T., & Eiler, J. M. (2006). Temperature and moisture dependence of soil H2 uptake measured in the laboratory. *Geophysical Research Letters*, *33*(14), 1–5. https://doi.org/10.1029/2006GL026749

Strauss, H. L., Chen, Z., & Loong, C. K. (1994). The diffusion of H2 in hexagonal ice at low temperatures. *The Journal of Chemical Physics*, *101*(8), 7177–7180. https://doi.org/10.1063/1.468303

Sumner, A. L., & Shepson, P. B. (1999). Snowpack production of formaldehyde and its effect on the Arctic troposphere. *Nature*, *398*(6724), 230–233. https://doi.org/10.1038/18423

Trudinger, C. M., Enting, I. G., Etheridge, D. M., Francey, R. J., Levchenko, V. A., Steele, L. P., et al. (1997). Modeling air movement and bubble trapping in firn. *Journal of Geophysical Research Atmospheres*. https://doi.org/10.1029/96JD03382

Verhallen, P. T. H. M., Oomen, L. J. P., Elsen, A. J. J. M. v. d., & Kruger, J. (1984). The diffusion coefficients of helium, hydrogen, oxygen and nitrogen in water determined from the permeability of a stagnant liquid layer in the quasi-steady state. *Chemical Engineering Science*, *39*(11), 1535–1541. https://doi.org/10.1016/0009-2509(84)80082-2

Vollmer, M. K., Walter, S., Mohn, J., Steinbacher, M., Bond, S. W., Rockmann, T., & Reimann, S. (2012). Molecular hydrogen (H2) combustion emissions and their isotope (D/H)

signatures from domestic heaters, diesel vehicle engines, waste incinerator plants, and biomass burning. *Atmospheric Chemistry and Physics*, *12*(14), 6275–6289. https://doi.org/10.5194/acp-12-6275-2012

Vos, W. L., Finger, L. W., Hemley, R. J., & Mao, H. K. (1993). Novel H2-H2O clathrates at high pressures. *Physical Review Letters*, *71*(19), 3150–3153. https://doi.org/10.1103/PhysRevLett.71.3150

Wang, D., Jia, W., Olsen, S. C., Wuebbles, D. J., Dubey, M. K., Rockett, A. A., & Wuebbles, C. D. J. (2013a). Impact of a future H 2 -based road transportation sector on the composition and chemistry of the atmosphere – Part 1 : Tropospheric composition and air quality. *Atmospheric Chemistry and Physics*, *13*(2), 6117–6137. https://doi.org/10.5194/acp-13-6117-2013

Wang, D., Jia, W., Olsen, S. C., Wuebbles, D. J., Dubey, M. K., Rockett, A. A., & Wuebbles, C. D. J. (2013b). Impact of a future H 2 -based road transportation sector on the composition and chemistry of the atmosphere – Part 2 : Stratospheric ozone. *Atmospheric Chemistry and Physics*, *13*, 6139–6150. https://doi.org/10.5194/acp-13-6139-2013